

Phononic and Excitonic Properties of Transition Metal Dichalcogenides

vorgelegt von

M.Sc. – Physiker

Hans Tornatzky

ORCID iD: 0000-0002-3153-0501

von der Fakultät II – Mathematik und Naturwissenschaften
der Technischen Universität Berlin
zur Erlangung des akademischen Grades

Doktor der Naturwissenschaften

Dr. rer. nat.

genehmigte Dissertation

Promotionsausschuss:

Vorsitzender: Prof. Dr. Michael Lehmann

Gutachter: Prof. Dr. Axel Hoffmann

Gutachter: Prof. Dr. Janina Maultzsch

Tag der wissenschaftlichen Aussprache: 27.6.2019

Berlin 2019

Abstract

Transition metal dichalcogenides (TMDCs) like MoS₂, MoSe₂, WS₂, and WSe₂ have attracted enormous interest in the past decade. TMDCs are van-der-Waals crystals with highly anisotropic properties, which allows the exfoliation of individual layers. Their remarkable physical properties, such as the high exciton binding energy and the locking of spin- and valley degree of freedom, make them promising for applications in optoelectronic, spintronic, and valleytronic devices. Phonons are fundamental to physical processes, like carrier and spin relaxation, exciton dynamics, and many more. However, experimental data of the complete phonon dispersion relations in these materials is still missing.

In this thesis the first measurements of the full basal plane phonon dispersions of MoS₂ and WS₂, determined by inelastic X-ray scattering, are presented. The results underline the two-dimensional nature of MoS₂ through the observation of a quadratic out-of-plane acoustic phonon branch (also called flexural mode), negligible dispersion in the out-of-plane direction and near-degenerate Davydov pairs. Supported by simulations of the dynamical structure factor and first-principles calculations several cases of activation and deactivation of branches could be explained.

For WS₂ the influence of the out-of-plane component of the scattering point in reciprocal space was investigated. It was found that the branches forming a Davydov pair are selectively active with either even- or odd- l Bragg peaks.

Further, photoluminescence measurements with different excitation energies on single-layer MoS₂ and MoSe₂ are presented in order to examine the resonance behavior of the conservation of circular polarization in these transition metal dichalcogenides. The circular polarization of the emitted light is found to be fully conserved

in MoS₂ and up to 84%/79% (A/A^- peaks) in MoSe₂ close to resonance. The values for MoSe₂ surpass any previously reported value. In clear contrast to previous reports, the degree of circular polarization decreases at energies lower than the prediction of the 2 *LA phonon mechanism*. These findings indicate that at least two competing processes underly the depolarization of the emission in single-layer transition metal dichalcogenides. Different mechanisms currently debated in the community are discussed and two new mechanisms are proposed for the valley depolarization in doped samples through exciton-electron scattering and through the decay of momentum-indirect trions.

Furthermore, the influence of surface contamination on the circularly polarized luminescence from single-layer MoS₂ is presented. While the decay of polarization remains unaffected, observations of a blue shift of the excitonic transitions and dynamics of bright defect states on long time scales reveal the strong influence of the surrounding medium on the quasi two-dimensional material.

Zusammenfassung

Die Stoffklasse der MX_2 Übergangsmetall-Dichalkogenide (engl. TMDCs) zu der Materialien wie MoS_2 , $MoSe_2$, WS_2 und WSe_2 gehören, haben im zurückliegenden Jahrzehnt außerordentliche Aufmerksamkeit in der Forschung erhalten. TMDCs sind van-der-Waals gebundene, geschichtete Strukturen mit hochgradig anisotropen Eigenschaften, die es erlauben einzelne Lagen mechanisch zu separieren. Ihre herausragenden Eigenschaften, zu denen eine große Exzitonenbindungsenergie und die gekoppelten Spin- und *Valley*freiheitsgrade gehören, machen sie zu einem vielversprechendem System für künftige Anwendungen in der Optoelektronik, sowie der Spin- und Valleytronik. Phononen spielen eine fundamentale Rolle in physikalischen Prozessen, wie der Ladungsträger- und Spinrelaxation, der Exzitondynamik und vielen weiteren. Nichtsdestotrotz ist eine vollständige Phononendispersionsrelation eines der TMDCs experimentell nicht bestimmt.

In dieser Arbeit werden die ersten Messungen der vollständigen Phonendispersionen der Basalebene von MoS_2 und WS_2 durch inelastische Röntgenstreuung bestimmt. Die Ergebnisse unterstreichen den zweidimensionalen Charakter von MoS_2 durch die Beobachtung einer quadratischen Form des akustischen Phononenzweiges transversaler Auslenkung senkrecht zur Basalebene (ZA), sowie einer vernachlässigbaren Dispersion senkrecht zur Basalebene und nahezu degenerierter Davydov-Paare. Unterstützt durch Simulationen des dynamischen Strukturfaktors und ab-initio Berechnungen konnten mehrere Fälle von Aktivierung und Deaktivierung von Phononenzweigen erklärt werden.

Für WS_2 wurde der Einfluss der Komponente senkrecht zur Basalebene des Streupunktes im reziproken Raum untersucht. Es wurde festgestellt, dass die Zweige, die

ein Davydov-Paar bilden, selektiv, entweder mit geradem oder ungeradem l -Miller Index Bragg-Peak aktiv sind.

Weiterhin werden Photolumineszenzmessungen mit unterschiedlichen Anregungsenergien an einschichtigem MoS₂ und MoSe₂ vorgestellt, um das Resonanzverhalten der Erhaltung der zirkulären Polarisation in diesen Übergangsmetall-Dichalcogeniden zu untersuchen. Die zirkuläre Polarisation des emittierten Lichts ist nahe der Resonanz in MoS₂ vollständig und in MoSe₂ bis zu 84%/79% (A/A^- Peaks) erhalten. Die Werte für MoSe₂ übertreffen jeden zuvor veröffentlichten Wert. Im deutlichen Gegensatz zu früheren Berichten, nimmt der Grad der zirkulären Polarisation bei Energien ab, die niedriger sind als die Vorhersage des *2 LA Phononen Mechanismus*. Diese Ergebnisse deuten darauf hin, dass mindestens zwei konkurrierende Prozesse der Depolarisierung der Emission in einschichtigen TMD-Cs zugrunde liegen. Verschiedene Mechanismen, die derzeit in der Forschungsgemeinschaft betrachtet werden, werden im Kontext der Datenlage, unter hinzunahme der experimentell bestimmten Dispersionsrelation, diskutiert. Desweiteren werden zwei neue Mechanismen für die Depolarisation in dotierten Proben durch Exziton-Elektronenstreuung und durch den Zerfall von Impuls-indirekten Trionen vorgeschlagen.

Darüber hinaus wird der Einfluss von Oberflächenkontamination auf die zirkular polarisierte Lumineszenz von einschichtigem MoS₂ dargestellt. Während die Resonanz der zirkulären Polarisation unberührt bleibt, zeigen Beobachtungen einer Blauverschiebung der exzitonischen Übergänge, und die Dynamik optisch aktiver Defektzustände auf langen Zeitskalen, den starken Einfluss des umgebenden Mediums auf das quasi zweidimensionale Material.

List of publications

1. **H. Tornatzky**, D. Hardeman, S. Esconjauregui, L. D'Arsié, R. Xie, H. Sugime, J. Yang, T. Makaryan, C. Thomsen, and J. Robertson, "Evaluation of bimetallic catalysts for the growth of carbon nanotube forests", *physica status solidi (b)* **250**, 2605–2610 (2013).
2. B. Chen, G. Zhong, P. Goldberg Oppenheimer, C. Zhang, **H. Tornatzky**, S. Esconjauregui, S. Hofmann, and J. Robertson, "Influence of packing density and surface roughness of vertically-aligned carbon nanotubes on adhesive properties of gecko-inspired mimetics", *ACS Applied Materials & Interfaces* **7**, 3626–3632 (2015).
3. C. Bothe, A. Kornowski, **H. Tornatzky**, C. Schmidtke, H. Lange, J. Maultzsch, and H. Weller, "Solid-state chemistry on the nanoscale: ion transport through interstitial sites or vacancies?", *Angewandte Chemie International Edition* **54**, 14183–14186 (2015).
4. M. Rafipoor, D. Dupont, **H. Tornatzky**, M. D. Tessier, J. Maultzsch, Z. Hens, and H. Lange, "Strain Engineering in InP/(Zn,Cd)Se Core/Shell Quantum Dots", *Chemistry of Materials* **30**, 4393–4400 (2018).
5. **H. Tornatzky**, A.-M. Kaulitz, and J. Maultzsch, "Resonance profiles of valley polarization in single-layer MoS₂ and MoSe₂", *Physical Review Letters* **121**, 167401 (2018).
6. **H. Tornatzky**, R. Gillen, H. Uchiyama, and J. Maultzsch, "Phonon dispersion in MoS₂", *Physical Review B* **99**, 144309 (2019).
7. A. Pierret, **H. Tornatzky**, and J. Maultzsch, "Anti-Stokes photoluminescence of WS₂", *physica status solidi (b)* *just accepted* (2019).
8. M. Rafipoor, **Tornatzky, H.**, D. Dupont, J. Maultzsch, M. D. Tessier, Z. Hens, and H. Lange, "Strain in inp/znse,s core/shell quantum dots from lattice mismatch and shellthickness - material stiffness influence", *under review at Journal of Chemical Physics*.
9. **H. Tornatzky**, B. Graczykowski, S. Reparaz, R. Gillen, Z. Galazka, J. Maultzsch, and M. R. Wagner, "Anisotropy of thermal conductivity, elasticity, and phonon modes of beta gallium oxide (β -Ga₂O₃)", *in preparation*.

Contents

Abstract	III
Zusammenfassung (German Abstract)	V
List of publications	VII
1. Introduction	1
2. Transition metal dichalcogenides: Structural and optical properties	5
2.1. Structure of D_{6h}^4 TMDCs	6
2.2. Optical properties of D_{6h}^4 TMDCs	10
2.2.1. Excitons in quasi two-dimensional systems	11
2.3. Inelastic light scattering in TMDCs	19
2.3.1. Inelastic X-ray scattering	21
2.3.2. Raman scattering	23
3. Experimental techniques	27
3.1. Sample preparation	27
3.2. Optical spectroscopy	32
3.2.1. The XY laboratory	33
3.2.2. The LabRAM laboratory	36
3.3. Inelastic X-ray scattering	37
3.3.1. High resolution IXS beamlines BL35XU and ID28	37
4. Phonon dispersions of TMDCs	41
4.1. Simulation of IXS intensities	41
4.2. Phonon dispersion of MoS_2	45
4.2.1. Sample	45
4.2.2. IXS measurements	48
4.2.3. Comparison of the phonon dispersion with literature	57
4.3. IXS of WS_2	59

4.4. Comparison of the phonon dispersion from IXS with the literature	71
4.5. Conclusion: inelastic scattering on TMDCs	72
5. Resonances of the degree of circular polarization with excitonic transitions	75
5.1. Circularly polarized photoluminescence spectroscopy of SL TMDCs	77
5.2. Resonance of the degree of polarization $\rho(\Delta E)$	79
5.3. Influence of surface contaminants on the PL	89
5.4. Comparison of DOP ρ values with the literature	96
5.5. Conclusion: Resonances of the degree of circular polarization	98
6. Summary	101
A. Appendix	XI
A 1. Design of an IXS-sample holder	XI
A 2. Displacement patterns of phonons at basal-plane high-symmetry points	XIII
A 3. Python scripts used for IXS data analysis	XVII
A 3.1. Header: import of libraries and definitions of variables and functions	XIX
A 3.2. Folding of actual, measured (hkl) into one irreducible part of the 1. BZ	XXVIII
A 3.3. Evaluation of error from projection onto high-symmetry directions	XXIX
A 3.4. Read FOURC files and split scans into files	XLIII
A 3.5. Plot all spectra	XLIV
A 3.6. Offset correction and interpolation of spectra	XLVI
A 3.7. Python script to reformat measurement table	XLVI
References	XLIX

1. Introduction

Transition metal dichalcogenides (TMDCs) like MoS₂ and MoSe₂ have emerged as promising materials for various future applications due to their properties when thinned down to a single-layer (SL). In the SL limit, they become direct semiconductors with their band gaps located at the K points in the Brillouin zone.

MoS₂ or *molybdenite* in its bulk form is a well known material and has been investigated for almost a century [1]. Thin layers of MoS₂ have also been investigated in the 1960's [2, 3], however it was not until the work of Novoselov *et al.* [4] in the mid-2000's, in which they produced and characterized single-layer graphite, or *graphene*, that atomically thin materials attracted large attention.

In contrast to graphene, single-layer TMDCs such as MoS₂, WS₂, MoSe₂ and WSe₂ are direct semiconductors with optical band gaps in the visible spectral range, which are governed by tightly bound excitons [5]. Strong exciton binding energies emerge on the order of 0.5 eV [5–10], as a result of large effective electron and hole masses, low screening from the environment and the spatial confinement effect. Furthermore, these materials exhibit strong spin-orbit coupling, which results in a large valence band splitting of a few hundred meV and a splitting of a few meV in the conduction bands at the K points [11–14]. Optical selection rules for circularly polarized light in single layers lead to transitions where electrons and holes are exclusively generated at either K or K' , as time reversal symmetry in the absence of inversion symmetry couples spin and valley (so-called valley polarization) [11, 15–19]. Hence, in theory excitation with circularly polarized light is followed by the emission of a photon with the same circular polarization.

This valley degree of freedom has been investigated in non-TMDC materials such as AlAs [20], bismuth [21] and graphene [22–24]. However, these materials do not

1. Introduction

show any valley polarization without external manipulation of the materials' properties. In TMDCs a high degree of valley polarization has been observed as an intrinsic property. This makes TMDCs an ideal platform to investigate the valley pseudospin and to eventually realize electronics based on the valley degree of freedom, i. e. *valleytronics* [25].

Since the first observation of valley polarization in TMDCs in 2012 [18, 19], most groups found imperfect conservation of polarization under different experimental conditions [see, e. g. 15, 19, 26]. The origin of such reduction in circular polarization of the emitted light from these materials is still controversially discussed. Different mechanisms limiting the conservation of circular polarization are suggested in the literature.

Some of these mechanisms consider phonon-scattering of charge carriers between the K points. However, despite their importance experimental data on the full phonon dispersion of MoS_2 and other TMDCs are still missing. Not only the conservation of polarization, but also carrier- and exciton-dynamics [Suelig2016, 27, 28], electron-phonon coupling in superconducting states [29, 30] and relaxation of spins [31] crucially depend on phonons. Only one high-symmetry direction of the Brillouin zone in MoS_2 has been accessed so far using inelastic neutron scattering (INS) [32]. Strikingly, the most relevant part necessary to describe scattering with large phonon wave vectors q or between the nonequivalent points K and K' (i. e., between the valleys) is completely missing and has so far only been addressed by calculations, e. g. Refs. [33–35]. The same holds for the other TMDCs, which have in common, as an obstacle for INS experiments, the in-plane nature of the phonon dispersion and the lack of large single crystals.

In this thesis, I will present the full basal plane phonon dispersions of MoS_2 and WS_2 as measured by inelastic X-ray scattering. Furthermore, I will present investigations of the mechanisms underlying the valley depolarization in MoS_2 and MoSe_2 .

In chapters 2 and 3 I will review the structural and electronic properties, leading to the remarkable properties of TMDCs along with the used experimental techniques.

In Chapter 4 I present the experimental determination by inelastic X-ray scattering and analysis of the basal plane phonon dispersions of MoS_2 and WS_2 . For this I

examine simulations of the dynamical structure factor to investigate the activation and deactivation of phonon-branches when progressing through the Brillouin zone. Furthermore, for WS₂ the out-of-plane dispersion is investigated.

Chapter 5 presents circularly polarized photoluminescence excitation spectroscopy. With the results of these measurements and the knowledge about the experimental phonon dispersion, depolarization mechanisms currently subject to debate will be evaluated. Furthermore, the influence of surface contaminants on the luminescence is investigated.

2. Transition metal dichalcogenides: Structural and optical properties

Many transition metal dichalcogenides (TMDCs) have a layered structure and can be thinned down to single-layers, promising new properties originated by quantum confinement effects or changes in crystal symmetry. An example of such a phenomenon is found, when the dimensionality of a superconductor is reduced. This lowers or even eliminates the orbital contribution to the critical magnetic field B_{c2} , leaving it determined by the paramagnetic contribution (spin alignment in Cooper pair) [36]. This is giving rise to an effective Zeeman-field that locks spins in the out-of-plane direction, which protects against alignment with the external magnetic field, and thereby the breakdown of the Cooper pair [37]. For a superconducting TMDC this can be easily achieved by reducing the number of layers.

For group VIb TMDCs belonging to the MoS_2 family, namely those belonging to the D_{6h}^4 space group, such as MoTe_2 or WSe_2 fascinate through their electronic properties, such as a large exciton binding energies, which allows the observation of excitonic effects at room temperature. Moreover, in their single-layer form spin and valley degrees of freedom are locked. Exploiting this effect allows to develop new applications, opening the field of valleytronics.

In this chapter, I will introduce structural and electronic properties relevant for the discussion of the phonon dispersion and valley polarization in the following chapters.

2.1. Structure of D_{6h}^4 TMDCs

MX_2 -Transition metal dichalcogenides (TMDCs) like MoS_2 consist of van der Waals bound sheets, commonly called *single-layers* (SL).¹ Each of these layers again consists of three covalently bound atomic layers (X-M-X), forming a trigonal prismatic structure (see Fig. 2.1 a - d). These layers have a horizontal mirror symmetry σ_h (within the \vec{a}_1 - \vec{a}_2 plane; blue hexagon in Fig. 2.1 c), a threefold rotation symmetry C_3 axis and a S_3 mirror-rotation axis (Fig. 2.1 b & d). Both are parallel to the \vec{a}_3 -axis. Further, they have three (horizontal, i. e. $\perp C_3$) C_2 rotation axes (within the σ_h -plane) and three σ_v vertical mirror planes each containing one of the C_2 -axes (Figs. 2.1 b & d). With the identity E these symmetry operations build the point group $D_{3h}^1 = E \oplus \sigma_h \oplus C_3 \oplus S_3 \oplus 3C_2 \oplus 3\sigma_v$ (Schoenflies notation) [38].

Stacking two single-layers along the \vec{a}_3 -axis, with the second layer rotated by 180 degrees around the C_3 -axis, a bi-layer is obtained (BL, cf. Fig.2.1 e). This BL inherits most of the symmetry operations of the single-layer except for the horizontal mirror plane, however, adds inversion symmetry i (with its center in between the layers). Further, the BL adds the improper rotation symmetry $S_6 = \sigma_h C_6 = i C_3$ [39] and replaces the 3 vertical mirror planes for three dihedral σ_d (bisecting the angle between two C_2). The symmetry of the structure therefore is $D_{3d}^3 = E \oplus C_3 \oplus 3C_2 \oplus i \oplus S_6 \oplus 3\sigma_d$ [33], while the last three symmetries are obtained by inverting the first three [33]. Due to the rotated second layer, the unit cell expands over two single-layers and contains 6 atoms, see Fig. 2.1 e.

Adding another (third) layer leads again to the symmetry of the single-layer as the σ_h plane is recovered in the middle layer and the inversion symmetry is broken. Further layers added to the system keeps alternating the symmetry of the single- and bi-layer. All N-layered structures can therefore be classified to odd and even N number of layers.

Note that in fact there are two 2H stacking orders, which are obtained when defining the C_3 axis, around which every other layer is rotated, in the metal atom of the first layer (2Ha: AbA CbC stacking) or in the middle of the formed hexagon (2Hc: CaC AcA stacking). While the 2Ha commonly is reported for materials such

¹Even though the "single-layer" consists of three covalently bound, atomic sub-layers (c.f. Fig 2.1 c), the literature refers to the isolable, but stable layers as the lowest unit. This nomenclature is adopted in this thesis.

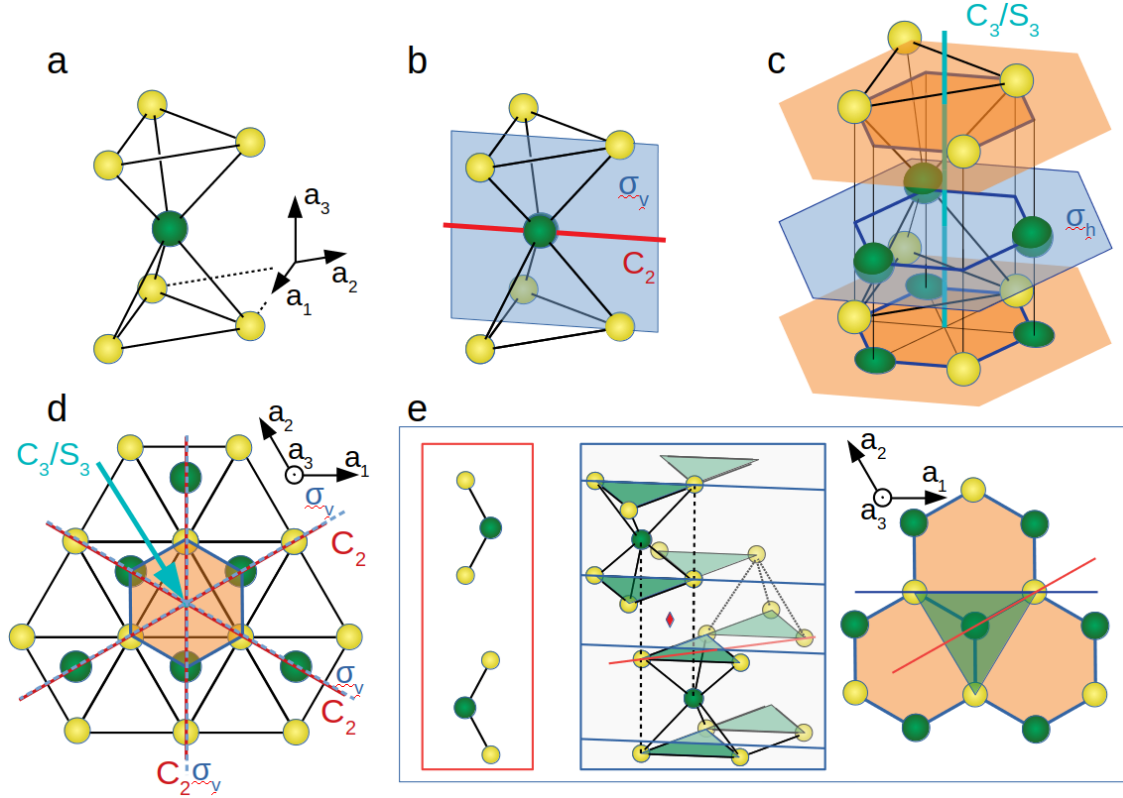


Figure 2.1: Real space structure of TMDCs of the MoS₂ family. Green (yellow) spheres depict the transition metal (chalcogen) atoms. **a:** Transition metal atom with nearest neighboring chalcogen atoms in trigonal prismatic coordination of the D_{3h}^1 , D_{3d}^3 or D_{6h}^4 structures (odd-N-layer, even-N-layer, bulk, resp.). **b (c):** Depiction of the σ_v and C_2 (C_3 , S_3 and σ_h) symmetries of the single-layer structure in the same perspective of **a**. **d:** View onto the basal plane, i. e., parallel to the \vec{a}_3 axis. **e:** Stacking structure in few-layer or bulk material. The inversion center has been depicted with a red diamond.

as TaS₂ and related, TMDCs of the MoS₂ family tend to form the 2Hc polytype. Finally, adding infinite layers results in the bulk 2Hc structure which is of D_{6h}^4 symmetry.

Due to the C_3 symmetry two equivalent, although not identical definitions of the in-plane lattice vectors \vec{a}_1 and \vec{a}_2 are possible where \vec{a}_1 and \vec{a}_2 enclose an angle of 60° or 120° (cf. Fig. 2.2). The reciprocal space of the hexagonal TMDCs is again hexagonal, inheriting the same ambiguity of lattice vectors, leading to different descriptions of scattering processes. The correspondence of the two systems is simple. Considering an angle of 120° in between the real space lattice vectors $\vec{a}_1^{120^\circ}$ and $\vec{a}_2^{120^\circ}$, and a and c being the in-plane and out-of-plane lattice constants, the

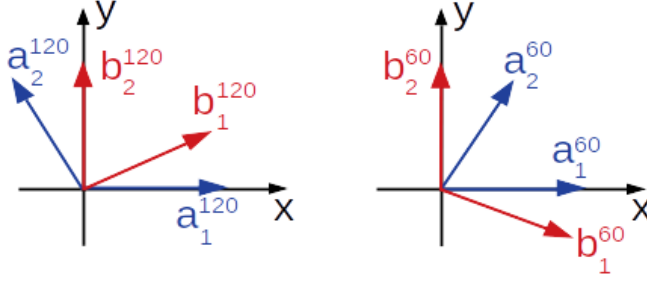


Figure 2.2.: Left (right): Conventional (unconventional) definition of lattice vectors with 120° (60°) in between the a_1 and a_2 lattice vectors and the resulting pairs of reciprocal lattice vectors.

reciprocal lattice vectors $\vec{b}_1^{120^\circ}$ and $\vec{b}_2^{120^\circ}$ calculate as

$$\vec{a}_1^{120^\circ} = \begin{pmatrix} 1 \\ 0 \\ 0 \end{pmatrix} a \quad \vec{b}_1^{120^\circ} = \frac{2\pi}{V} (\vec{a}_2 \times \vec{a}_3) = \frac{2\pi ac}{V} \begin{pmatrix} \sqrt{3}/2 \\ 1/2 \\ 0 \end{pmatrix} \quad (2.1)$$

$$\vec{a}_2^{120^\circ} = \begin{pmatrix} -1/2 \\ \sqrt{3}/2 \\ 0 \end{pmatrix} a \quad \vec{b}_2^{120^\circ} = \frac{2\pi ac}{V} \begin{pmatrix} 0 \\ 1 \\ 0 \end{pmatrix}. \quad (2.2)$$

Now, considering an angle of 60° in between $\vec{a}_1^{60^\circ}$ and $\vec{a}_2^{60^\circ}$ while keeping $\vec{a}_1^{60^\circ} = \vec{a}_1^{120^\circ}$, the reciprocal lattice vectors calculate as

$$\vec{a}_1^{60^\circ} = \begin{pmatrix} 1 \\ 0 \\ 0 \end{pmatrix} a \quad \vec{b}_1^{60^\circ} = \frac{2\pi}{V} (\vec{a}_2 \times \vec{a}_3) = \frac{2\pi ac}{V} \begin{pmatrix} \sqrt{3}/2 \\ -1/2 \\ 0 \end{pmatrix} = \begin{pmatrix} 1 \\ -1 \\ 1 \end{pmatrix} \circ \vec{b}_1^{120^\circ} \quad (2.3)$$

$$\vec{a}_2^{60^\circ} = \begin{pmatrix} 1/2 \\ \sqrt{3}/2 \\ 0 \end{pmatrix} a \quad \vec{b}_2^{60^\circ} = \frac{2\pi ac}{V} \begin{pmatrix} 0 \\ 1 \\ 0 \end{pmatrix} = \vec{b}_2^{120^\circ}. \quad (2.4)$$

By comparing the reciprocal lattice vectors one can easily deduce, that the transformation is performed by changing the sign of the second entry of the \vec{b}_1 -vector (for this definition of the real space vectors). Figure 2.2 depicts the two different definitions of the vector sets. Conventionally an angle of 120° in between \vec{a}_1 and \vec{a}_2 is chosen in real space, resulting in an angle of 60° between the reciprocal lattice vectors \vec{b}_1 and \vec{b}_2 .

The first hexagonal Brillouin zone (BZ) is shown in figure 2.3 a with its high-symmetry points. The Γ and K points mark the center and the edges of the hexagon, while M sits at half the distance to a Γ point of a neighboring BZ and at half the distance of the line connecting two neighboring K points. The triangle spanned by Γ - K - M - Γ holds the irreducible part of the BZ in the basal plane. The remaining high symmetry points are the A , H and L points which correspond to Γ , K and M with a translation of $(0\ 0\ \frac{1}{2})$ in units of the reciprocal lattice vectors.

The reciprocal space of single-layer TMDCs comprises only the gray hexagon in figure 2.3 a, due to its 2D-nature, and the, hence, missing \vec{a}_3 vector.

In figure 2.3 b the single-layer reciprocal space is shown, with the reciprocal lattice vectors and the high symmetry points in the rhombohedral unit cell. Further, the transformation from the hexagonal to the cartesian basis as well as the lengths in between high symmetry points are given.

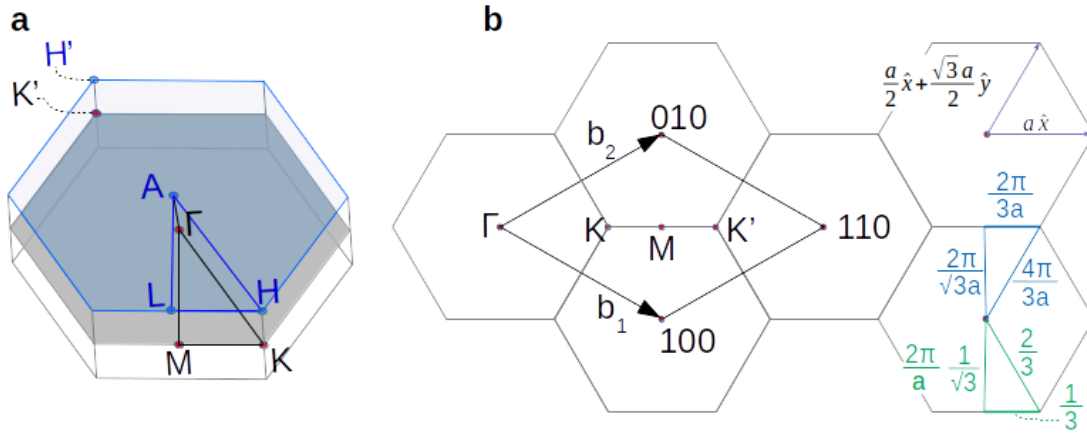


Figure 2.3: **a:** First Brillouin zone of bulk TMDCs with its high symmetry points. The gray area corresponds to the hexagonal Brillouin zone of a single layer TMDC. **b:** Depiction of the reciprocal space of two-dimensional hexagonal crystals with reciprocal space vectors \vec{b}_1 and \vec{b}_2 . Further, the lengths of the high symmetry lines in units of the reciprocal lattice vectors (green) and absolute momentum (blue), and the transformation in cartesian coordinates are shown (black).

2.2. Optical properties of D_{6h}^4 TMDCs

Light-matter-interaction describes in most cases (except, e.g. the radioactive γ -radiation) the photon-electron-interaction. The optical properties of a material under investigation is consequently defined by its electronic structure. The TMDCs of the MoS₂ family (except for WTe₂) are semiconductors, with band gaps in the visible (MoS₂, WS₂, MoSe₂, WSe₂) or near-infrared (MoTe₂) spectral range, making them interesting for various opto-electronic applications [40–43].

In bulk material, the maximum of the valence band (VBM) is situated at the Γ point, while the minimum of the conduction band (CBM) is found at the Q point,² leading to an indirect band gap. A direct transition is found at the (energetically degenerate) K and K' points, however, hundreds of meV above the bulk indirect band gap (see Fig. 2.4, first panel).

When thinning the crystal down to a single layer, the band gap evolves from indirect to direct, as the indirect gap grows with decreasing layer number, while the direct transition at K remains nearly constant (cf. Fig. 2.4) [40, 45]. This effect

²Roughly at half the length $\bar{\Gamma K}$. [44]

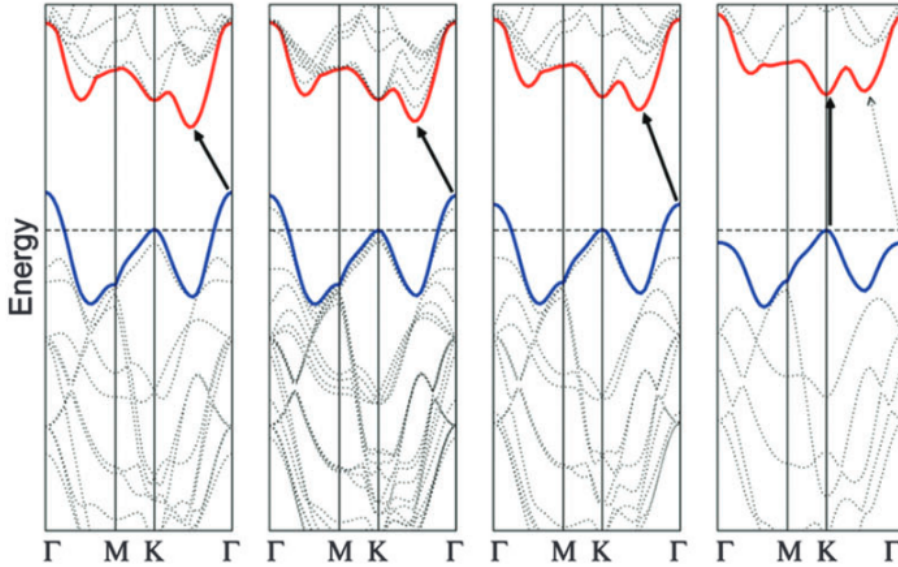


Figure 2.4.: Transition of the bandstructure from bulk (first panel) to single layer (fourth panel). Figure taken from [40].

can be understood by analyzing the orbitals' contributing to the distinct (local) VBM and CBM. At the Γ and Q point VBM and CBM (indirect transition) are composed of chalcogen p_z and transition metal d_z orbitals, with considerable overlap in between layers – prone to changes in the layer number of the material [14, 15, 46]. At the K points the VBM and CBM are composed mainly of transition metal $d_{x^2-y^2} \pm id_{xy}$ and d_{z^2} orbitals, respectively [15, 46]. The orbitals building the VBM and CBM at the K points have only little overlap in between layers leaving the direct transition barely affected of layer number changes [40, 47]. Ultimately, for the change from two to one layer, the indirect gap grows larger than the direct gap at the K points (see Fig. 2.4, fourth panel). This indirect-to-direct transition from bi- to single-layer is accompanied by a strong increase of the photoluminescence quantum yield [47].

The observed luminescence is not originated from band-to-band transitions but stems – even at room temperature – from excitonic transitions. Excitons and their peculiar properties in 2D materials will therefore be discussed in the following section.

2.2.1. Excitons in quasi two-dimensional systems

As the optical properties of TMDCs are dominated by excitonic transitions, I will dedicate this section to a (rather short) introduction of excitons and the characteristics of these in 2D-materials. Even though these excitons are confined within one SL and are technically bound to this layer, they will be referred to as *free excitons* if not bound, e. g. to a defect. This nomenclature is according to the jargon of the community.

In general, non-metallic matter can absorb a photon with suitable energy by lifting an electron into the conduction band, thus leaving behind a hole in the valence band. These transitions can occur at several points in the reciprocal space where the electron's and hole's joint density of states is large, i. e. where the bands are parallel or have each a large individual density of states. These points are commonly referred to as band nesting regions [14]. While efficient transitions occur in

2. Transition metal dichalcogenides: Structural and optical properties

these regions when the wave functions of electron and hole have a large overlap, which is the case for similar effective masses of electron and hole. These photo-generated carriers can bind to excitons due to their Coulomb interaction. On the other hand, direct generation of an exciton through the absorption of a photon is also possible, however, with the restriction of momentum conservation only allowing the generation of excitons obeying $p_{\text{exciton}} = p_{\text{photon}}$, leading to excitons with near-zero kinetic energy. This is consequently also true for the radiative relaxation. This restriction gives rise to the figure of the light cone, which is constructed by the linear dispersion of photons ($E = \hbar c|\vec{k}|$). The radiative generation or recombination of a negatively or positively charged exciton, i. e. a trion, however, is not bound to the light cone, as excess momentum can be transferred to the remaining electron or hole of the trion [48].

The excitonic transitions in TMDCs are named *A*, *B* and *C*. The *A* and *B* transitions stem from the spin-orbit split bands, while the commonly called *C* band or *C* exciton stems from multiple excitonic or band-to-band transitions throughout the Brillouin zone [14]. Spin-orbit interaction in TMDCs are strong, compared to, e. g. the relatively closely related graphene. This is mainly due to the heavy atoms as well as the contribution of the transition metal *d*-Orbitals to the VBM [14, 15, 49–51]. These splittings range from 150 meV (MoS₂) to several hundred meV (e. g. WSe₂) in the VBM at the *K* points [52]. In the conduction band maximum the splitting is much smaller (3-40 meV) [46]. The conduction band ordering is further dependent on the type of transition metal. This ordering leads to a bright excitonic ground state in Mo-based TMDCs, while W-based materials have a dark ground state [46, 50, 53, 54].

Classically excitons are classified into Frenckel- and Wannier-Mott-excitons. Frenckel-excitons have a small radius of about a unit cell and a higher binding energy whereas Wannier-Mott-excitons have a larger spatial extension and an accordingly lower binding energy. In 2D-TMDCs the Bohr radius of ≈ 1 nm [6, 14, 55, 56] corresponds to the Wannier-Mott type, yet with a much higher binding energy.

The measurement of the exciton binding energy as a simple difference of the optical band gap (exciton transition) and the onset of the band-to-band continuum transition (classically performed by absorption spectroscopy) is not possible as the

latter so far could not be observed directly. Experimental determination of the A exciton's binding energy has been performed by, e.g. absorption spectroscopy, investigating the quasi-Rydberg series [5–7], two-photon absorption [5, 8] or scanning tunneling spectroscopy [9, 10]. The results show a significant variation, but still determine the binding energy on the order of 0.5 eV for MoS_2 , approximately 1–2 orders of magnitude stronger than in conventional semiconductors, such as GaAs (4.9 meV [57]), GaN (27 meV [57]), ZnS (29 meV [57]) or ZnO (≈ 60 meV [58, 59]). The strong variation originates presumably from differences in the sample quality, but also from different substrates used in the experiments, different dielectric environments due to a different distribution of residue from the mechanical or chemical exfoliation process, or different adsorbates. All these differences might result in changes of the observables and even the binding energy itself (see below). This uncertainty also carries over to the determination of other physical properties and the turn over to applications.

The strong A and B exciton binding energy emerges as a consequence of several properties. First, the wave functions of the electron and the hole part of the excitons are confined to one layer (even in the bulk material) [14, 60] lowering the ground level in the attractive potential well, which is commonly known as the spatial confinement effect.

Second, the total energy of the exciton is scaled as a consequence of the dependence of the Hamiltonian and thereby of the energy eigenstates on the carriers' effective masses. In a simplistic approach, considering the hydrogen model to describe the exciton, with the reduced effective mass $\mu = (1/m_e^{\text{eff}} + 1/m_h^{\text{eff}})^{-1}$ of the electron and hole, and the contributions from the lattice combined in the relative dielectric constant $\epsilon_0 \rightarrow \epsilon_0 \epsilon_r$, the Hamiltonian reads

$$\vec{H} = \left(\frac{\hbar^2}{2\mu} \nabla^2 - \frac{e^2}{4\pi\epsilon_0\epsilon_r r} \right). \quad (2.5)$$

Solving Schrödinger's equation, considering the CBM (E_g) as the state of dissociate charge carriers, i. e. “zero energy” of the exciton system, and including the excitonic

2. Transition metal dichalcogenides: Structural and optical properties

dispersion in \mathbf{k} , the allowed excitonic eigenenergies read:

$$E = E_g - \frac{1}{2} \frac{\mu e^4}{(4\pi\epsilon_0\epsilon_r)^2 \hbar^2} \frac{1}{n^2} + \frac{\hbar^2 \vec{k}^2}{2(m_e + m_h)}, \quad (2.6)$$

which is also found in textbooks as the energy of a Wannier-Mott-exciton. The second term describes the exciton binding energy, in the case of the ground state $n = 1$. Here, the above claimed implication of the effective carrier masses (within μ) on the binding energy (E_b) is easily seen: a larger m^{eff} increases the absolute value of the binding energy. In MoS₂, the effective mass of the electron and hole forming an *A* exciton are about $m^{\text{eff}} = 0.5 m_0$ [61, 62],³ thus comparable to the magnitude of the carriers in ZnO [63], which is a high exciton binding energy, classical semiconductor. As a comparison in GaAs ($E_b = 4.9$ meV [57]) the masses of the electron and light hole (forming the GaAs-*A* exciton), are much smaller with $m_e^{\text{eff}} = 0.063 m_0$ and $m_{lh}^{\text{eff}} = 0.082 m_0$. [64]

And third, the screening further contributes to the large binding energy in TMDCs. This effect can also be read from equation 2.6 as the energy is a direct function of the dielectric constant. Due to its appearance in the denominator a material with low dielectric constant (in the volume of the exciton) will support a strong binding energy. This effect is especially strong in single-layer (SL) TMDCs due to their 2D-nature, as most of the Coulomb field is not within the material itself but outside, exposed to the (usually) very low dielectric constant of the surroundings (e. g. vacuum, air, low dielectric constant-substrates). Considering single-layer MoS₂ with its relatively low dielectric constant of $\epsilon_r \approx 3 \dots 4$ [65] ($\epsilon_r^{\text{ZnO}} = 7.8 - 8.8$ [66], $\epsilon_r^{\text{GaAs}} = 12.9$ [64]) one can calculate an increase of the binding energy by a factor of 2–4 (again compared to ZnO and GaAs), while the reduced screening in a free-standing single layer further increases the binding energy by another factor

³For the sake of clarity I only give an approximate value of the effective masses, since the values given in the literature are of large variation due to the applied approximations to the band structure calculations (which are used to calculate the masses). Further, the effective mass is not an isotropic constant at any \mathbf{k} but depends on the direction, e. g. at the *K* point in the high symmetry directions Λ , *T* or *P*. This is in contrast to excitons in classical semiconductors where the excitonic transitions are at the Γ point with isotropic effective masses.

of almost 4.⁴

Excitons can interact with several other quasi-particles to form new quasi-particles. This includes charged excitons, with an exciton binding to another electron or hole, biexcitons, two electrons and two holes stably bound, or excitons binding to defects. Each of these states can have a positive binding energy, i. e. can have lower state compared to the neutral, free exciton. Several of these can decay radiatively, resulting for some materials in spectra with a plethora of features.

In 2D TMDCs usually only the neutral and the charged excitons are observed. From luminescence as well as calculations the binding energy could be determined in the range of $E_{b,trion} = 18 \dots 40$ meV [67–71], depending on the type of TMDC. In contrast to conventional semiconductors the positively and negatively charged trions can not be easily distinguished, as similar effective masses of electron and hole lead to near degenerate binding energies. Gated PL measurements of mechanically exfoliated MoS₂ suggest that the negatively charged trion is the one predominantly observed [69], leading to the conclusion that mechanical exfoliation of MoS₂ leads to n-doped samples. Furthermore, SL MoS₂ transistors are exhibiting an n-type characteristic [72]. The doping is possibly caused by Rhenium, supposed to be present in natural molybdenite [73, 74].

Figure 2.5 presents PL spectra of WSe₂ in ambient and in cryogenic conditions. The room temperature emission exhibits only a broad peak at 1.66 eV originating from the exciton and trion emission. At low temperatures further insights into the electronic structure are possible: The neutral and charged exciton line widths shrink, so that a differentiation is possible. Further, multiple peaks arise below the A^- peak, which are defect induced “localized” or “trapped” excitons.

⁴The increase of the binding energy is approximately and not equally 4, since the electric field is not completely in the surrounding vacuum, but to some extent within the layer.

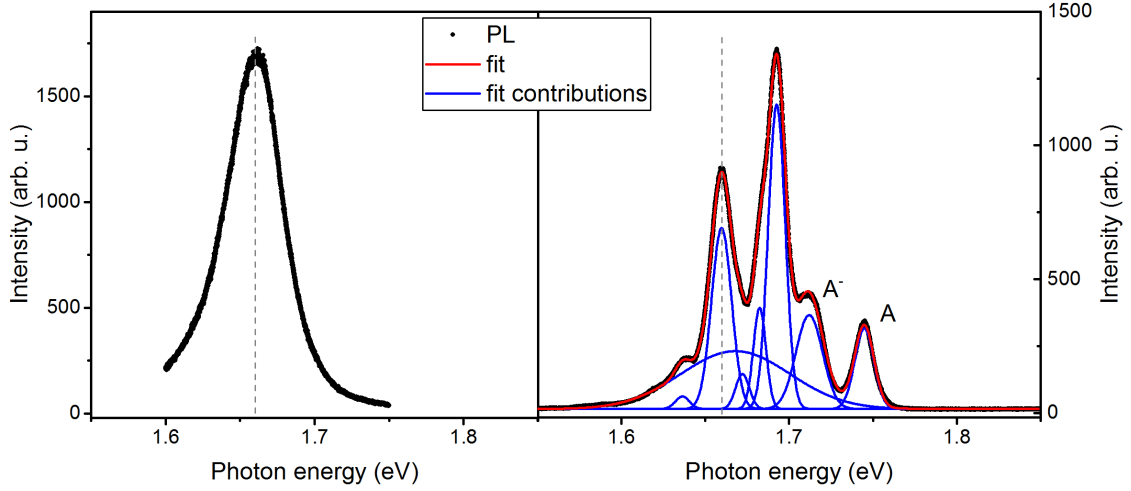


Figure 2.5.: Photoluminescence spectra of WSe₂ at room temperature (left) and 20 K (right) in vacuum. For the low temperature measurement distinct A and A^- peaks and low contributions of luminescent defect states (below 1.7 eV) are observable.

2.2.1.1. Valley polarization in single-layer TMDCs

Considering the excitonic transitions, it is useful to define the term *valley*, which describes a local minimum in the corresponding potential for a carrier in the BZ. Most prominent for TMDCs of the MoS₂-family are the electron and hole valleys at the K point, because of their direct transition. As a result of its hexagonal structure two energetically degenerate band gaps at the K points exist within the first BZ (Fig. 2.6 a); an electron being excited at this direct transition can either be located at the K or K' point. Therefore, the electron acquires a further, spin-like, binary information which can be defined as a *pseudospin*. This pseudospin describes in which valley the charge carrier is located.

Similar to the changes in symmetry of the crystal when the layer number is altered, the symmetry of high symmetry points also changes. This transition in symmetry results in a strict dependency of the electronic bands and the scattering selection rules on the number of layers. For example, second harmonic generation in the centrosymmetric even- N -layers is impossible, due to a vanishing $\chi^{(2)}$ -term in the susceptibility, while non-zero terms are existent in the single-layer's D_{3h}

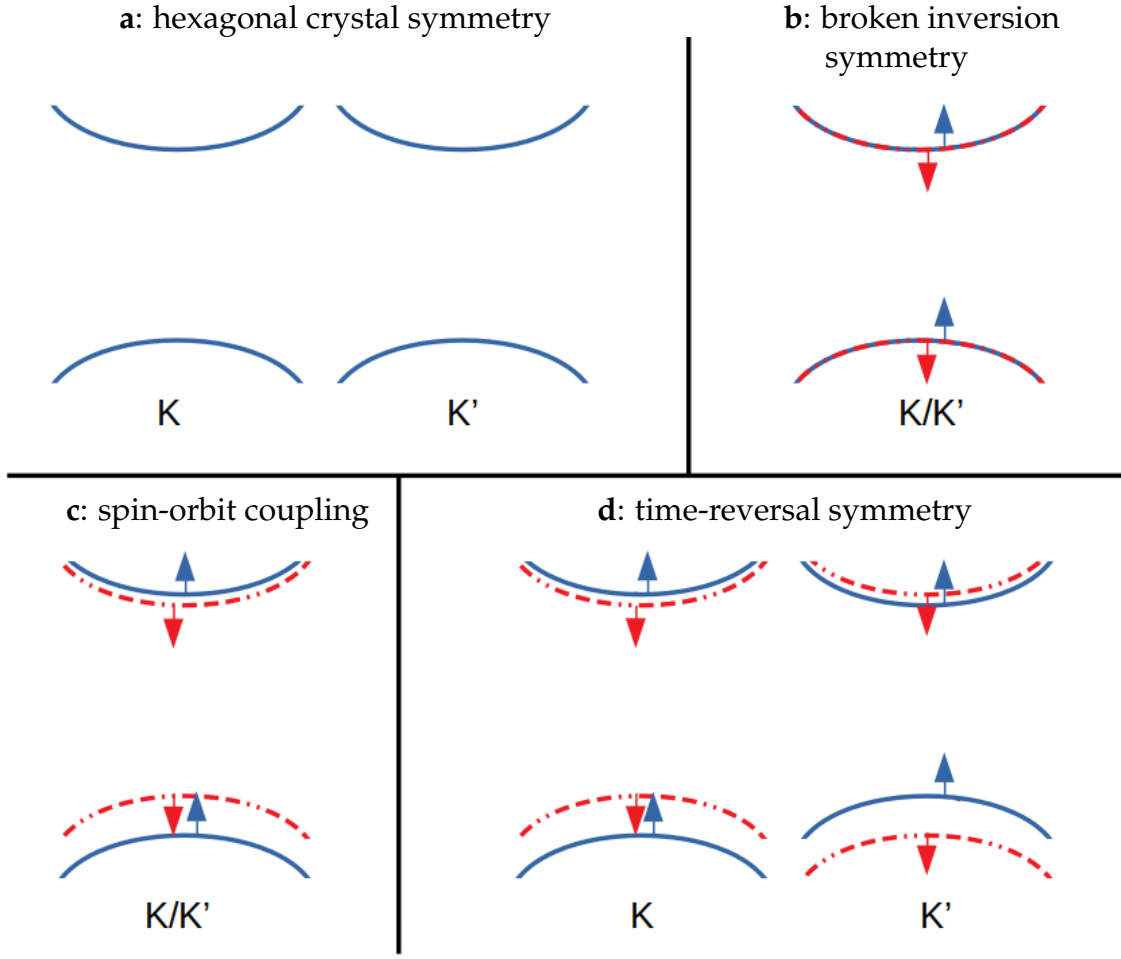


Figure 2.6.: Sketch of the single-particle band structure of the valleys at K and K' in D_{3h} TMDCs (odd-layer number) taking the hexagonal symmetry (a), broken inversion symmetry (b), spin-orbit coupling (c) and time-reversal symmetry (d) into account. Arrows depict the spin orientation.

point group [75]. Further, the non-existence of inversion in odd- N -layers results in opposite Berry curvatures at K and K' , which again describes an effective magnetic field with opposite sign [25]. This results in bands only containing either spin up or down charge carriers (Fig. 2.6 b). Adding the above described strong spin-orbit interaction, a system with energetically split bands is obtained [14, 15, 49–51] (Fig. 2.6 c). Finally, time-reversal symmetry implies that the spin orientation has to be opposite at opposite K points, leading to a coupling of spin and pseudospin, also called *spin-valley locking* (Fig. 2.6 d). Note that this is only exactly true at the K / K' points due to the loss of the C_{3h} symmetry (odd- N -layer) away from the

2. Transition metal dichalcogenides: Structural and optical properties

high-symmetry point.

For the excitation through the absorption of a photon or the radiative relaxation the selection rules demanded by the Laporte rule apply, i.e. that transitions are only allowed in between bands that are not originated from the same orbital and those exhibiting parallel spins ($\Delta l = \pm 1$ and $\Delta s = 0$) [14]. Following this selection rule and considering the spin-valley locking, further implications follow: Transitions for the A exciton are only allowed for the spin-down bands at K (following the example given in Fig. 2.6) or the spin-up bands at K' (the opposite applies for the B exciton). These excitons are called bright, other excitons (not allowed to radiatively decay) are called dark.⁵

As the electron and hole, which bind to excitons, underly the above described phenomena, formed excitons inherit these conditions. This allows for the observation of excitonic valley polarization [15, 18, 19].

Trion PL can be circularly polarized, however, linear polarization is highly unlikely,⁶ due to entanglement of the photon polarization with the pseudospin of the residual charge [68, 70].

To quantitatively address the degree of valley polarization, the contrast-like degree of circular polarization (DOP)

$$\rho = \frac{I_{\sigma^+} - I_{\sigma^-}}{I_{\sigma^+} + I_{\sigma^-}} \quad (2.7)$$

is introduced, with I_{σ^+} (I_{σ^-}) being the photoluminescence (PL) emission intensity of the σ^+ (σ^-) circular polarization.

⁵Note that most states associated with the bands allowing a radiative transition are dark, due to the further implication of the momentum conservation ('light cone'). However, to facilitate the discussion, excitons will also be named bright even if the momentum is larger than the photon-momentum as long as they obey the Laporte rule.

⁶In the case of negative trions, configurations exist where the the emission of linear polarized light is possible. However, for these states valley coherence is expected to be destroyed by exchange interactions [68]. For the positive trion state no configurations are present [68], which would in principle allow valley coherence, due to the large spin-orbit splitting of the valence bands.

2.3. Inelastic light scattering in TMDCs

To analyze the above described optical properties and potentially implement them in new applications, one generally needs to consider a reasonable set of perturbations to the system. Since experiments (or applications) are never running at $T = 0\text{K}$, the effect of temperature to the bare mathematical model of the unperturbed system has to be taken into account. The manifestation of the temperature in a crystal are the atoms' oscillations in the lattice. These oscillations can be either described as a plane wave-like motion in the crystal or as quanta called *phonons* moving through the lattice. The knowledge of a crystal's phononic properties is important, as they not only influence the above described valley physics, but also, e. g. provide relaxation channels for hot carriers, are the only source of the electronic resistance in an ideal crystal and play the most important role for heat transport in non-conducting materials.

Each crystal has $3N$ phonon branches, where N is the number of atoms in the unit cell. The unit cell of bulk 2H-MoS₂ contains 6 atoms, giving rise to 18 phonon branches. Each two of them form so-called a Davydov pair. Each of these pairs is formed by two modes, where the first one constitutes of layers performing the same oscillation as the single-layer, while for the second mode the phase of the oscillation of every other layer is shifted by π . For every pair one mode is even, while the other one is odd under inversion at the Γ point [60, 76]. While the frequency difference of the two modes is determined by the coupling strength of the individual layers, it is expected that the difference is small, for the layered TMDCs discussed in this thesis.

Reducing the crystal to a single layer, the number of atoms in the unit cell is 3 leading to 9 phonon branches. However, the energies of these phonon branches in most of the Brillouin zone are comparable to the bulk, as the vibrations are not altered much by the van-der-Waals bound neighboring layers. Major differences are the absence of the rigid layer modes in the SL limit and the slight blue (red) shift of the $E_{1g} / E_g / E'$ ($A_{1g} / A_{1g} / A'_1$) mode, commonly used for the layer number assignment [77–79].

2. Transition metal dichalcogenides: Structural and optical properties

Phonons can be detected through their interaction with other (quasi-) particles, e. g. electrons (electron energy loss spectroscopy, EELS), neutrons (inelastic neutron scattering) or photons⁷ (Raman scattering and inelastic X-ray scattering, IXS). EELS is in particular important to study surface physics, due to the low penetration depth of the electrons into the crystal at used low kinetic energies. However, the full dispersion relation of a crystal remains inaccessible by EELS on account of its limited momentum transfer and energy resolution. Also, the bulk dispersion remains inaccessible, in cases of crystals exhibiting a surface reconstruction. None of these limitations apply to INS. However, due to the limited abilities to focus neutrons and the low scattering cross section, one requires large mono-crystalline samples (on the order of $15 \times 15 \times 30 \text{ mm}^3$ [80]). Raman spectroscopy, the inelastic scattering of light in the visible range, again, lacks meaningful momentum transfer,⁸ but allows to measure zone center phonons with high energy resolution. Further, because of the polarization of electro-magnetic waves, selection rules apply (see below, sec. 2.3.2), that allow to differentiate Raman active phonons with similar energies. In recent decades, high resolution IXS has been developed, reaching energy resolutions up to 10^{-7} enabling to resolve phonons on the meV-scale [81–83]. As a consequence of the high photon energy of $\approx 2 \cdot 10^4 \text{ eV}$, the momentum transfer is not limited to the zone center,⁹ but also extends to the edges of the first BZ, even for materials with small lattice constants. In addition, hard X-rays can be focused on a spot of the size down to about $10 \times 10 \mu\text{m}^2$ [83], allowing IXS (as opposed to INS) to probe phonons in materials only accessible in limited quantities or with limited crystalline quality.

⁷In agreement with the above statement of photons only interacting with electrons (apart from core derived radioactive radiation, page 10), inelastic photon scattering relies on the Born-Oppenheimer-approximation, i. e. that electrons react faster than the nuclei are able to dislocate.

⁸The maximum momentum transfer is given in back-scattering geometry where $q = 2k_{\text{photon}}$. The momentum of a photon can be calculated by $|\vec{k}_{\text{photon}}| = 2\pi n / \lambda_{\text{photon}}$ which is $k_{633 \text{ nm}}^{\text{MoS}_2} \approx 2.0 \cdot 10^5 \text{ cm}^{-1}$ for the examples of photons from a HeNe-Laser in MoS₂ (refractive index $n = 2$ [65]). On the other side the momenta corresponding to the K and M points in MoS₂ are $k_K = 4\pi/3a \approx 1.3 \cdot 10^8 \text{ cm}^{-1}$ and $k_M = 2\pi/\sqrt{3}a \approx 1.2 \cdot 10^8 \text{ cm}^{-1}$ and are almost three magnitudes larger than the photon momentum, demonstrating that phonons probed with Raman spectroscopy are originated from the BZ center.

⁹ $k_{20 \text{ keV}}^{\text{MoS}_2} \approx 4 \cdot 10^9 \text{ cm}^{-1}$ exceeding the first BZ by more than an order of magnitude.

For the inelastic scattering both energy and momentum conservation have to be obeyed:

$$E_i = \hbar\omega_i = \hbar\omega_s \pm \hbar\omega_p = E_s \pm E_p \quad (2.8)$$

$$\vec{k}_i = \vec{k}_s \pm \vec{k}_p + \vec{H} = \vec{k}_s + \vec{Q}, \quad (2.9)$$

with the indices i , s , p describing the incoming and scattered photon and the phonon, respectively. \vec{H} and $\vec{Q} = \pm\vec{q} + \vec{H}$ are a reciprocal lattice vector and the total scattering vector. The \pm describes the creation or annihilation of the phonon.

2.3.1. Inelastic X-ray scattering

The dispersion of a phonon can be measured by IXS by measuring the phonon energy at different momenta within the irreducible part of the first BZ (or equivalent momenta), which can be selected through the scattering geometry. From the scattering geometry, depicted in figure 2.7, one can deduce that the absolute value, i. e. the length, of the total scattering vector $Q = |\vec{Q}| = |\vec{k}_i - \vec{k}_s|$ depends on the scattering angle, spanned by \vec{k}_i and \vec{k}_s :

$$Q^2 = k_i^2 + k_s^2 - 2k_i k_s \cos(2\Theta) \quad (2.10)$$

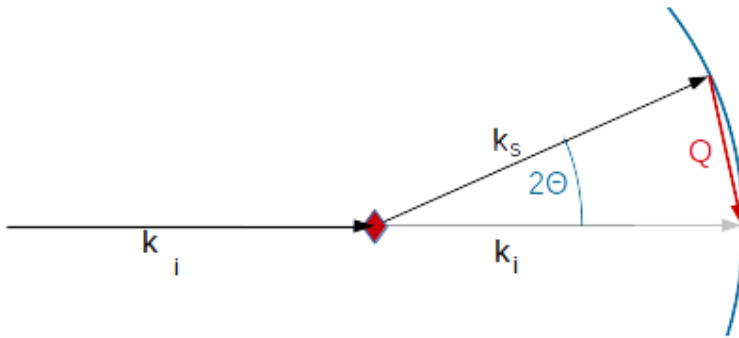


Figure 2.7.: Inelastic scattering process of a photon with wave vector \vec{k}_i at a scattering center (red diamond). The arrow \vec{k}_s depicts the scattered photon and the blue circle marks the equi-momentum circle with radius $r = k_i \approx k_s$.

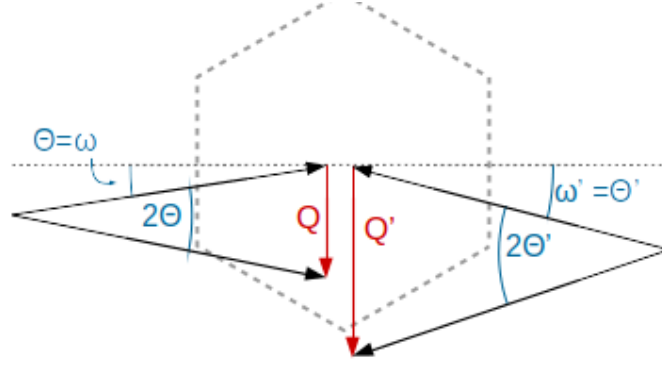


Figure 2.8.: Depiction of different scattering geometries in a $\Theta - 2\Theta$ scan resulting in parallel scattering vectors with different lengths (along the $\Gamma - K$ direction). The horizontal dotted, gray line depicts the $[100]$ direction in the indicated hexagonal reciprocal space.

Considering a small change of the magnitude of the photon wave vector, i. e. $|\vec{k}_i| \approx |\vec{k}_s|$ the dependence of the scattering angle on Q can be given as the chord spanned by the photon wave vectors in the circle with radius $r = k_i \approx k_s$ (cf. Fig. 2.7, blue circle segment):

$$Q \approx 2k_i \sin(\Theta). \quad (2.11)$$

Now, considering crystal-fixed coordinates (see figure 2.8) allow to define the angle of the incident photon ω . With this additional freedom of creating the scattering geometries, it is possible to perform a $\omega - 2\Theta$ scan with $\omega = \Theta$. Due to the geometric implications all scattering vectors \vec{Q}_Θ are parallel, however, with its magnitude as a function only depending on Θ , as of equation (2.11). This method allows to measure along radial lines (from the origin) in the reciprocal space.

For a detailed introduction into the inelastic scattering of X-rays, the reader is referred to the excellent reviews and books [81, 82, 84–86].

2.3.2. Raman scattering

A simple approach to Raman scattering is the derivation of the Raman tensor from macroscopic electrodynamics.¹⁰ The electric field \vec{E} of an incoming photon

$$\vec{E}(\vec{r}, t) = \vec{E}_i(\vec{k}_i, \omega_i) \cos(\vec{k}_i \cdot \vec{r} - \omega_i t) \quad (2.12)$$

induces a polarization \vec{P} in the medium

$$\vec{P}(\vec{r}, t) = \chi(\vec{k}_i, \omega_i) \vec{E}_i(\vec{k}_i, \omega_i) \cos(\vec{k}_i \cdot \vec{r} - \omega_i t). \quad (2.13)$$

Phonons in the medium can be described as

$$\vec{Q}(\vec{r}, t) = \vec{Q}(\vec{q}, \omega_p) \cos(\vec{q} \cdot \vec{r} - \omega_p t), \quad (2.14)$$

with \vec{q} (ω_p) denoting the wave vector (angular frequency) of the phonon. Changes of the phonons on the susceptibility are small (if at all present), allowing to approximate χ through a Taylor series

$$\chi(\vec{k}_i, \omega_i, \vec{Q}) = \chi_0(\vec{k}_i, \omega_i) + \left(\frac{\partial \chi}{\partial \vec{Q}} \right)_0 \vec{Q}(\vec{r}, t) + \dots \quad (2.15)$$

By inserting (2.15) up to the first order in (2.13), one obtains two summands. The first term (zeroth order) is of the same energy as the incident light and represents the elastically scattered light:

$$\vec{P}_0(\vec{r}, t) = \chi_0(\vec{k}, \omega_i) \vec{E}_i(\vec{k}, \omega_i) \cos(\vec{k}_i \cdot \vec{r} - \omega_i t), \quad (2.16)$$

¹⁰Since this is a common approach, overlap with standard textbooks is likely, e. g. with reference [57].

2. Transition metal dichalcogenides: Structural and optical properties

while the second term (first order) is induced by phonons:

$$\vec{P}_{\text{ind}}(\vec{r}, t, \vec{Q}) = \left(\frac{\partial \chi}{\partial \vec{Q}} \right)_0 \vec{Q}(\vec{q}, \omega_P) \cos(\vec{q} \cdot \vec{r} - \omega_P t) \cdot \vec{E}_i(\vec{k}_i, \omega_i) \cos(\vec{k}_i \cdot \vec{r} - \omega_i t) \quad (2.17)$$

$$\begin{aligned} &= \frac{1}{2} \left(\frac{\partial \chi}{\partial \vec{Q}} \right)_0 \vec{Q}(\vec{q}, \omega_P) \vec{E}_i(\vec{k}_i, \omega_i) \\ &\quad \cdot \left(\cos [(\vec{k}_i + \vec{q}) \cdot \vec{r} - (\omega_i + \omega_P)t] \right. \\ &\quad \left. + \cos [(\vec{k}_i - \vec{q}) \cdot \vec{r} - (\omega_i - \omega_P)t] \right), \end{aligned} \quad (2.18)$$

where the addition theorem $\cos(a) \cos(b) = \frac{1}{2} [\cos(a - b) + \cos(a + b)]$ has been used on equation (2.17). Consequently the electric dipole momenta which sum up to the macroscopic polarization consist of oscillations with frequencies ω_i (Rayleigh), $\omega_i + \omega_P$ (Anti-Stokes) and $\omega_i - \omega_P$ (Stokes). Including higher orders of the Taylor series will enable to calculate the higher order Raman scattering processes.

The factor

$$\vec{R}_{ijm} = \left(\frac{\partial \chi_{ij}}{\partial \vec{Q}_m} \right) \quad (2.19)$$

is the 3rd rank Raman tensor, which holds the information of scattering probabilities, and thereby the selection rules and scattering intensities. The indices i and j run over the three space coordinates, while m represents all possible phonons.

The 2nd rank Raman tensors of the Raman active modes in bulk (odd-layer) TMDCs with D_{6h} (D_{3h}) symmetry are [87]:

$$\begin{aligned} A_{1g} (A'_1) : & \begin{pmatrix} a & & \\ & a & \\ & & b \end{pmatrix} & E_{1g} (E'') : & \begin{pmatrix} & & \\ & & c \\ & c & \end{pmatrix} & E_{1g} (E'') : & \begin{pmatrix} & & -c \\ & & \\ -c & & \end{pmatrix} \\ E_{2g} (E') : & \begin{pmatrix} & & d \\ & d & \\ d & & \end{pmatrix} & E_{2g} (E') : & \begin{pmatrix} d & & \\ & -d & \\ & & \end{pmatrix} \end{aligned}$$

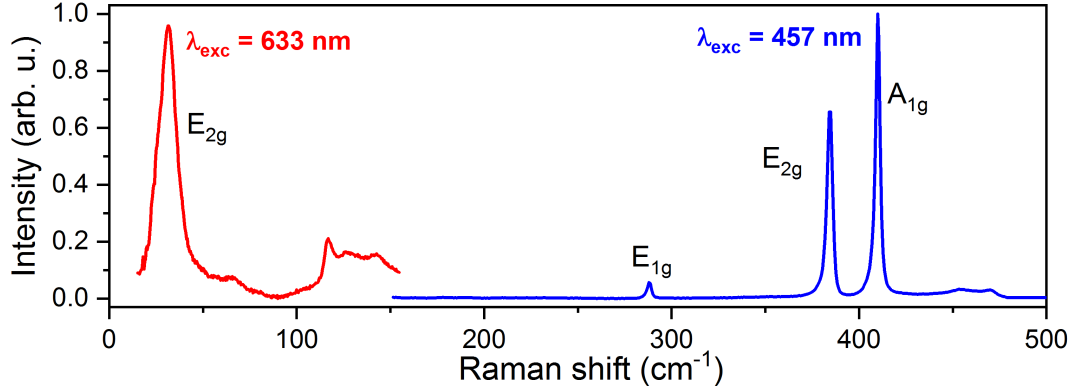


Figure 2.9: Typical Raman spectrum of bulk MoS₂ at room temperature. The low (high) energy part of the spectrum has been acquired using an 633 nm (457 nm) excitation. The labels give the irreducible representation of the corresponding Raman mode. Peaks without labels are originated by second order scattering processes.

while for even-N layer TMDCs with D_{3d} symmetry the Raman tensors read [87]:

$$A_{1g} : \begin{pmatrix} a & & \\ & a & \\ & & b \end{pmatrix} \quad E_g : \begin{pmatrix} c & & \\ & -c & d \\ & & d \end{pmatrix} \quad E_g : \begin{pmatrix} & -c & -d \\ -c & & \\ -d & & \end{pmatrix}.$$

Figure 2.9 depicts a Raman spectrum of bulk MoS₂ in near-backscattering geometry, showing four out of the five Raman active modes. Peaks not labeled with irreducible representations are originated by higher order scattering processes.

3. Experimental techniques

In this chapter I will give an introduction to the sample preparation through mechanical exfoliation and give details about the optical characterization. Further, experimental setups will be described.

3.1. Sample preparation

The idea of creating thin films of layered materials like MoS₂ is rather old, as, for example, Frindt *et al.* [2] produced continuous crystals of less than 10 nm thickness in the 1960s by peeling thin sheets off bulk material. Initially, adhesive tape was only used to fixate thin films over, e.g. holes to acquire freestanding samples [2]. Not long after, Frindt *et al.* [88] realized that adhesive tapes could be used to further thin down the sample to produce few-layer crystals. In their experiment, they observed crystals as thin as 35-40 Å (6 layers) [88]. It was, however, not until the experiments of Novoselov *et al.* [89] in the 2000s that single layer crystals of any layered material had been observed in a top-down approach.¹ The used technique is in principle the same which was presented in the experiments of Frindt *et al.* [88] in the 1960s. The difference of the techniques is that Novoselov *et al.* [89] used silicon with a surface layer of silicon oxide on the order of 100 nm instead of mica. This enabled the visual observation of single layers, and hence decouples the observation from sophisticated methods such as transmission electron microscopy. By using a substrate-system with a thin surface layer with different refractive index interference effects become important. In the case of the pure substrate (Si/SiO₂) the spectral composition

¹The first observation of single-layer graphite was 1962 by Hanns-Peter Boehm and co-workers [90]. In their study graphite oxide was reduced, resulting in small graphene flakes.

3. Experimental techniques

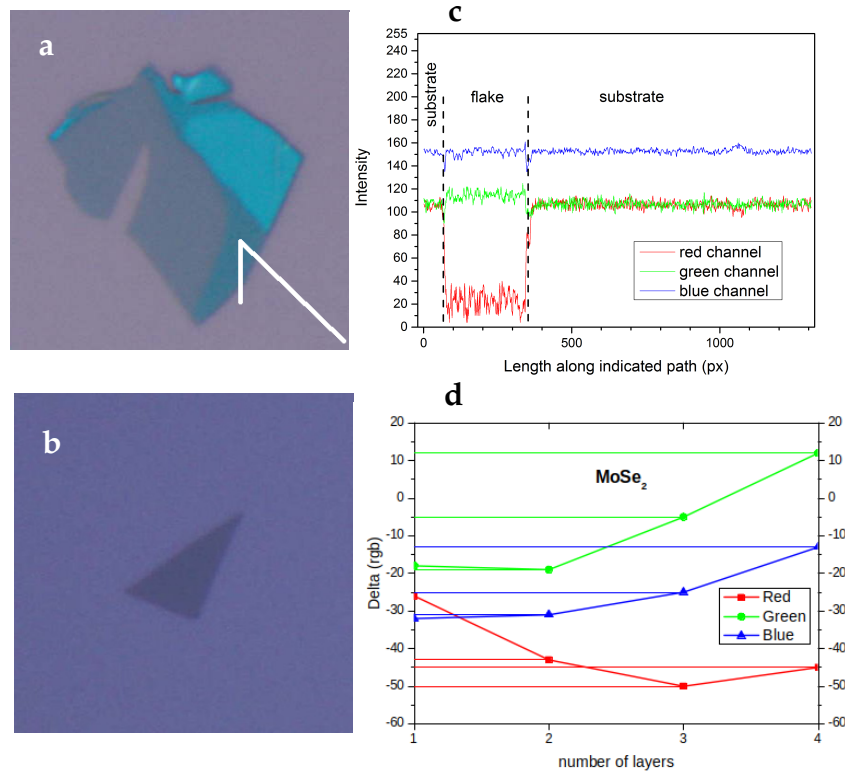


Figure 3.1.: **a, b** Optical microscope images of exemplary MoS₂ and MoSe₂ flakes; images depict an area of $20 \times 20 \mu\text{m}^2$. **c** RGB values of the pixels along the shown path in **a**. **d** evolution of the RGB differences to the substrate RGB with the layer number. Exemplarily shown for MoSe₂.

(color) of reflected white light is dependent on the thickness of the oxide layer, as the wavelengths, subject to constructive or destructive interference, are dependent on the oxide layer thickness [91]. A thin (third) layer atop the oxide alters the conditions for these interferences such that the color changes again, leading to a contrast compared to the bare substrate (cf. Fig. 3.1).

Since the thickness of a single layer is small compared to the wavelength of visible light, changes are small as well, but observable by eye under magnification. Furthermore, the small thickness leads to a gradual change of contrast with the number of layers rather than an oscillating intensity which would be expected for slabs with a thickness of, e. g. half the wavelength (dielectric mirror). The gradual evolution of the color makes it possible to observe this effect by solely using an optical microscope and allows the direct characterization of the layer number by

means of the RGB-values (see Fig. 3.1 c, d) [92]. This allows to quickly scan large areas for crystals of the desired thickness in contrast to techniques like atomic force microscopy (AFM).

A further difference in the procedure described in the works of Novoselov *et al.* [89] is that bulk material is directly put onto the adhesive tape instead of peeling very thin sheets off the bulk material. A thinning prior to the deposition on the substrate is performed by repeated folding of the tape and thereby repeated cleavage of the multi-layer crystal until eventually thin few-layer crystals remain on the tape. In this step, a trade off between low layer number on the tape (possibly a high yield of single-layers on the substrate) and flake size has to be made. With each cleavage step layers have a chance to tear, possibly due to direction of peeling, their structural environment fixating the layer to one or the other side of the tape or regions with lower structural strength, e. g. due to defects.

When the material is pressed onto the substrate the layer at the interface strongly connects to the SiO₂, keeping it in place when removing the tape.² By chance cleavage occurs above the Nth layer, when the tape is removed, leaving a N-layer crystal on the substrate.

Since this method of producing thin crystals is a top-down-process, the sample quality is directly dependent on the bulk material quality. For MoS₂ natural crystals are abundant. However, other TMDCs are only available in a synthetic form. Both origins comprise samples exhibiting cm-scale hexagonal structures, suggesting excellent mono-crystallinity. The lateral size of individual sheets within the bulk is only on the order of up to a few hundred microns for MoS₂ or few tens of microns for WS₂ [93]. Therefore, the maximum lateral size of single- or few-layers is limited to the sheet-size within the bulk material. Further, chemical and structural defects (impurities, dislocations, etc.) are inherited from the bulk crystal making good starting materials paramount.

Other possibilities of creating single- or few-layer crystals include chemical exfoliation [94–96] and van der Waals epitaxy or chemical vapor deposition [45, 97–101].

²For the samples produced for this thesis, a resting time of 24-48 h with mild pressure in ambient conditions has been used.

3. Experimental techniques

Samples used for the work presented in this thesis were prepared by mechanical exfoliation with 3M Scotch Magic Tape 810. Figure 3.2 depicts an AFM micrograph of a typical mechanically exfoliated WSe₂ flake on SiO₂. Sub-figure **a** shows the full flake, while a $1 \times 1 \mu\text{m}^2$ zoom of the right edge of the flake is shown in sub-figure 3.2 **b**. The height profile along the line indicated in sub-figure 3.2 **b** is presented in sub-figure 3.2 **c** exhibiting a step height of approximately 1 nm with a peak of additional 2 nm at the edge. The former represents the thickness of the single-layer plus additional thickness from adsorbed molecules on the interface. The peak at the edge might indicate that the edge curls upward to release strain, potentially caused by wrinkles (vertical bright lines). A further cause for the high edge might be the direction of exfoliation. When the adhesive tape was peeled off the substrate and flake it could lift the edge. Attractive forces to the substrate restrain the flake from lifting off leaving only the edge levitated. Again, the wrinkles could stabilize this bent structure.

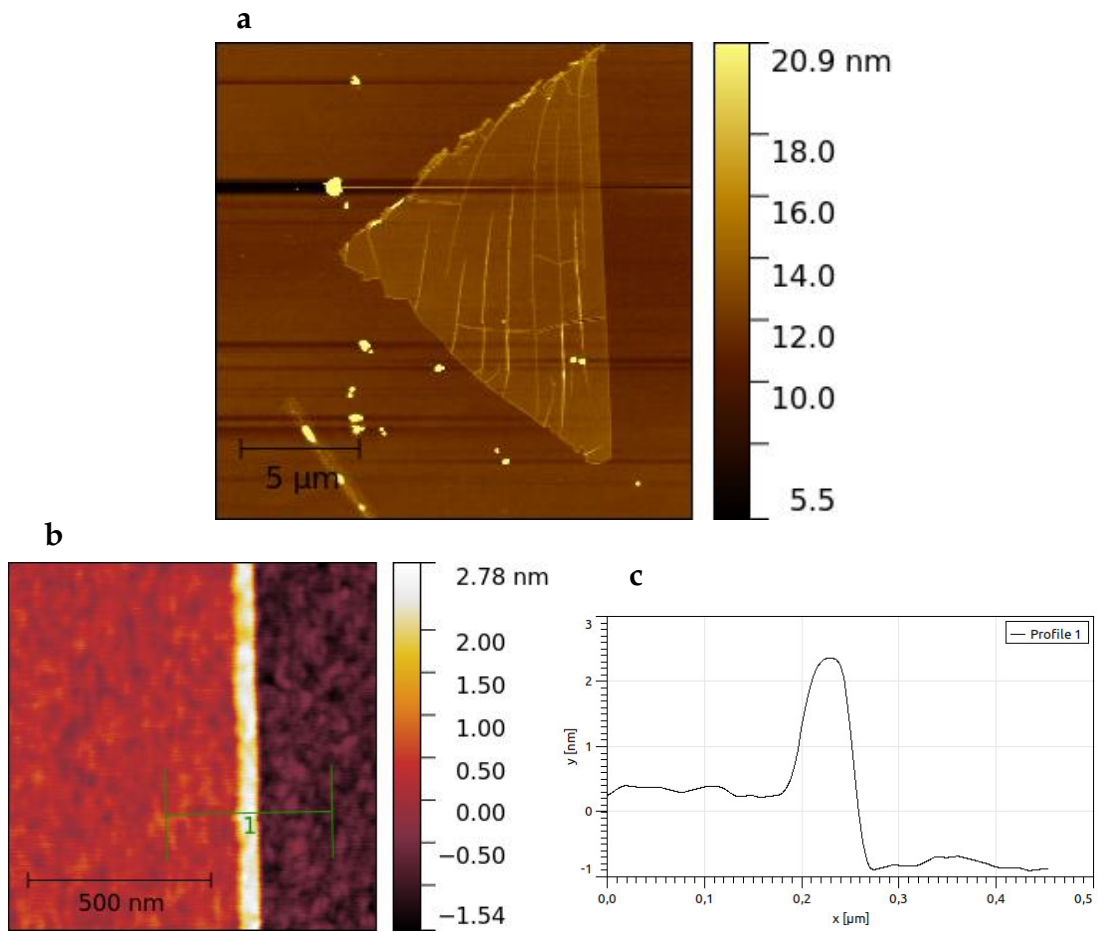


Figure 3.2.: AFM micrograph of a typical single-layer WSe₂. Sub-figure **b** depicts a $1 \times 1 \mu\text{m}^2$ zoom of the right edge of the flake. **c** is the height profile indicated in **b**.

3.2. Optical spectroscopy

All Raman, photoluminescence (PL) and photoluminescence excitation (PLE) spectroscopy experiments were performed on two different setup types: (i) a triple-monochromator setup with a wide range of laser sources (this lab will be referred to as the "XY") and (ii) in laboratories using a single-monochromator setup equipped with a set of solid-state and gas lasers and corresponding filters for laser light attenuation (the "LabRAM" labs). Both setup types will be introduced in detail in the following sections.

Generally, all optical measurements were performed in microscope-setups and in backscattering geometry. Spectral calibration has been performed using a low-pressure neon lamp, and taken prior to changes of the spectral position of the monochromators. Further, to correct the (polarization dependent) system-response of the setup the unpolarized light of an Avantes AvaLight-HAL-CAL was used as a standard. These corrective measurements were performed during each series of measurements.

For low temperature measurements, a cold-finger micro-cryostat was used with liquid helium as cooling agent. If not otherwise stated, a temperature of 20 K was set. During a series of measurements, the number of temperature cycles was kept at a minimum to avoid induced changes from e. g. changing dielectric environment due to absorbed water. Further, except for power series measurements, the power density was always kept below $\approx 10^8 \text{ W/m}^2$ ($260 \mu\text{W}$ on a $\approx 2 \mu\text{m}$ laser spot) for MoS_2 and MoSe_2 and below $\approx 10^7 \text{ W/m}^2$ ($26 \mu\text{W}$) for WS_2 and WSe_2 to avoid damage and excessive heating. Figure 3.3 depicts a power series measurement of a MoS_2 -SL, showing that temperature effects become observable only at powers above approximately $500 \mu\text{W}$ as indicated by the reduced emission energy (through the change of the band gap energy, i.e. Varshni's equation). Furthermore, the power series measurements prove laser induced changes, which were also observed by Cadiz *et al.* [102]: At low laser power only the exciton emission is observed (red dots), however, when a power threshold is overcome the exciton emission shifts and a trion peak emerges (black symbols). Although the used power in regular measurements has to be considered high, laser induced changes are not considered to

happen, as $260 \mu\text{W}$ is still below the threshold (red star).

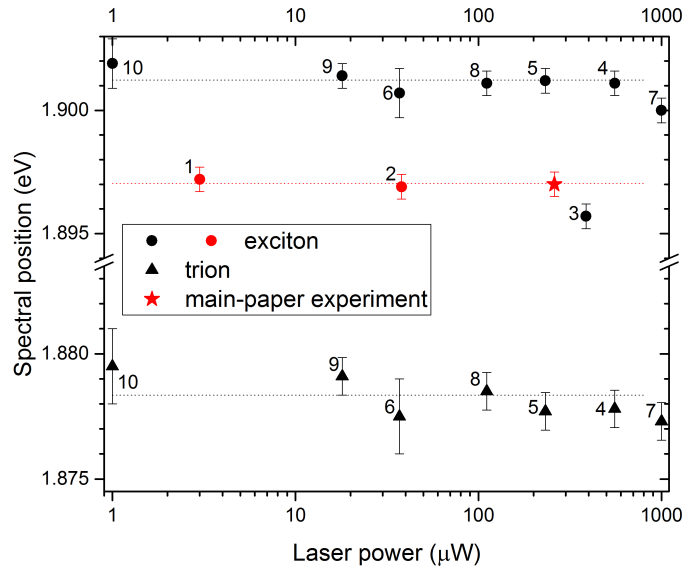


Figure 3.3.: Spectral position of the A exciton and A^- trion of SL MoS₂ as a function of the excitation power at a temperature of 20 K. Horizontal lines depict average values, excluding the measurement at $1000 \mu\text{W}$.

3.2.1. The XY laboratory

The XY-lab gained its name from the there used Dilor XY 800 triple-monochromator. In standard operation mode, the two first monochromators are set to subtractive operation, allowing to use these two as a continuously tunable, narrow bandpass. The third monochromator is used to disperse the filtered light onto a liquid-nitrogen cooled CCD. All three monochromators have a focal length of 800 mm and are equipped with a 1800 lines/mm grating. Thereby a spectral resolution of about 1.5 cm^{-1} is achieved at 650 nm with a slit opening of $200 \mu\text{m}$.

The strength of this system is the flexibility in excitation, since no filters are used restricting the operation to specific wavelengths.

As light sources a variety of lasers is used: An ArKr mixed-gas laser with discrete

3. Experimental techniques

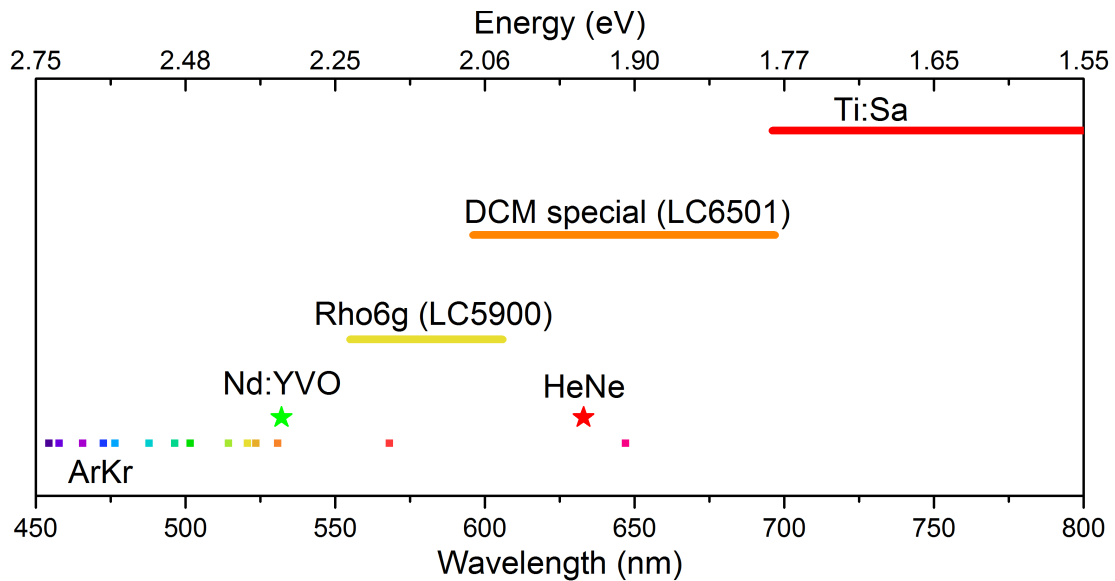


Figure 3.4.: Excitation energies / wavelengths available in the XY lab.

emissions between 452 nm and 647 nm³ and a HeNe gas laser at 633 nm. Further, a titanium sapphire and two dye lasers, pumped by a frequency-doubled Nd:YVO laser were used to obtain continuously tunable emissions in the ranges 579–606 nm (1 g/L Rhodamine 6g (LC5900) in ethylene glycol), 599–697 nm (0.69 g/L DCM Special (LC6501) in a 2:1 mixture of ethylene glycol and butyl alcohol) and 695–848 nm (Ti:sapphire).⁴ Furthermore, the 532 nm emission of Nd:YVO pump laser can also be used directly.⁵ All lasers are continuous wave lasers. An overview of the emission ranges of the available lasers is depicted in figure 3.4.

All lasers (following the beam path in the lab sketch in Fig. 3.5) are guided onto the same optical axis which is fed into a 30 cm flint prism-premonochromator, allowing to clean the beam from undesired plasma emission lines of the gas lasers or luminescence background of tunable lasers. Alternatively, a bypass of the premonochromator can be used in combination with interference filters. After the chromatic beam clean-up, a cascade of neutral density (ND) filters and a continu-

³More lines can be made available using different sets of mirrors.

⁴An extended emission range in the infra-red, up to ≈ 1100 nm, is possible using a different set of cavity mirrors.

⁵Even though this is only a pump laser, the spectral quality of the emission line (full width at half maximum of $\Delta\omega \lesssim 1.5 \text{ cm}^{-1}$, at $100 \mu\text{m}$ slits) and the low background at higher wavelengths allow to perform Raman experiments.

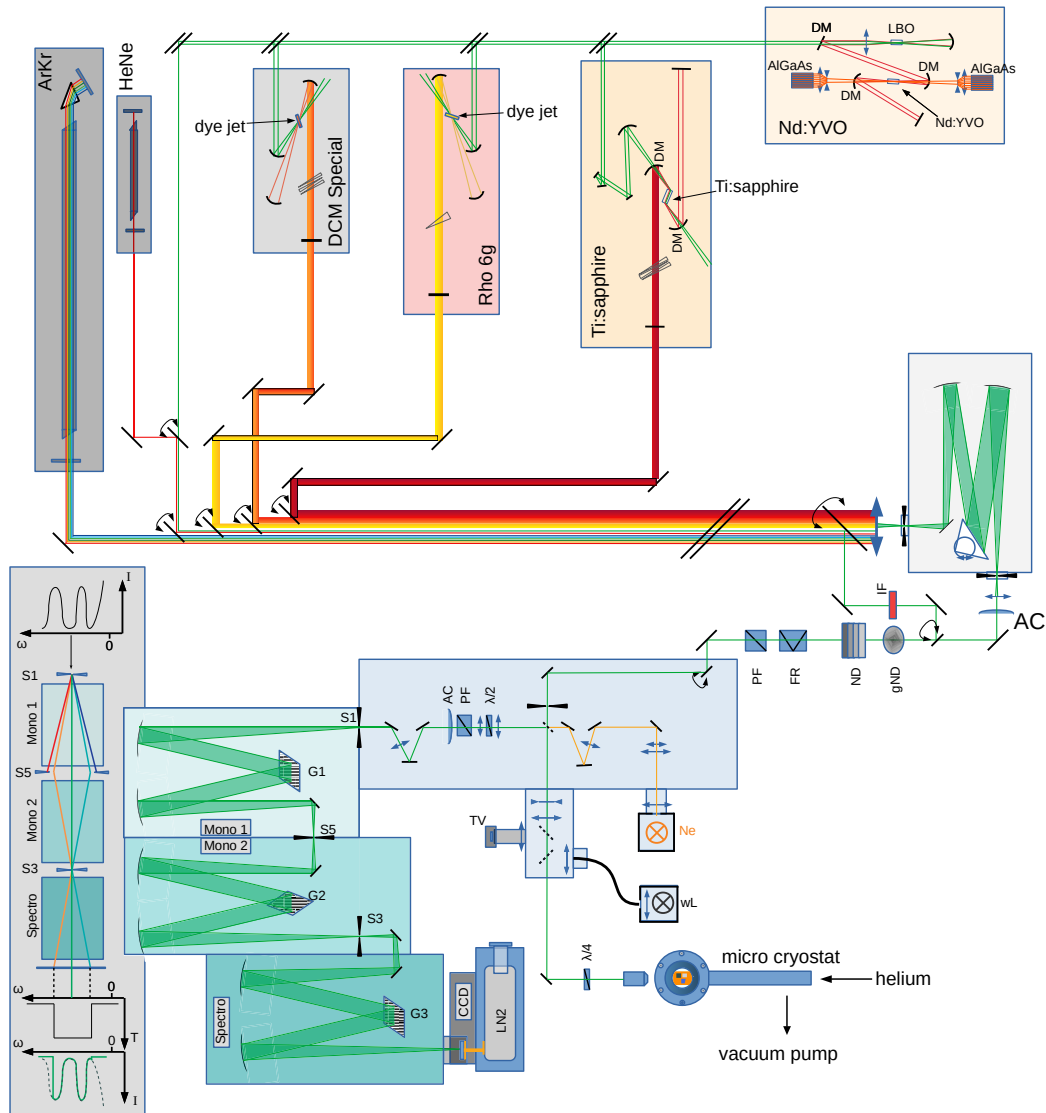


Figure 3.5.: Layout of the XY-laboratory. The inset (box in the lower left) depicts the spectral dispersion in all three monochromators and thereby the working principle of the variable bandpass using the subtractively coupled foremonochromators.

Description of symbols: \diagup (DM): high reflection (\diagdown dielectric) plane and focussing mirror, LBO: frequency doubling crystal (lithium triborate), \uparrow : lens, AlGaAs: pump laser stack (40 W), \parallel : beam lift, --- : Lyot filter, --- : flip-mounted mirror, $|$: slit $|$ (AC): astigmatism corrective cylindric lens, --- \bullet (ND / gND): ND filter cascade and gradual ND filter wheel, --- (FR): Fresnel rhomb, --- (PF): polarizing beam splitter, IF: interference filter, --- : beam splitter, TV: video camera, wL: white light source, Ne: neon calibration lamp, --- $\lambda/4$ ($\lambda/2$): achromatic quarter (half) waveplate, S1-5: monochromator slits, G1-3: monochromator gratings.

3. Experimental techniques

ous ND filter wheel are used to set the desired excitation power. Subsequent, the polarization of the beam is rotated to the desired orientation using a Fresnel rhomb and guided through a polarizing beam-splitting cube to achieve a clean linear polarization before entering the microscope. For circularly resolved measurements an achromatic quarter-wave plate is mounted just above the objective lens to avoid distortions induced by optics with e. g. different reflectivities for *s*- and *p*-polarization. The emitted circular polarized luminescence is converted to linear polarization with the same quarter-wave plate, while selection of the respective polarization is performed by a combination of an achromatic half-wave plate and a linear polarizer, fixed in the favored orientation of the Blaze grating. Further, to reduce the effect of providing out-of-plane photon momentum to the sample, relatively low numerical aperture objective lenses were used (e. g. Olympus LMPLAN F1 50x, NA=0.5).

3.2.2. The LabRAM laboratory

For Raman and PL spectra Horiba LabRAM800 HR spectrometers were used. These setups impress by their sensitivity (compared to a triple monochromator), which is achieved by using a notch or edge filter allowing the use of only one monochromator. Consequently, the LabRAM systems are used when no specific excitation energy is needed.

As excitation sources several gas lasers (Ar⁺: 488 nm and 514 nm; HeNe: 633 nm) and solid state lasers (457 nm, 830 nm, 532 nm) are available. The lasers are chromatically cleaned through interference filters and are reflected into the microscope by the notch or edge filter. The light emitted by the sample reaches the filter and is either reflected (within the filtering band) or transmitted. The transmitted light is guided into the monochromator which is equipped with a 600 lines/mm and a 1800 lines/mm grating. The spectra are recorded by Peltier-cooled CCDs.

The filters allow measurements starting at approximately 100 – 250 cm⁻¹ (low energy side of the laser, i.e. Stokes). For the HeNe laserline an ultra low frequency notch filter set is available, enabling measurements around 20 cm⁻¹.

Depending on the type of material and used measurement conditions (e.g. a cryostat) different objective lenses were used.

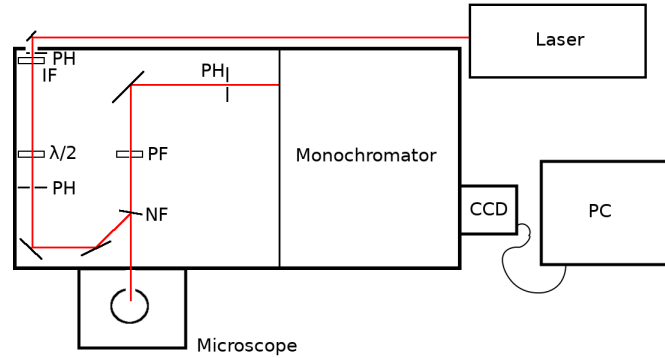


Figure 3.6.: Layout of the LabRAM-laboratories. IF: interference filter, PH: pin hole, $\lambda/2$: achromatic half wave plate, NF: notch filter, PF: polarization filter).

3.3. Inelastic X-ray scattering

3.3.1. High resolution IXS beamlines BL35XU (SPring-8, Japan) and ID28 (ESRF, France)

Inelastic X-ray spectra were recorded at beamlines 35XU at the Super Photon ring – 8 GeV (SPring-8, Japan) and the European Synchrotron Research Facility (ESRF, France). A depiction of the beamline layouts is found figure 3.7. A beam with a photon energy of 17.7935 keV with a spectral width of $\lesssim 3$ meV (FWHM) was obtained by using a liquid-nitrogen cooled Si (111) high heat load premonochromator, reducing the FWHM to ≈ 1 eV. The final width was created with a near-backscattering main monochromator of which the Si (999) reflex was used. At the SPring-8, the beam was then focused onto the sample with a spot size of $75 \times 63 \mu\text{m}^2$, allowing to select a single crystalline domain of the investigated bulk MoS₂ crystal. At the ID28 a spot size of $20 \times 20 \mu\text{m}$ was achieved by using a set of Kirkpatrick-Baez mirrors (KB) [103]. The scattered photons were analyzed at BL35XU (ID28) by an array of 3x4 (1x9) bent Si (111) analyzers, attached to

3. Experimental techniques

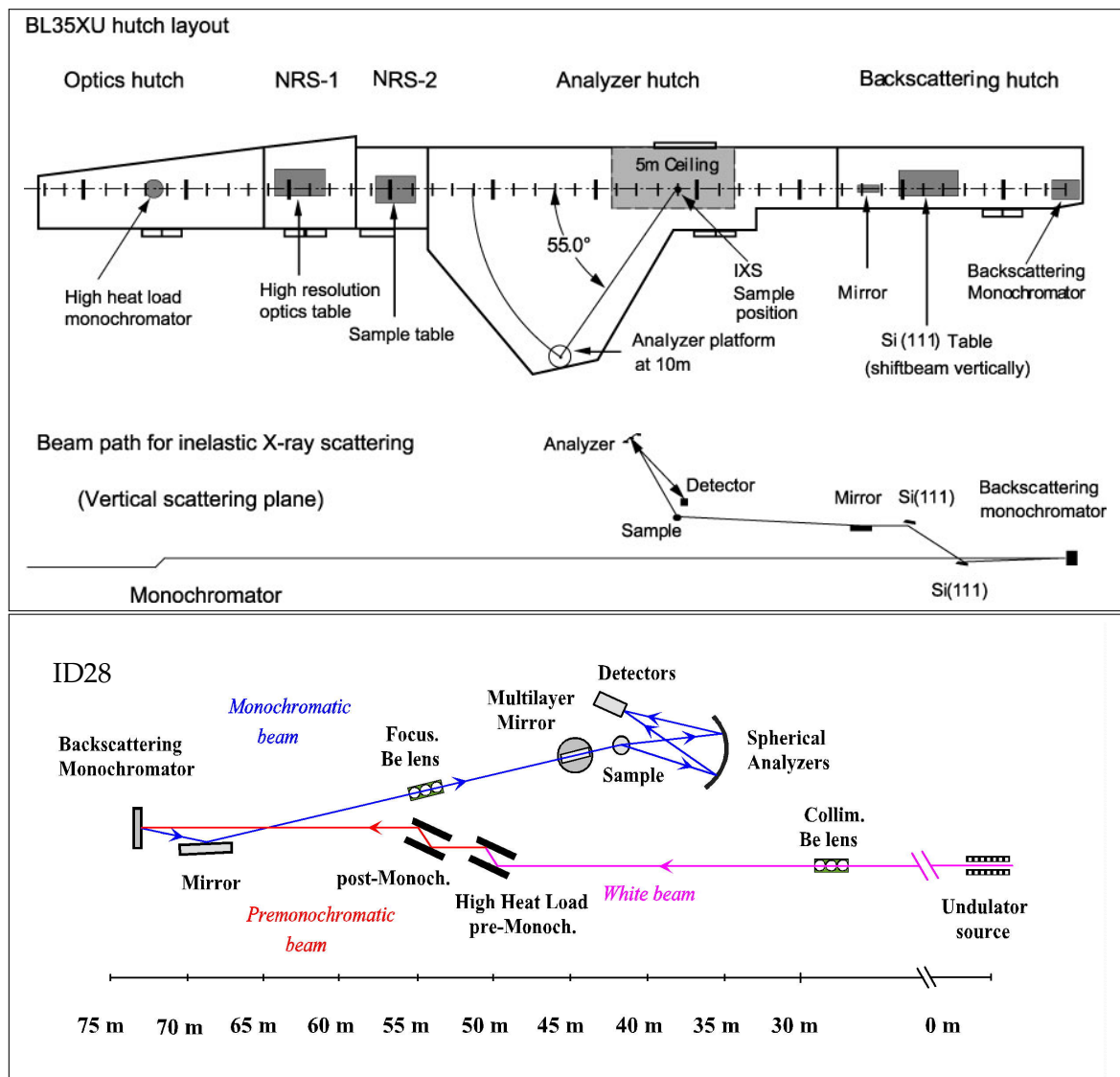


Figure 3.7.: Layouts of the beamlines BL35XU at SPring-8 (Japan) [104] and ID28 at the ESRF (France) [105].

the 9.8 m (7 m) monochromator arm. Figure 3.8 depicts the analyzers' positions in the reciprocal space for the measurements on MoS_2 of the longitudinal modes in $\Gamma - K - M$ direction. A detailed description of the beamlines can be found in Refs. [106] and [107].

The measurements were performed by keeping the scattering wave vector Q (and thereby the phonon wave vector q) constant and scan the energy by varying the temperature of the backscattering main monochromator. The twelve analyzers

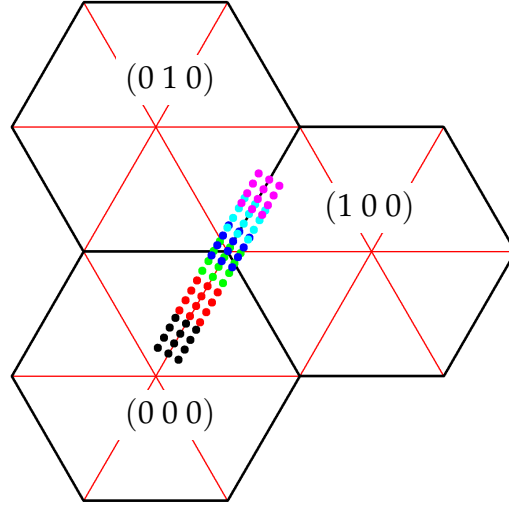


Figure 3.8: Positions of the 3×4 analyzers in the reciprocal space during the measurements of the MoS₂-phonons (SPring-8) in Γ - K - M direction with longitudinal oscillation component. Each color depicts one individual scan at a distinct \mathbf{Q}_{ctr} along $(h h 0)$.

were kept at a fixed energy (i.e. temperature). To verify that no significant energy shifts of analyzers and main monochromator have occurred, Stokes-anti-Stokes pairs of inelastically scattered photons were measured frequently.

The measurements on MoS₂ were performed in reflection geometry for ΓA longitudinal and all out-of-plane transverse modes and in transmission for ΓM , ΓK and KM longitudinal and in-plane transverse modes. The transmission and reflection scattering geometries were chosen to minimize the footprint of the beam within the sample, to reduce the possibility of measuring multiple crystallites. To record signal from low-intensity modes, momentum resolution was set to 0.75 nm^{-1} (BL35XU).

Calibration of the phonon energy was performed using silicon as a standard (BL35XU). For the measurements at the ESRF a deviation of 2% was considered, resulting in the best agreement of IXS and Raman measurements (see section 4.3).

The samples are synthesized crystals (HQ graphene, Netherlands). The MoS₂ crystal was directly grown with a thickness of about $150 \mu\text{m}$ to match the attenuation length of the used X-rays in MoS₂ to yield the best trade-off between high absorption and low scattering in a transmission setup. For WS₂ an approximately $20 \mu\text{m}$ thick platelet was peeled off the crystal. All measurements were taken at ambient conditions. Further details about the MoS₂ crystal are given in section 4.2.1.

4. Phonon dispersions of TMDCs

Parts of this chapter have been published in [108].

This chapter describes the experimental determination of the phonon dispersion of MoS₂ and WS₂. I will first introduce the dynamical structure factor, which in principle can be considered the probed observable for IXS, before describing details of the precharacterization of the MoS₂ sample. Finally, detailed discussions of the inelastic X-ray scattering measurements will be given. For WS₂ an extensive investigation of the out-of-plane dispersion is performed.

4.1. Simulation of IXS intensities

For the interpretation of acquired spectra of the IXS experiments, it is of value to consider the theoretically predicted spectra (scattering intensities) (e. g. for assignment of branches, etc.). The cross section σ of the scattered photons into a specific solid angle (Ω) that is collected by the detectors (dE) is directly dependent on the dynamical structure factor $S(\mathbf{Q}, \omega)$

$$\left(\frac{d^2\sigma}{d\Omega dE} \right) = \frac{k_2}{k_1} r_e^2 |\epsilon_1^* \cdot \epsilon_2|^2 S(\mathbf{Q}, \omega) \quad (4.1)$$

for a transition from an initial state (k_1, ϵ_1) to the final state (k_2, ϵ_2). $r_e = e^2/m_e c^2 \approx 2.8$ fm is the classical electron radius [109]. The factor k_2/k_1 is in the case of IXS experiments close to 1 (cf. section 2.3) and hence can be neglected in the

4. Phonon dispersions of TMDCs

following discussion. The second factor $r_e^2 |\epsilon_1^* \cdot \epsilon_2|^2$ is the Thomson scattering factor and corresponds to the elastically scattered photons. The direct dependence on the Thomson scattering factor allows the deduction that in the vicinity of strong Bragg reflections strong inelastically scattered peaks can be found. This leaves us with the dynamical structure factor carrying the information of the inelastic scattering on phonons, i.e. IXS is directly probing the dynamical structure factor, which calculates as [109, 110]:

$$S(\mathbf{q}, \omega)_{hkl} \propto \sum_j^{3N_{at}} \left| \sum_d \frac{f_d(\mathbf{H} + \mathbf{q})}{\sqrt{2M_d}} e^{-W_d(\mathbf{H} + \mathbf{q})} (\mathbf{H} + \mathbf{q}) \cdot \mathbf{e}_{\mathbf{q}jd} e^{i(\mathbf{H} + \mathbf{q}) \cdot \mathbf{x}_d} \right|^2 F_{\mathbf{q}j}(\omega). \quad (4.2)$$

Here N_{at} is the number of atoms in the unit cell, f_d is the form factor, \mathbf{H} is the reciprocal lattice vector corresponding to the Bragg peak with Miller indices $(h \ k \ l)$. M_d and x_d are the mass and position of basis atom d , while e^{2W_d} is its Debye-Waller factor. $\mathbf{e}_{\mathbf{q}jd}$ is the displacement of atom d due to phonon mode j and $F_{\mathbf{q}j}\omega$ is the phonon mode's spectral shape and temperature dependent intensity. Due to electron-phonon and phonon-phonon scattering $F_{\mathbf{q}j}(\omega)$ is best described by a damped harmonic oscillator model [110]:

$$F_{\mathbf{q}j}^{\text{DHO}}(\omega) = \frac{4\omega}{\pi(1 - e^{\hbar\omega/k_B T})} \frac{\gamma_{\mathbf{q}j}}{(\omega^2 - \Omega_{\mathbf{q}j}^2)^2 + 4\omega^2\gamma_{\mathbf{q}j}^2},$$

where $\Omega_{\mathbf{q}j}^2 = \omega_{\mathbf{q}}^2 + \gamma_{\mathbf{q}j}^2$ is the effective frequency of the phonon mode and $\omega_{\mathbf{q}j}$ and $\gamma_{\mathbf{q}j}$ the angular frequency and linewidth (half width at half maximum) of the phonon mode j at wavevector q .

The exponent of the Debye-Waller factor e^{2W_d} from equation 4.2 is calculated as [109]

$$W_d(\mathbf{H} + \mathbf{q}) = \frac{\hbar}{4M_d N_q} \sum_{\mathbf{q}} \sum_j^{3N_{at}} \frac{1}{\omega_{\mathbf{q}j}} |(\mathbf{H} + \mathbf{q}) \cdot \mathbf{e}_{\mathbf{q}jd}|^2 \coth\left(\frac{\hbar\omega_{\mathbf{q}j}}{2k_B T}\right), \quad (4.3)$$

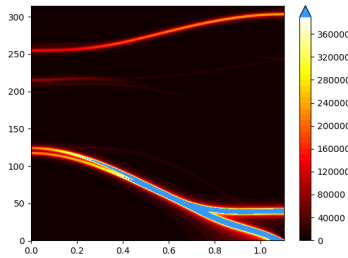


Figure 4.1.: Simulations of the dynamical structure factor for WSe_2 at the (0 0 11) Bragg peak exhibiting a strong $S(q, \omega)$ for the forbidden out-of-plane acoustic (ZA) branch.

which requires a sum over N_q vectors in the first Brillouin zone of the crystal. We found a negligible qualitative dependence of our results on W_d [108].¹

Since, the simulations only calculate the dynamical structure factor $S(q, \omega)$ and do not include the Thomson scattering factor, information about scaling due to the strength of the elastic scattering is neglected. Therefore, the calculations can suggest a strong signal, which however, is suppressed by a Thomson factor going to zero. This is illustrated in figure 4.1 for the out-of-plane transverse geometry at the (0 0 11) Bragg peak (WSe_2). The simulations exhibit a strong $S(q, \omega)$ for the acoustic branch which is not observable in the experiment (further discussion of the influence of the l -component on the inelastic scattering can be found in section 4.3). Yet, valuable information can be gathered evaluating the simulations. Figure 4.2 displays a set of simulations of the dynamical structure factor for WS_2 in the vicinity of the (-1 0 0) and (-1 2 0) Bragg peaks, showing (i) the different scattering intensities of the same branch at different Bragg peaks and (ii) the evolution of the scattering intensity with varying q .

¹The implementation of these calculations in a python script has been performed by Roland Gillen (Friedrich-Alexander Universität, Erlangen-Nürnberg). Further details about the underlying DFT calculations can be found in [108].

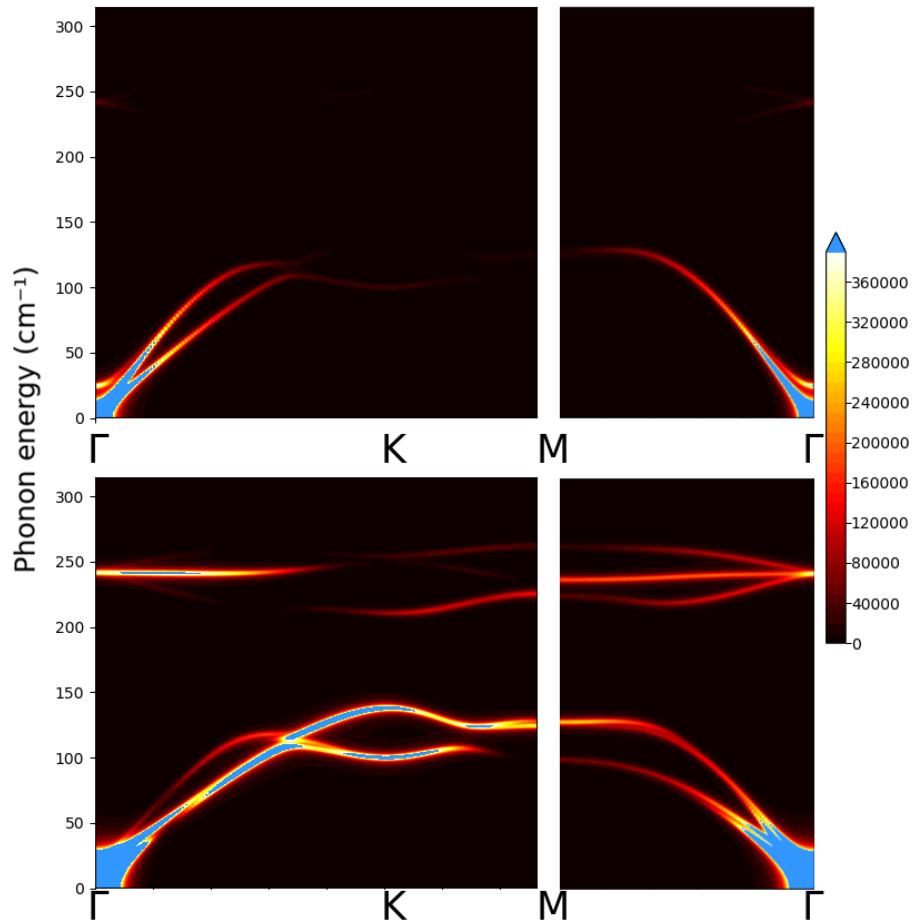


Figure 4.2.: Simulations of the dynamical structure factor for WSe_2 at the $(-1\ 0\ 0)$ and $(-1\ 2\ 0)$ Bragg reflections (upper and lower panels, resp.).

4.2. Phonon dispersion of MoS₂

4.2.1. Sample

The IXS measurements were performed on a commercially available synthetic MoS₂ crystal (HQ Graphene, Netherlands), which was grown to meet the specific thickness requirement of 150 μm . Figure 4.3 shows a photograph of the crystal mounted in the sample holder.

High resolution X-Ray diffraction (HRXRD) measurements were performed on a set of four samples provided by the manufacturer (hereafter called "sample 1", and accordingly) to evaluate which of the samples has the best crystal quality and to assess the orientation of the crystal's lattice vectors relative to the mount of the sample holder to facilitate the alignment process of the crystal at the beamline.²

To assess the orientation of the sample holder, a silicon (1 1 0) wafer was glued into the recessed slot (cf. drawing, Fig. A 1 in the appendix), which allows to align the (1 0 0) directions parallel to the edges of the holder. Subsequent measurement of the Bragg reflections of the silicon wafer and the MoS₂ crystal in a ϕ -scan allows to access the relative orientation. A ϕ scan of MoS₂ covering a full circle is shown in figure 4.4 a, i. e. a scan rotating the sample around the crystal surface normal (here, the crystal c-axis) at fixed ω , χ and θ angles. In this scan the sixfold rotational symmetry can be observed. The missing Bragg peak has probably been obscured by a clamp or the adapter used to mount the sample holder in the HRXRD setup. Figure 4.4 b presents high resolved ϕ scans of a single Bragg reflection of each silicon and MoS₂ (sample 3), allowing the deduction of the relative orientation of the crystals and hence the lattice orientation of MoS₂ with respect to the sample holder. Note that the increased linewidth of MoS₂ compared to silicon does not necessarily allow the conclusion of little crystal quality, as a) different Bragg reflections of the crystals were evaluated and b) natural line width varies for different crystals. Revisiting the photograph of sample 3 (Fig. 4.3) allows further interpretation of the

²The HRXRD measurements were supported by Johannes Enslin (Technische Universität Berlin).

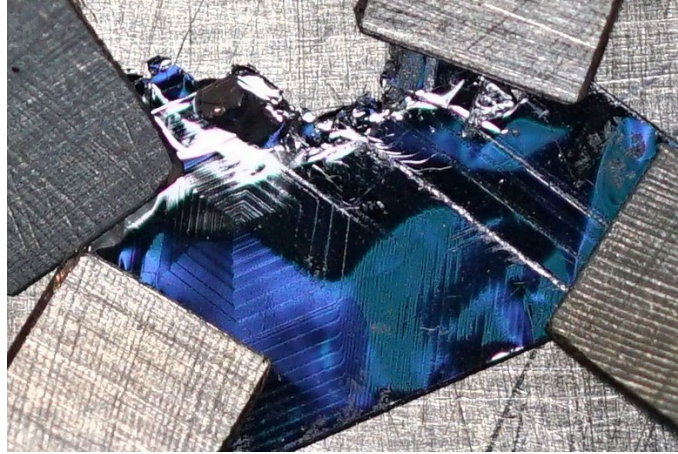


Figure 4.3.: Photograph of the MoS₂ crystal used for IXS measurements. The hexagonal pattern is due to steps in height on the surface. Note that the pattern has a uniform orientation at all locations on the crystal and are aligned to the lattice vectors. The width of the clamps, holding the crystal, have a width of 3 mm.

crystal quality. Closely examining the surface steps one observes a hexagonal pattern with uniform orientation on every position on the sample. Therefore, one can conclude that sufficient crystal quality with respect to rotation around the crystal *c*-axis is present to maintain a long-range order. The HRXRD measured orientation of the crystal is in excellent agreement with the orientation of the steps observed in the photograph.

A lower crystal symmetry might be present in terms of flatness of lattice planes across the crystal, as ω -scans show a broad peak with distinct maxima (see Fig. 4.4 c). This could also be due to the large cross-section of the ray of approximately $2 \times 10 \text{ mm}^2$, probing a large, probably bent area (cf. reflections on the surface in the photograph, Fig. 4.3). Furthermore, for thin samples, peaks are usually subject to broadening in ω scans [111]. Comparing the different MoS₂ samples, sample 3 shows the most pronounced maxima which can be attributed to large area single crystalline volumes with intact translation symmetry. In line with this speculation, the other MoS₂ samples would have a larger distribution of bends, breaking the translation symmetry. Note, offsets in the angle are due to mechanical variations in the setup of the adapter holding the sample holder. Figure 4.4 d and e depict 2θ and χ scans of the crystals, supporting the assessment of the best quality for sample 3, from the lowest full width at half maximum. Since sample 3 exhibits

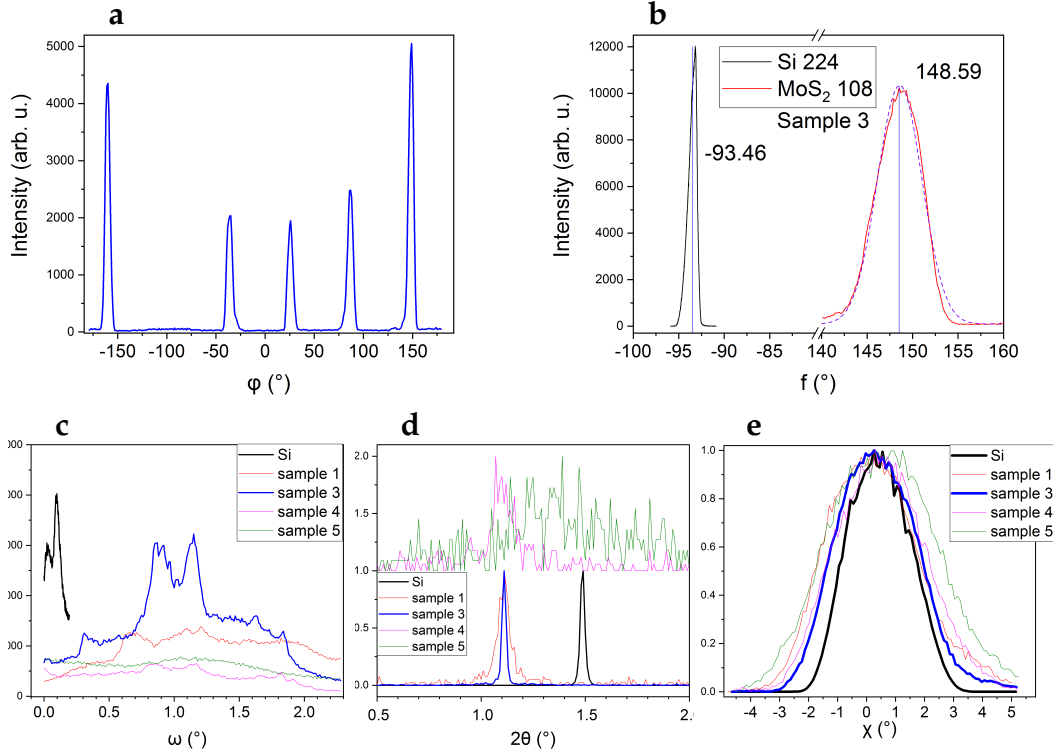


Figure 4.4.: HRXRD spectra of different MoS₂ crystals (samples 1, 3, 4, 5). **a** ϕ scan of MoS₂ exhibiting five of the six Bragg reflections emerging from the sixfold rotation symmetry. **b** comparison of high resolution XRD spectra of silicon and MoS₂ Bragg reflections, used for deducing the sample orientation. **c**, **d** and **e** depict ω , θ and χ scans used to assess the crystalline quality of the different samples.

the largest uniformity in the ω scan and the narrowest reflection lines in the 2θ and χ scans, we decided to use sample 3 for the IXS measurements, the other samples will not be subject of further discussion.

To further assess the crystal quality, Raman measurements were performed on the LabRAM setup with excitation wavelengths of 633 nm and 457 nm. An ultra-low frequency notch filter was used with the 633 nm laser to observe the shear mode (E_{2g}^1). Since the higher-frequency first-order modes are not easily deconvoluted from the resonance-induced strong higher-order background, an excitation of 457 nm was chosen for the determination of the high-energy optical Raman modes (E_{1g} , E_{2g}^2 and A_{1g}). Non-labeled peaks in Fig. 4.5 are assigned to higher-order Raman scattering processes. Due to the absence of the defect-enabled (first order) "LA" peak (A_1' or A_2' at K and B_{3u}/A_g at M) at around 230 cm^{-1} , see inset to Fig. 4.5 a good crystal

4. Phonon dispersions of TMDCs

quality can be confirmed [112, 113].

The acquired phonon energies will later be used to complement the measured IXS spectra at the Γ point (Fig. 4.7).

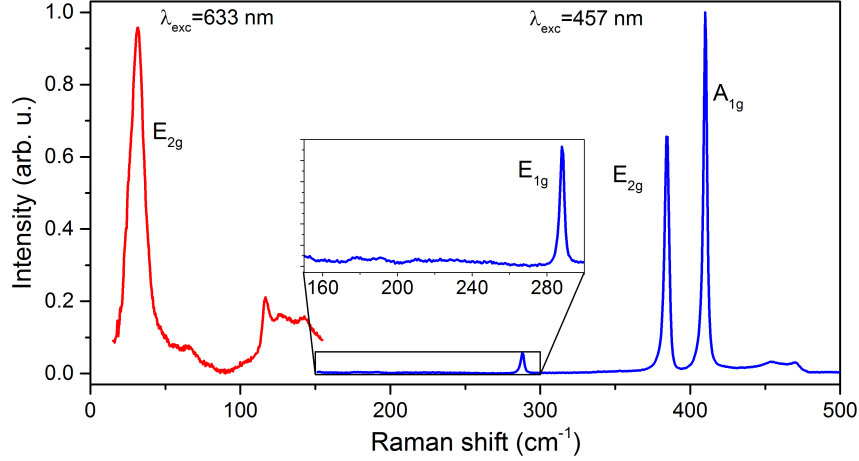


Figure 4.5.: Raman spectra of the MoS₂ crystal used for the IXS measurements. The red (blue) spectrum is acquired with 633 nm (457 nm) excitation wavelength.

4.2.2. IXS measurements

Sub-figure 4.6 a depicts a set of IXS spectra taken in the vicinity of the (0 0 12) Bragg peak, in the (0 q 0) direction. This scattering geometry preferentially detects the transverse out-of-plane component of the displacements and, hence, phonons with pronounced out-of-plane component. Each three spectra are taken simultaneously during one scan. The spectra are vertically offset by the absolute value of the phonon wave vector $|\mathbf{q}| = q = 0 \dots 0.5$ (i.e. Γ to M point) in units of the reciprocal lattice vector. For the spectra at $q = 0.1$ and $q = 0.5$ fits with Lorentzian functions³ are included (solid green and orange lines, resp.). The compilation of the obtained phonon energies is plotted over the corresponding phonon momentum in Fig. 4.6 b and represents the dispersion of the out-of-plane transverse modes from

³The correct model to approximate the peak shape is a damped harmonic oscillator, as discussed in section 4.1. However, the expected gain in accuracy is below the assumed error of the measurements. Furthermore, it is assumed that the convolution with the beamline characteristics results in a peak shape close to a Lorentzian function []

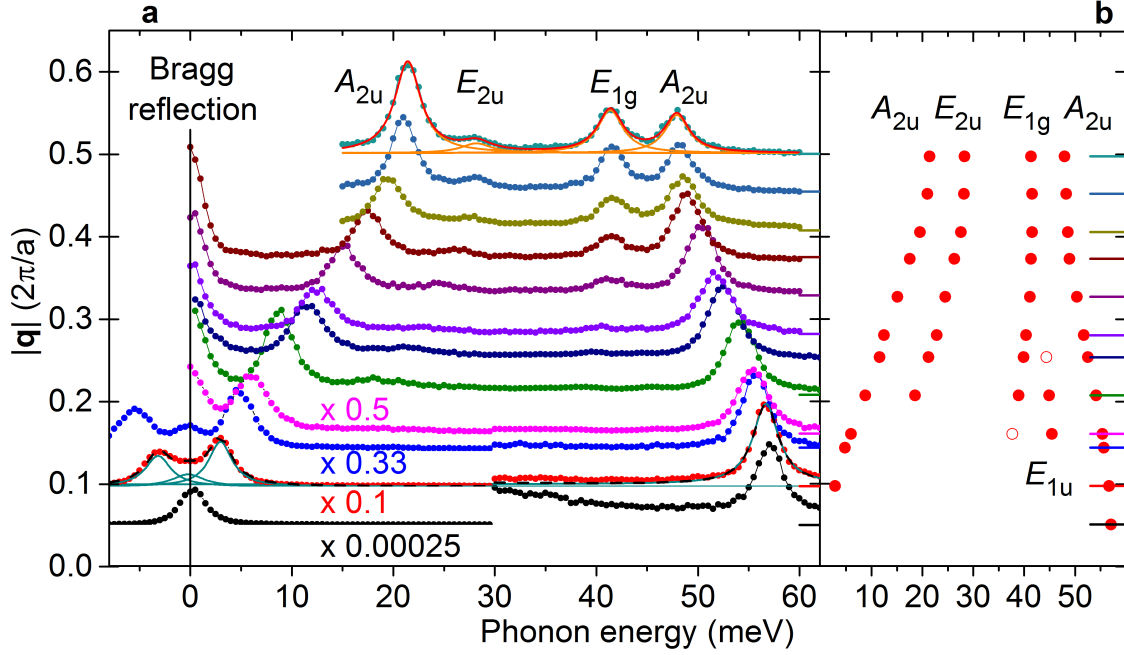


Figure 4.6.: **a** Experimental IXS spectra of MoS₂ along the Γ -M direction (in the vicinity of the (0 0 12) Bragg reflection) with vertical offsets corresponding to the phonon q vector. The four spectra closest to Γ are scaled by the factor given next to the spectrum. **b** Extracted peak positions of the spectra shown in **a**. Peaks are labeled according to their symmetry and notation at the Γ point. This figure has been published in Ref. [108].

Γ to M. For simplicity, the irreducible representation at the Γ point is used to label the entire phonon branch.

The full set of IXS spectra yields all acoustic and almost all optical phonon branches along the A - Γ - K - M - Γ directions as shown in figure. 4.7. The values from the IXS measurement (circles) are complemented at the Γ point by values obtained by Raman spectroscopy (stars), cf. figure 4.5. The observations from these two techniques are in seamless agreement. Furthermore, theoretical values, obtained by density functional perturbation theoretical calculations with included van-der-Waals corrections, are included (lines).⁴ The calculations show that the Davydov pairs are only split by a small amount, as expected for van-der-Waals bound, layered materials, due to the weak inter-layer forces. The splitting, however, is too small to measure both phonons of a Davydov pair, if they are not selectively allowed at

⁴DFT calculations have been performed by Roland Gillen (Friedrich-Alexander Universität, Erlangen-Nürnberg). Details about the DFT calculations are given in Ref. [108]

4. Phonon dispersions of TMDCs

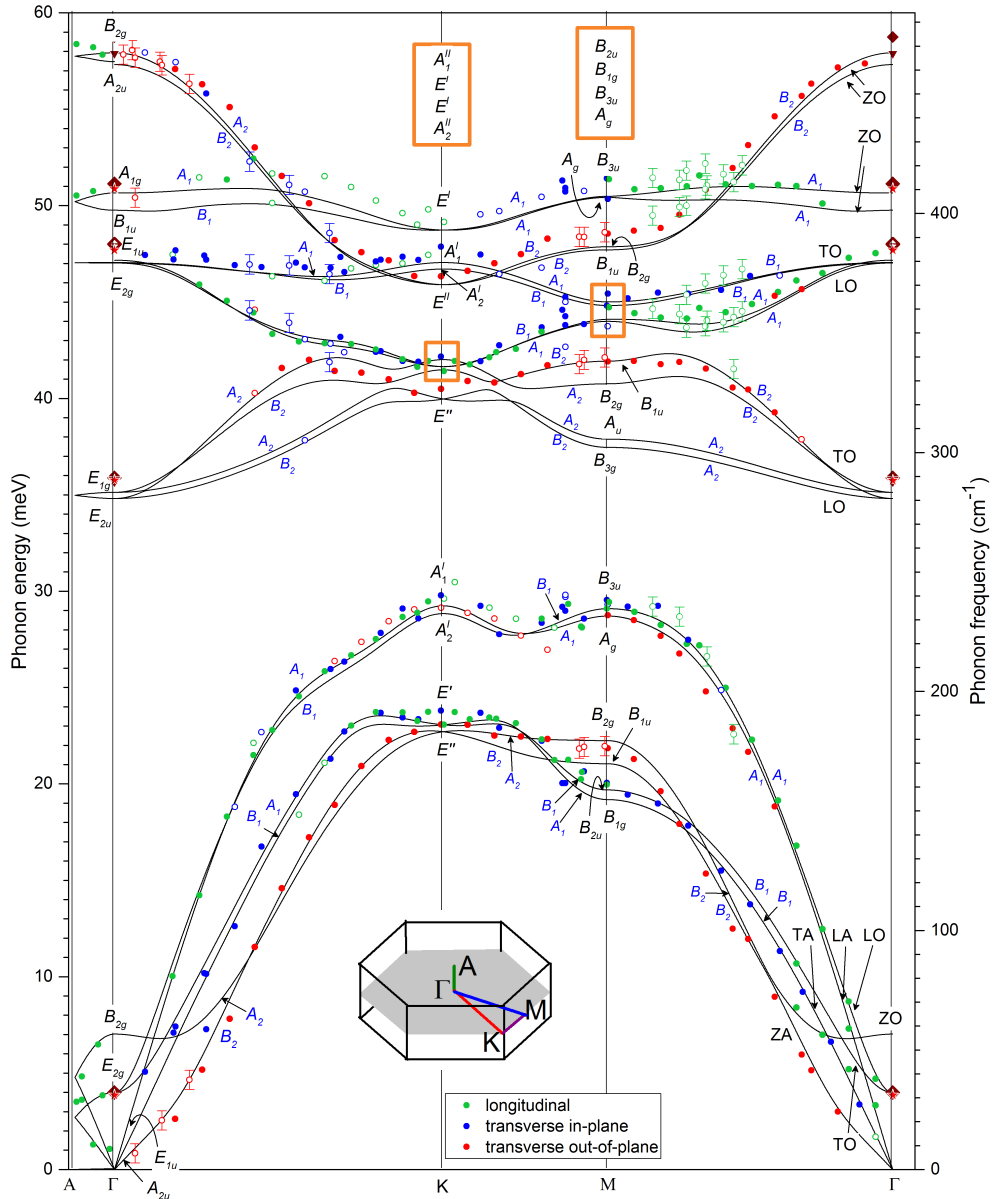


Figure 4.7.: Inelastic X-ray scattering measurements and density-functional perturbation theory calculations of the phonon dispersion of MoS₂ along the high symmetry directions A- Γ -K-M- Γ . For symbols without an error bar, the error is estimated to be smaller than the symbol size. Open symbols depict peaks with small intensities or larger error. Values at the Γ point are Raman and IR spectroscopy data from the literature [60, 76, 114] (diamonds) and from Raman measurements on the same sample as used in the IXS experiment (stars). Phonon branches are labeled by irreducible representations of all branches at the Γ (D_{6h}), K (D_{3h}) and M (D_{2h}) points (black) and along the high-symmetry lines (C_{2v} , blue), as well as by their displacement (L, T, Z) and acoustic (A) or optical (O) character. This figure has been published in Ref. [108].

different Bragg peaks, caused by a vanishing dynamical structure factor S for one branch.

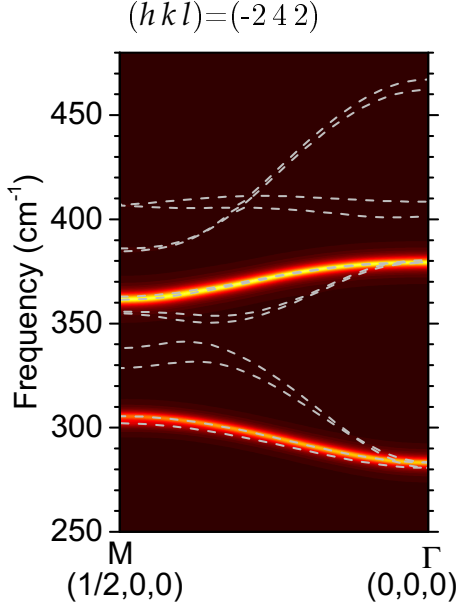


Figure 4.8.: Simulated dynamical structure factor illustrating the possible observation of the branches associated to the longitudinal E_{1g}/E_{2u} modes at the $(-2\ 4\ 2)$ Bragg peak. This figure has been published in Ref. [108].

In the experiment, eight branches can be observed throughout the entire Brillouin zone. For the branch consisting of the almost degenerate longitudinal E_{2u}^{Γ} and E_{1g}^{Γ} branches, only a weak peak, approximately in the middle between Γ and K points, and a few peaks in the vicinity of the K point could be observed. Considering the calculated dynamical structure factors around the Bragg peaks, at which the measurements were performed, one can observe that no scattering is expected for these branches, see figure 4.9. The simulations suggest that destructive interference of the counter-phase oscillation of the sulfur sublayers in each MoS₂ layer causes extinction of the structure factor for all q -vectors along the Γ - M and Γ - K - M directions, if a Bragg peak $(hk0)$ is used (cf. tables A I, A II and A III in the appendix).

Therefore, measurements at Bragg peaks with a finite out-of-plane component $l \neq 0$ should lead to activation of the longitudinal E_{1g} and E_{2u} branches, caused by symmetry breaking of the phase factors from the atomic positions, which lifts the destructive interference.

The calculation of the dynamical structure factor at $(-2\ 4\ 2)$ in the direction of $(q\ 0\ 0)$ are shown in figure 4.8 and predict finite scattering intensity for the $E_{1g}(\text{LO})$ branch.⁵

For some branches, the intensity of the IXS signal fades towards the Γ point. This is true for example for the branch with $E_{1g}(\text{TO})$ symmetry at Γ . This branch

⁵These calculations were made after the experiment to explain the scattering behavior and were therefore not available as a guidance when selecting the scattering setup or during the experiment.

4. Phonon dispersions of TMDCs

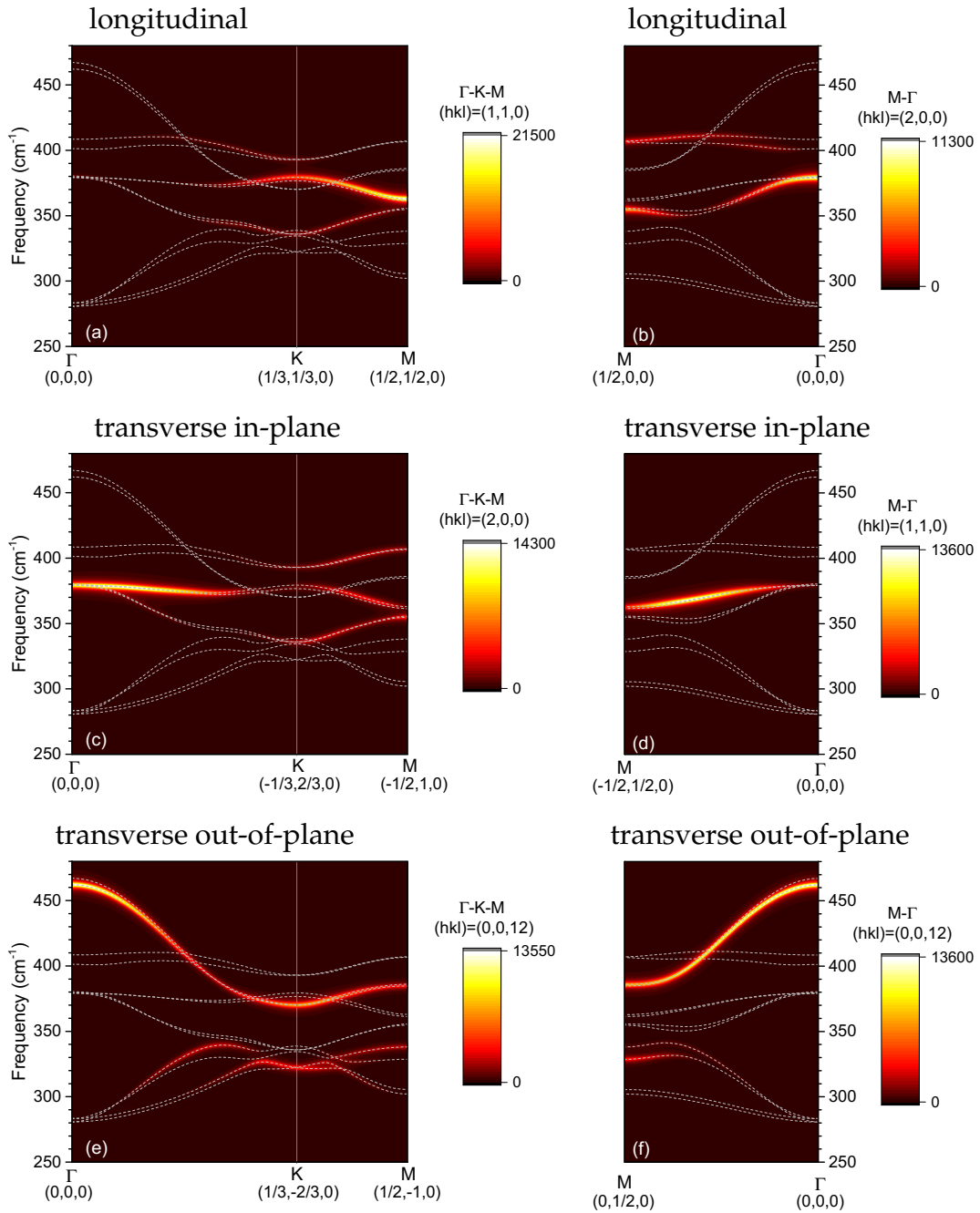


Figure 4.9.: Dynamical structure factor calculations for the Bragg peaks used for the IXS measurements of MoS₂. Lines depict DTF calculated phonon branches as a guide to the eye. This figure has been published in Ref. [108].

is invisible around the Γ point in the experiment, becomes visible with a weak signal at first around a third of the distance from Γ to M , to yield strong signal further towards the M point. This can be explained considering the displacement directions of atoms participating in the oscillation of the respective phonons. At the Γ point these are either longitudinal (L), transverse in-plane (T) or transverse out-of-plane (Z). This is seen by the color of the symbols representing the IXS data, which indicates the displacement direction preferentially detected in the given scattering geometry. While progressing through the Brillouin zone the phonon eigenvectors change and hence the displacement patterns. As a result phonons have no pure longitudinal or transverse oscillation. For the Γ , K and M points displacement patterns can be found in tables A I, A II and A III in the appendix.

In the case of the E_{1g}^{Γ} branch, the displacement at Γ is of pure in-plane transverse nature. Therefore, no coupling to the photons in the out-of-plane scattering geometry exists. However, with phonon momenta $q > 0$ the phonons gain an out-of-plane component allowing the coupling to the out-of-plane scattering geometry, resulting in (weak) IXS signal. This consideration is supported by the transition of the eigenvectors derived from the DFT calculations, which is depicted in figure 4.10. Further, this mixing can be deduced from the observation of one branch in different scattering geometries, see for example the longitudinal acoustic (LA) branch, which can be observed in all three geometries in the vicinity of the M point. The corresponding eigenvectors of the B_{3u} (E_{2g}^{Γ}) and A_g (E_{1u}^{Γ}) modes comprise both, an in-plane and out-of-plane nature (see table A III in the appendix).

A comparable activation and deactivation of the scattering of branches can be observed in the case of the transverse E_{2u}^{Γ} and the longitudinal E_{1g}^{Γ} . Following the data points around 40 meV in the transverse out-of-plane scattering geometry (red circles) one might conclude that the calculated dispersion cannot reproduce a crossing of branches, which results in the impression of a false ordering of branches at the K point. Consulting the dynamical structure factor simulations, one can find that the transverse E_{2u}^{Γ} grows in scattering strength around half the distance to the BZ edge and again vanishes towards the K point. The longitudinal E_{1g}^{Γ} on the other hand gains in scattering strength around the momentum, where the E_{2u}^{Γ} fades. At the K point the displacement patterns are of pure in-plane character in the case of the

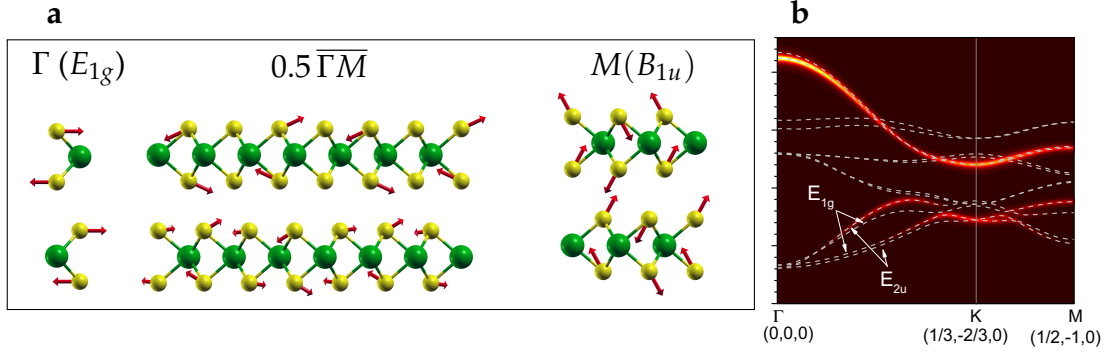


Figure 4.10.: **a** Transition of the phonon eigenvectors from the Γ to the M point of the branch with E_{1g} (TO) symmetry at the Γ point. See tables A I, A II and A III in the appendix for a complete overview of the phonon eigenvectors at the Γ , K and M points. **b** Simulation used for the assignment of the measured out-of-plane phonon energies at the (0012) Bragg peak, showing the emergence of the dynamical structure factor for the longitudinal $E_{1g}^\Gamma/E_{2u}^\Gamma$ branches around K . Sub-figure **b** has been published in [108].

$A_1'' (E_{2u}^\Gamma)$ and pure out-of-plane character for the $E'' (E_{1g}^\Gamma)$, see table A II. The same shift in activation of the branches can be observed in between the K and M points, which is in perfect agreement with the experimental observations. This allows the correct assignment of the branches and confirms the correct ordering of branches in the DFT calculations. Again, the activation and deactivation is originated by a change in the displacement patterns and the resulting momentum-selective coupling to the photons in the given scattering geometry. This is not limited to branches of different Davydov pairs, but can also be found for two branches of the same Davydov pair: The A_{1g}^Γ and B_{1u}^Γ as well as the E_{1g}^Γ and E_{2u}^Γ branches exhibit a shift in activity in the $\Gamma - M$ direction. For the A_{1g}^Γ and B_{1u}^Γ Davydov pair a decrease of energy was observed for the measurement most close to the Γ point. And in the case of the E_{1g}^Γ and E_{2u}^Γ branches, it seems that the measurements are not in agreement with the calculations. In both cases an activation and deactivation of respective branches can be observed in the simulations of the dynamical structure factor (Fig. 4.9 **b** and **f**).

Examining the shapes of the acoustic branches one observes a distinct difference in between the LA/TA and the ZA branches. While the LA and TA branches exhibit a linear dispersion, the ZA branch follows quadratic shape. This is signature of two dimensional, atomically flat materials [115] and underlines the 2D nature of MoS₂

even in its bulk form. An implication of this is that little changes are to be expected on most parts of the phonon dispersion, changing the layer number, due to weak inter-layer interactions for all but the rigid layer modes (E_{2g} and B_{2g}). This is also in line with the observations in the related materials of graphite and graphene [116–119]. Therefore, one can expect this being an intrinsic property of van-der-Waals bound materials.

In table 4.1, values from the IXS and Raman measurements are shown for the Γ , K and M points. Further, phonon energies by DFT calculations are given as a comparison. The values are accompanied by the irreducible representations for the respective high symmetry point and phonon. Furthermore, lines include information of the correlation of phonons by connecting phonons of the same branch, e. g. B_{2g} at Γ belongs to the same branch as the phonon with E'' symmetry at K and B_{2g} symmetry at M , as indicated by the red line.

Γ (space group D_{6h}^4)				K (D_{3h}^4)			M (D_{2h}^{17})			Γ	
irr. rep.	Raman	IR	DFT	irr. rep.	IXS	DFT	irr. rep.	IXS	DFT	irr. rep.	
E_{1u}	TA			E''	186	183.1	B_{1g}	161	154.7	TA	
	LA	n.a.	0.0				B_{2u}	158.7		E_{1u}	
A_{2u}	ZA			E'	189	186.0	B_{1u}	176	169.7	LA	
	TO						B_{2g}	179.4		ZA	
E_{2g}	LO	31 – 32 ^a [114]	32.2	A'_2	239	232.5	A'_g	235	231.5	TO	
	ZO		56.6	A'_1	235.8		B_{3u}	234.6		LO	
B_{2g}	ZO									ZO	
E_{2u}	LO	n.a.	280.7	E''	327	322.3	B_{3g}	302.1	305.5	LO	
	TO						A_u	305.5		TO	
E_{1g}	LO	286 – 289 ^b [76, 114]	283.3	A''_2	334	334.5	B_{2g}	328.7		LO	
	TO			E'	334	335.9	B_{1u}	338	338.1	TO	
E_{2g}	LO	383 – 384 ^b [76, 114]	379.2	A''_1	340	339.0	A'_g	353	354.8	LO	
	TO						B_{3u}	355.6		TO	
E_{1u}	LO		379.4	E''	373	370.1	B_{1g}	361	361.4	LO	
	TO	n.a.	380.4				B_{2u}	364	362.9	TO	
B_{1u}	ZO		401.3	A'_2	384	376.7	B_{1u}	392	384.7	ZO	
A_{1g}	ZO	408 – 410 ^b [76, 114]	408.5	A'_1	379.4		B_{2g}	386.0		ZO	
A_{2u}	ZO		462.2	E'	398	393.0	A'_g	410	406.6	ZO	
B_{2g}	ZO	n.a.	467.1				B_{3u}	407.1		ZO	

Table 4.1.: Phonon frequencies (given in cm^{-1}) of MoS_2 at the Γ , K and M high-symmetry points from the DFT calculations and experiments (Raman and IR spectroscopy at Γ and IXS at K , M). n.a. identifies not active phonon modes in Raman and IR experiments. The phonon modes are labeled by their irreducible representations in the factor groups D_{6h} (Γ), D_{3h} (K) and D_{2h} (M). Lines connect phonons that belong to the same phonon branch. This table has been published in Ref. [108].

^a measured with 633 nm excitation
^b measured with 457 nm excitation

4.2.3. Comparison of the phonon dispersion obtained by IXS with data from the literature

Despite the importance of the phonon dispersion for the evaluation of mechanical and elastic properties, thermal transport as well as charge-carrier dynamics, phonon-assisted optical excitations and many more, only few experimental values are known for any TMDC. For MoS₂, only two measurements of parts of the dispersion have been reported in the literature, to the best of my knowledge.

Figure 4.11 **a** shows the comparison of the dispersion obtained by IXS with the previously reported measurements by electron energy loss spectroscopy (EELS, open circles) [120]. The acoustic branches from the EELS measurements deviate significantly from the data obtained by IXS as well as the calculations. As EELS is a surface sensitive technique, one might think that the difference is due to surface defects or reconstruction. However, in a layered material such a large difference between layers near the surface and layers within the bulk seems rather unlikely. The slope of the acoustic branches differs approximately by a factor of two between the EELS and IXS data, suggesting a missing factor in the calculations of the momenta or energies for one of the datasets.

The inelastic neutron scattering data (INS, Fig. 4.11 **b**, open squares) [32], on the other hand, are in excellent agreement with the IXS data for the acoustic branches. A good agreement can be found for the optical branches in the vicinity of the Γ point, however, energies and assignment of some branches deviate close to the M point. An anti-crossing [label (a)] and a crossing of branches [label (b)] in the INS measurements, can be ruled out by analysis of the selection rules in IXS measurements.

4. Phonon dispersions of TMDCs

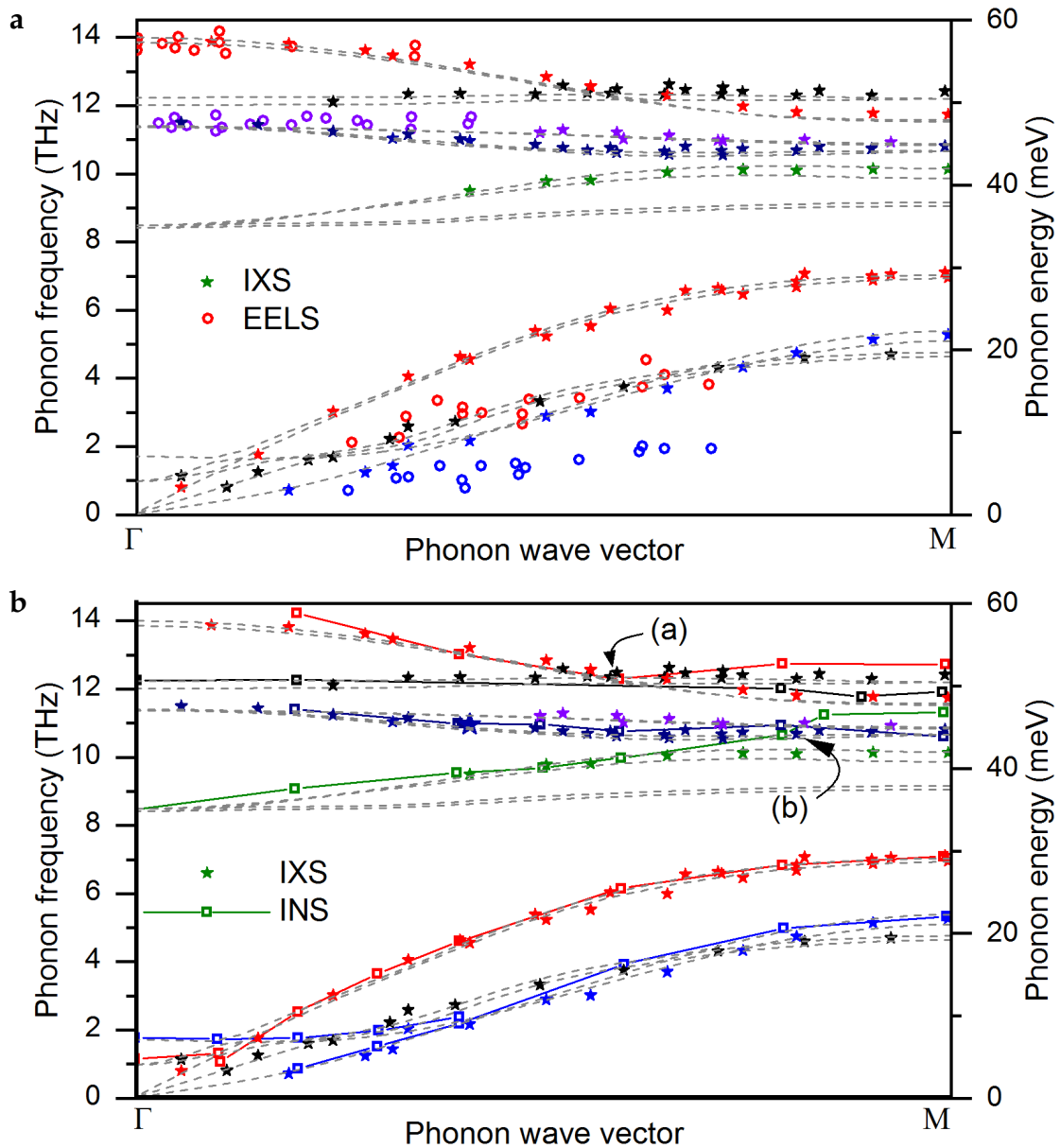


Figure 4.11.: Comparison of the IXS data (stars) with EELS measurements of Ref. [120] (open circles, a) and INS measurements of Ref. [32] (open squares, connected by lines, b). Colors depict different branches. Dashed gray lines depict DFT calculations as a guidance to distinguish different branches. A different version of this figure has been published in Ref. [108].

4.3. IXS of WS₂

Further inelastic X-ray scattering measurements have been performed on WS₂ at the European Synchrotron Radiation Facility (ESRF) in Grenoble, France. The measurements were aimed to further substantiate the previous measurements on MoS₂, by measuring (i) the dispersion of a second TMDC and (ii) measuring the previously unobserved $E_{2u}^{\Gamma} / E_{1g}^{\Gamma}$ (LO) Davydov pair. The measurements were performed not only along the in-plane high symmetry directions, but cover a large volume of the irreducible reciprocal space, allowing more advanced deductions from the phonon dispersion, such as the phonon density of states, which will not be covered in this thesis.

A photograph of the sample in the gonio head is shown in Figure 4.12. To acquire a sample of about 20 μm in thickness (absorption length of ≈ 20 keV X-rays in WS₂), a thin sheet was peeled off a single crystal. This crystal was then glued to a polymer cone on its edge.⁶

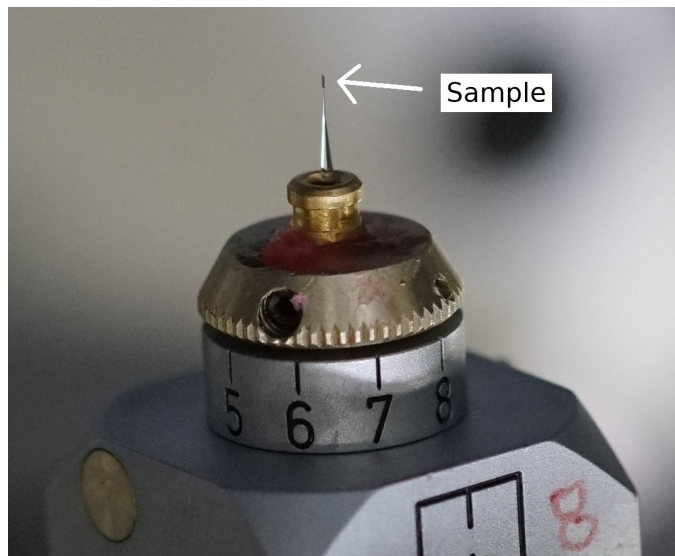


Figure 4.12.: Photograph of the WS₂ crystal in the sample mount. The sample is the dark flake atop the polymer cone in the gonio head.

⁶The sample fabrication was performed by Alexei Bossak (European Synchrotron Radiation Facility).

4. Phonon dispersions of TMDCs

IXS measurements at the beamline ID28 (ESRF) were performed at the same conditions and in the same manner as at BL35XU (SPring-8), except for the use of KB mirrors, to achieve a small spot size of $20 \times 20 \mu\text{m}^2$.

Due to the construction of the beamline, with 9 detectors in a line (in momentum space), and due to the chosen scattering geometries, a large portion of the acquired data is not within the basal plane BZ. To classify and sort the data a custom python script was used.⁷ This script uses the original data to find the corresponding coordinates in the irreducible prism of the first BZ (spanned by the $\Gamma - K - M - L - H - A$ high symmetry points) and evaluates and refines the data set according to the deviation in the Miller index l as well as the estimated error made by projecting a measurement point $(h k l)$ onto the basal plane high-symmetry directions.⁸

Figure 4.13 depicts the projections onto the basal plane of the measurements' reciprocal space points. Sub-figures 4.13 **a** and **b** depict the original $(h k l)$, while **c** and **d** depict the zone-folded $(h' k' l')$ in the irreducible part of the first BZ. Only considering measurements in the basal plane, i. e. with $|l| \leq 0.025$ (5% of the length $\overline{\Gamma A}$), one obtains the subset shown in 4.13 **e** and **f**.

To further refine the data, the calculated error from in-plane projection onto the high-symmetry lines is used. Figure 4.14 depicts the estimated error upon projection for all measured points (for the example of the $A_{2u}^{1,\Gamma}$ phonons; a compilation of the projection errors of all branches can be found in the appendix, section A 3.3.7, page XXXVI). Points depicted in color exhibit a different energy of $|\Delta E| \leq 0.1 \text{ cm}^{-1} \approx 1.2 \mu\text{eV}$ compared to the high-symmetry direction, while gray points have a larger deviation. Points meeting both the requirement of little deviation in the out-of-plane momentum and in-plane energy are considered for further analysis, i. e. the intersecting set of the sets depicted in 4.13 **e** / **f** and 4.14 (for the $A_{2u}^{1,\Gamma}$ branch).

To acquire spectra from the measurement file (SPEC / FOURC file from the

⁷The script and a detailed description of it can be found in the appendix, section A 3 on page XVII.

⁸Note, the script only considers the error from in-plane projection, which is reasonable due to the low out-of-plane dispersion of most phonons in the BZ (further discussion below). Second, the error is estimated by evaluating the DFT calculated dispersion.

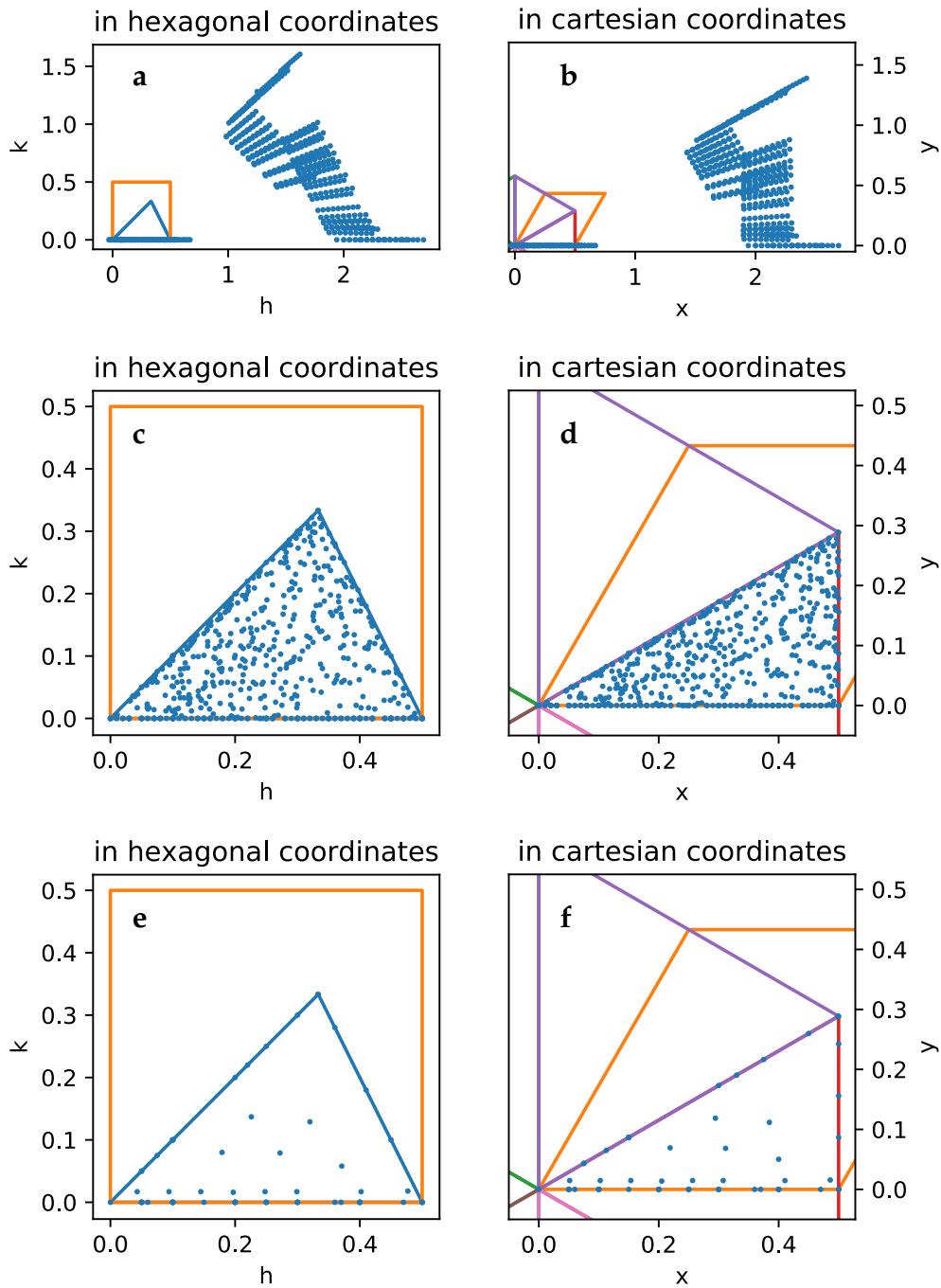


Figure 4.13.: Depiction of the basal plane projection of the measurements' reciprocal space points ($h k l$) (a, b), their corresponding ($h' k' l'$) in the irreducible triangle in the first BZ (c, d) and the subset of the data with $|l| \leq 0.025$ (e, f). Sub-figures a, c and e (b, d and f) depict the data in hexagonal (cartesian) coordinates. Details of the script are found in sections A 3.2 and A 3.3.1 in the appendix.

4. Phonon dispersions of TMDCs

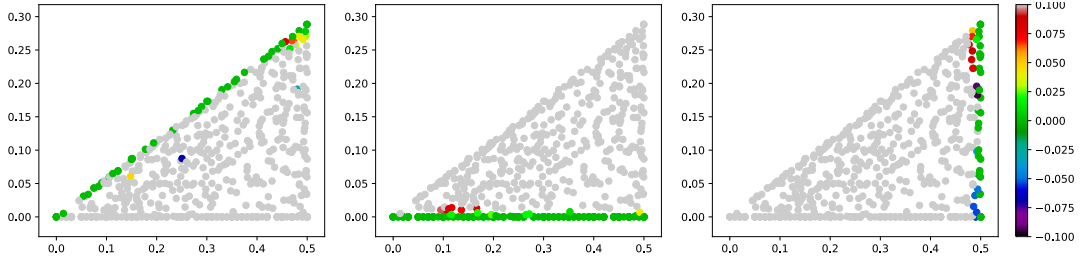


Figure 4.14.: Heatmaps depicting the error upon projection of measured $(h k l)$ onto the $\Gamma - K$, $\Gamma - M$ and $K - M$ high symmetry directions for the $A_{2u}^{1\Gamma}$ phonons (left, middle and right panel, resp.). Corresponding heatmaps for all phonons can be found in section A 3.3.7 in the appendix.

beamline), which contains all measured data (including motor positions and such) a further part of the python script has been written. The script splits the main file into individual scans, exploiting the structure of the file through regular expressions. The split scans are then offset- and X-ray flux-corrected, as well as interpolated, when multiple scans are present for the same reciprocal space point.

Figure 4.15 depicts spectra of a scan in a mixed transverse in-plane and out-of-plane scattering geometry at $(h k l)=(1+q 1+q 6)$. The spectrum depicted in blue is acquired at $(1.1 1.1 6)$ and is therefore on the $\Gamma - K$ line, while the other spectra exhibit a significant deviation in l , and are disregarded. The phonon ener-

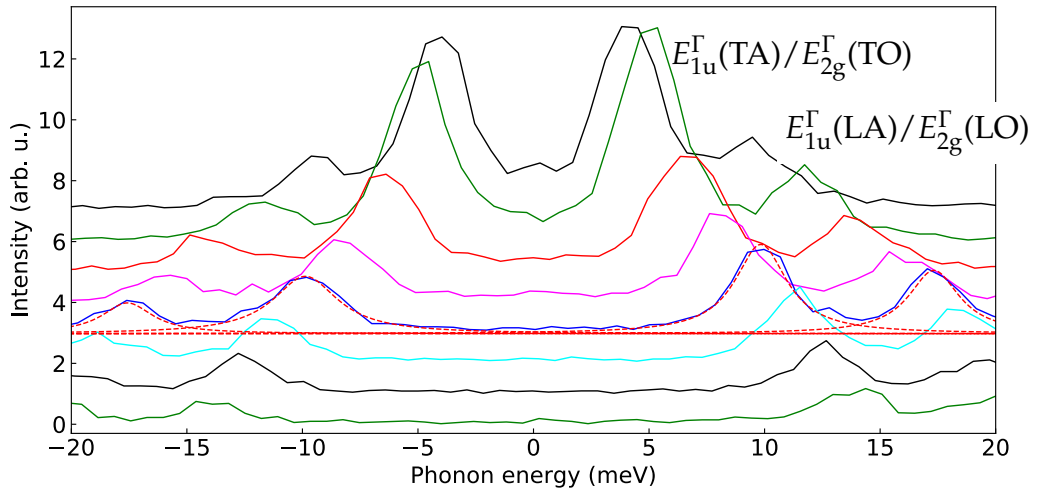


Figure 4.15.: IXS spectra of WS_2 . Each spectrum depicts the signal on one detector during one scan. The spectra are offset for better visibility.

gies are extracted by fitting the peaks with a Lorentzian model, as for the spectra of MoS_2 (cf. section 4.2.2). Plotting the phonon energies over the phonon momentum along the high symmetry directions $\Gamma - K - M$ and $M - \Gamma$, results in the phonon dispersion relation depicted in figure 4.16. Note that the categorization into longitudinal, transverse in-plane and transverse out-of-plane is for most cases approximative, as most scans are in a mixed scattering geometry. For example, the above considered measurements at $(1+q, 1+q, 6)$ possess a comparable in-plane and out-of-plane momentum, yet their data points are depicted as longitudinal (green). The lines depict DFT-D3 calculations.⁹ Overall an excellent agreement of the IXS measurements with the DFT calculations can be observed. Yet, not all branches are observed, since the large portion of the measured data is not considered in the above analysis, because of its out-of-plane component.

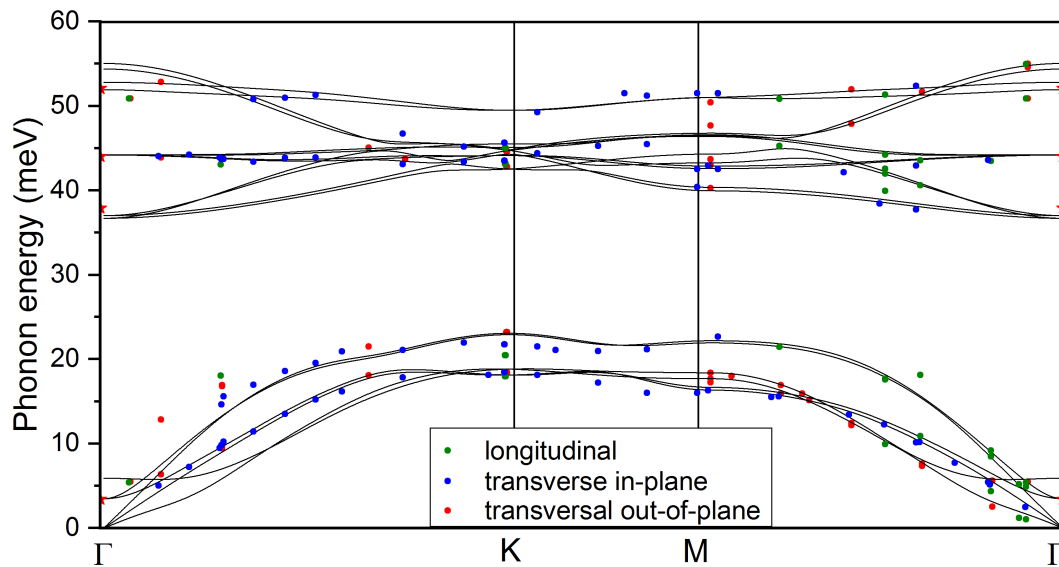


Figure 4.16.: Phonon dispersion of WS_2 . Circles depict IXS measurements in longitudinal (green), transverse in-plane (blue) and transversal out-of-plane scattering geometry. Mixed scattering geometries have been labeled by the predominant contribution (see text for details). Stars at the Γ point depict Raman measurements from [77, 121–124].

⁹The calculations were scaled by a factor of 1.02 to fit the Raman measured data at the Γ point [77, 121–124].

4. Phonon dispersions of TMDCs

To substantiate the measured phonon dispersion, I will evaluate the influence of a deviation in l on the in-plane dispersion. This is expected to be low, due to (i) the layered structure of WS₂ and (ii) the observation of virtually no dispersion for the optical phonons in the measurements on MoS₂ in $\Gamma - A$ direction. In this case a relaxation of the constraints of data selection would allow to obtain a larger data set.

Figure 4.17 depicts the out-of-plane dispersions of the A_{2u}^1 (ZA), E_{1u} (LA), E_{2u} (LO) and B_{2g}^2 (ZO) phonons of WS₂ in the reciprocal space spanned by the $\Gamma - A - K - H$ and $K - H - M - L$ high symmetry points. Color changes in the contour plots depict a difference of 1 meV. Dispersion profiles parallel to $(0\ 0\ l)$ are shown for exemplary points along $[h\ h\ 0]$ (i.e. with $k = h$) in the respective right panel. For the acoustic phonons a strong dispersion of a few meV is observed in case of low h , i.e. low in-plane phonon momenta. For larger momenta, the dispersion becomes small. This is clearly seen in the dispersion profiles, where the profiles starting at low energies (hence with small phonon momentum for the acoustic branches) exhibit a strong variation in energy, while profiles with an energy of $\hbar\omega_p \gtrsim 7\text{ meV}$ at $l = 0$ are virtually vertical in the plot. The optical branches exhibit negligible dispersion in the out-of-plane direction, independent of phonon momentum or energy.

For the low energy optical branches the relative high dispersion lies within the nature of the displacement pattern of the respective motions. These phonons are (at Γ) rigid-layer modes: The shear or breathing-like motions (E_{2g} and B_{2g} , resp.). These rigid-layer modes are fully determined by the inter-layer forces implying a dispersion in the corresponding direction. The non- Γ phonons of all (quasi-) acoustic branches (A_{2u}^Γ , E_{1u}^Γ , E_{2g}^Γ and B_{2g}^Γ) carry this dependence into the BZ. The dependence is retained close to the Γ point ($h \approx 0$) for all values of l , however fades quickly in in-plane direction. At larger h covalent intra-layer bonds become the driving force of the phononic atom-displacement, while the contribution from van-der-Waals forces becomes negligible. This behavior underlines the 2D-nature of this van-der-Waals layered material, where neighboring layers have only little interaction, even in its bulk form.

This insight allows to consider more of the acquired data. The calculations pre-

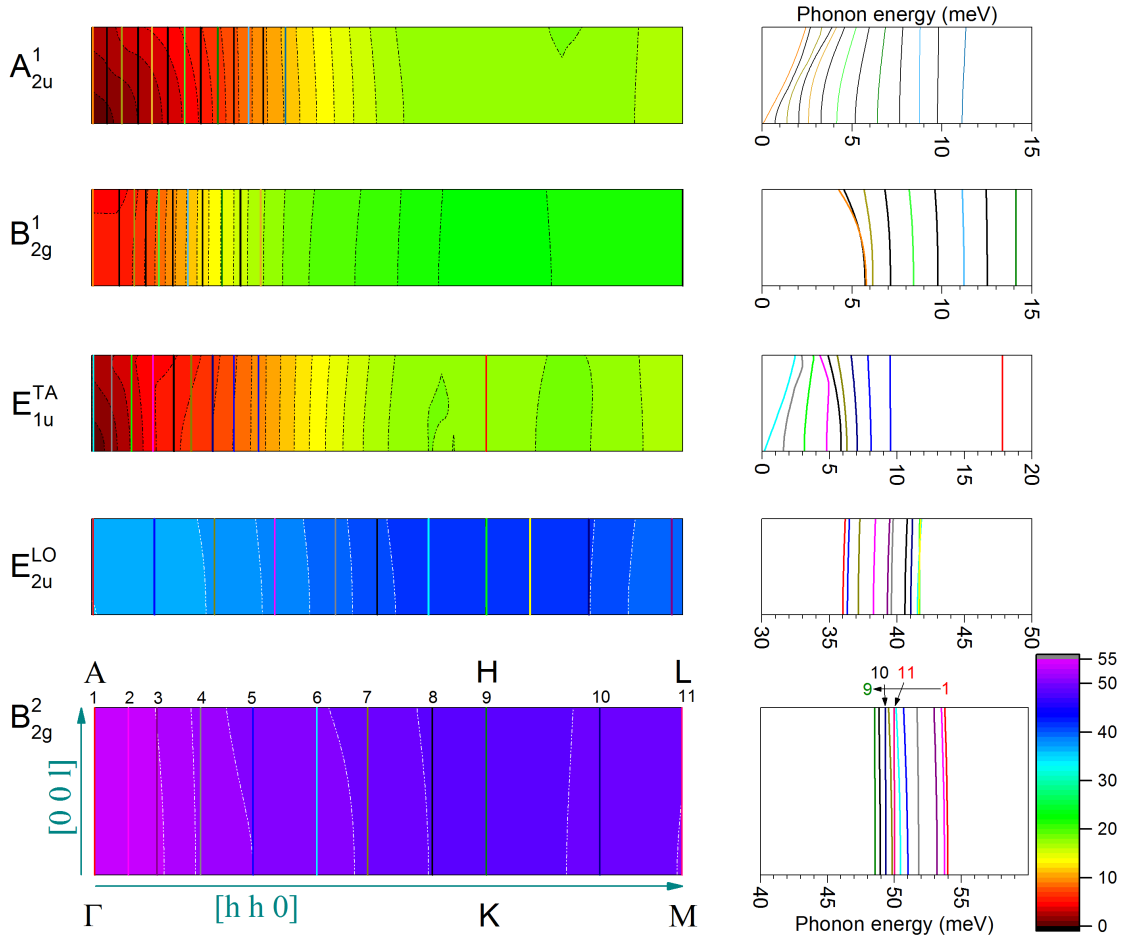


Figure 4.17.: Left panels: 2D-Dispersion of the A_{2u}^1 (ZA), B_{2g}^1 (breathing, ZO), E_{1u} (TA), E_{2u} (LO) and B_{2g}^2 (ZO) phonons of WS_2 . The depicted area corresponds to the reciprocal space spanned by the $\Gamma - K - M$ and $A - H - L$ high symmetry directions. The phonon energies are color coded, according to the displayed scale. Dotted contour lines indicate an energy difference of 1 meV. Right panels: 1D-dispersions parallel to the Γ -A direction for distinct q points along the $\Gamma - K - M$ direction in the basal plane (indicated as lines in the left panel).

dict for the optical branches that all values can be used, as the dispersion can be considered smaller than the experimental uncertainty for all in-plane momenta.

Figure 4.18 depicts the dispersion constructed by 1617 data points, originating from scattering events with arbitrary Miller index l along the in-plane high-symmetry directions. Measurements with a Miller index $l = 0$, depicted in figure 4.16 (above), are included as black squares. For the acoustic branches most

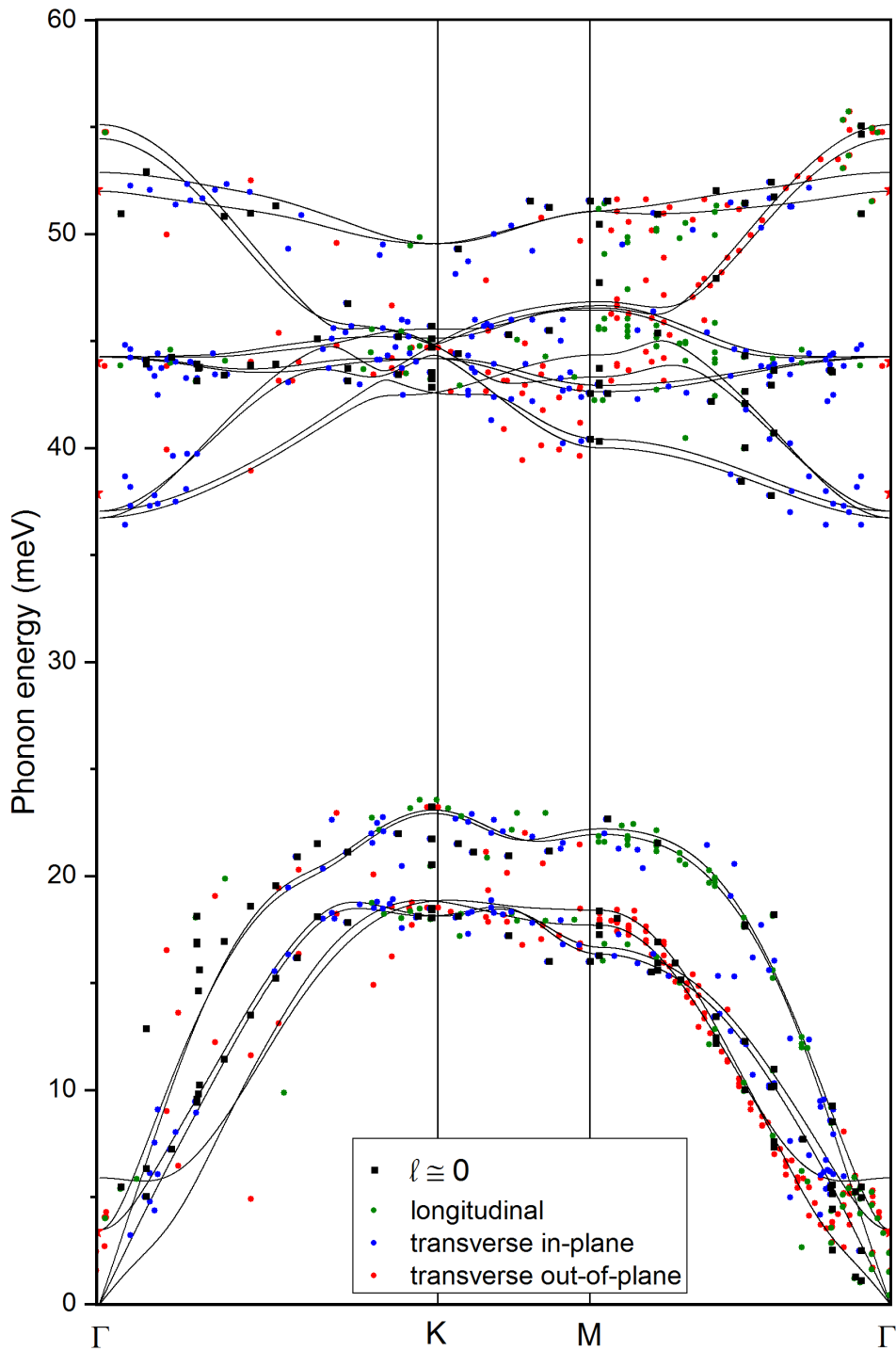


Figure 4.18.: Phonon dispersion of WS_2 considering scattering events along the in-plane high-symmetry lines regardless of their out-of-plane component. Squares depict data already shown in Fig. 4.16 obeying $l = 0$. Phonon symmetries are according to MoS_2 and are omitted for clarity of presentation. The vertical line depicts the spectral full width of half maximum of the probing X-rays.

of the newly added data points fall in line with those measured without an out-of-plane component, when considering phonons with energies $\hbar\omega_p \gtrsim 7$ meV. The deviation for data points with considerable difference to the trend and the calculated dispersion is considered to originate in the mixed scattering geometries. In these geometries the polarization of the X-rays will allow coupling to all phonon oscillation directions, hence resulting in spectra with multiple, convoluted peaks. Note that the X-ray probe has a spectral width of 3 meV. This leads to strong overlap of neighboring branches. The same is true for the branches of the optical phonons, especially at the K point, where all but two branches are found in an energy range of only 3.5 meV. Furthermore, due to the low scattering probability of optical phonons in IXS experiments, low signal-to-noise ratio results in a larger error in the determination of the phonon energies. Still, excellent agreement is observed, e. g. for the $A_{2u}^{2\Gamma}/B_{2g}^{2\Gamma}$ and $A_{1g}^{\Gamma}/B_{1u}^{\Gamma}$ Davydov pairs in $\Gamma - M$ direction. In general a good set of data points is attained for the latter pair, which only yields weak signal, since the oscillation is performed mostly by the light sulfur atoms throughout the entire BZ. For the $E_{1g}^{\Gamma}/E_{2u}^{\Gamma}$ Davydov pair, which was undiscovered in the measurements of MoS₂, scattering was observed in between the K and M points and in the vicinity of the Γ point, in good agreement with the phonon energies obtained by Raman scattering. Moreover, the IXS measurements are in line with the DFT-D3 calculations, completing the evaluation of the DFT calculations with van-der-Waals correction. Due to its predictions being well in line with the experiment for these layered TMDCs it might be considered quantitatively for similar materials, where experimental data is not present.

Returning to the acoustic phonons with small in-plane momentum, a large distribution of energies is present, as predicted. Yet the data points are only observed in between the $A_{2u}^{1\Gamma}$ (ZA) and $B_{2g}^{1\Gamma}$ (ZO) branches. Figure 4.19 depicts the measured dispersion of WS₂ acquired in the out-of-plane scattering geometries in the vicinities of the $(00l)$ Bragg points with $l \approx 9.5 \dots 12.5$. The plots show that the measured phonon energies cover the area spanned by the two branches of a Davydov pair, nicely seen for the $A_{2u}^{1\Gamma}$ (ZA) and $B_{2g}^{1\Gamma}$ (breathing, ZO) branches. To allow differentiation, data points with significant deviation ($|\Delta l| > 0.2$ reciprocal lattice vector units) from the $l \in \mathbb{N}_0$ condition are colored in green. Data points close to a $l \in \mathbb{N}_0$

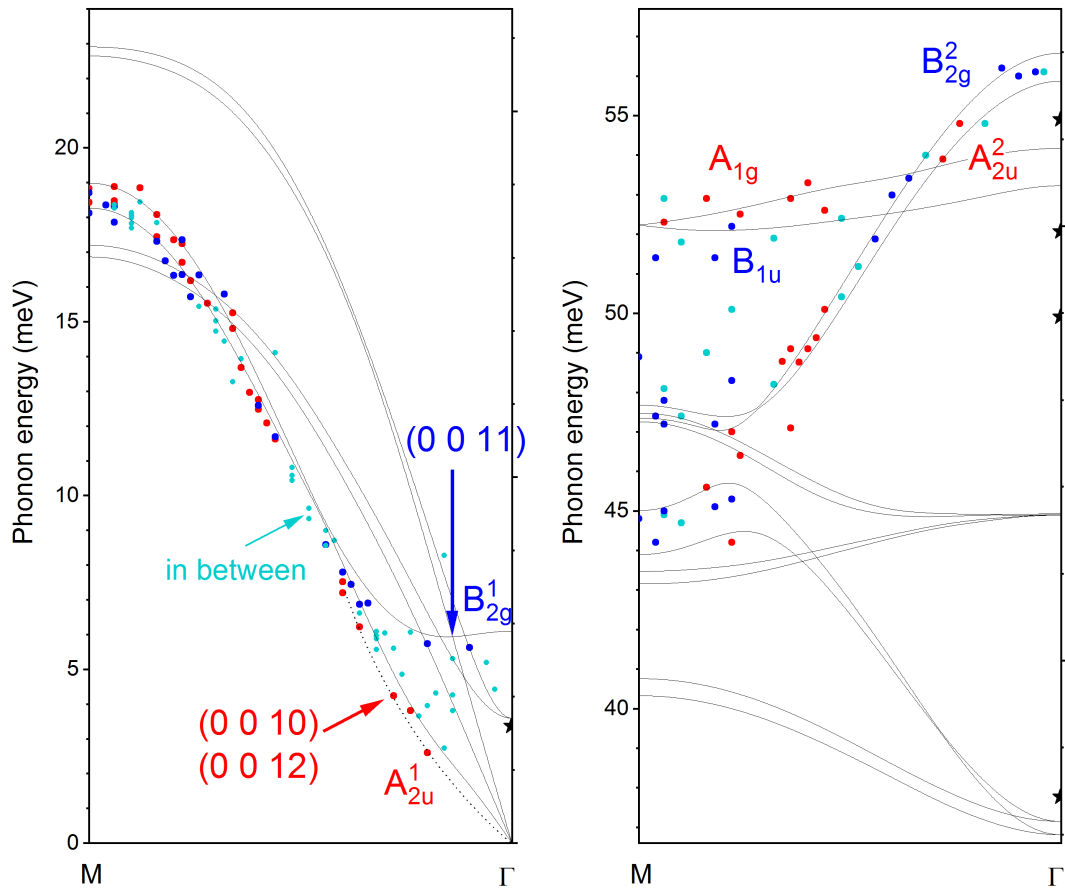


Figure 4.19.: Dispersion in WS_2 for the out-of-plane scattering geometries along Bragg peaks $(00l)$ with $l \approx 9.5 \dots 12.5$ in the $\Gamma - M$ direction. Data points are color-coded whether they are measured in the vicinity of an even- l (red) or odd- l Bragg peak (blue), or in between (green).

are colored in red (blue), if the corresponding Bragg peak has an even (odd) Miller index l . With this color coding it is evident that the acoustic A_{2u}^1 branch is observed at Bragg peaks with an even- l , while the breathing-like B_{2g}^1 mode is observed at odd- l Bragg peaks. Scattering points in momentum-space with a significant deviation exhibit phonon energies in between the A_{2u}^1 and B_{2g}^1 branches. Taking the out-of-plane dispersion of these two branches into account (cf. Fig. 4.17), the *in between* points show a continuous transformation of the acoustic into the optical branch, and vice versa.

For the optical branches a similar behavior can be observed, however with larger scattering, due to lower signal-to-noise ratio. Still, close to the M point peaks observed near even- l Bragg peaks are at higher energies than observed odd- l peaks. This indicates predominant signal of the A_{1g} at even- l Bragg peaks, while the B_{1u} is observed at odd- l peaks. An indication of the same behavior can be observed for the A_{2u}^2/B_{2g}^2 Davydov pair.

Consulting the dynamical structure factor calculations in figure 4.20 the experimental observations are confirmed for most cases: The A_{2u}^2 / B_{2g}^2 as well as the A_{1g}^2 / B_{1u}^2 modes show signal at even- / odd- l Bragg peaks, respectively. The simulations of the low energy A_{1g}^1 (ZA) and B_{1u}^1 (breathing, ZO) branch only show a partial agreement. While a strong shift in scattering intensity from one branch to the other is observed, the simulations show a finite residual signal at the respective other Bragg peak for the experimentally non-observed branch. In general, the scattering cross section of long wavelength acoustic phonons strengthens with strong Bragg peaks. This is due to the fact that $S(Q, \omega)$ converges to the structure factor of the Bragg peak $S(H, \omega)$ for $q \rightarrow 0$ (cf. eq. 4.2, page 42). Since the (0 0 11) Bragg peak is forbidden, the overall scattering cross section of the acoustic A_{2u}^1 branch goes to 0. Consequently at strong Bragg peaks, such as the (0 0 10) and (0 0 12) peaks, a strong signal is expected for the acoustic branches. For the optical branch the observations are of opposite nature, as optical branches are strongest at weak Bragg peaks [109].

Revisiting the dispersion plot in figure 4.19, one observes the quadratic dispersion for the values at even- l Bragg points, hence for the ZA branch, also in WS₂. This observation again underlines the 2D-nature of TMDCs even in their bulk forms

4. Phonon dispersions of TMDCs

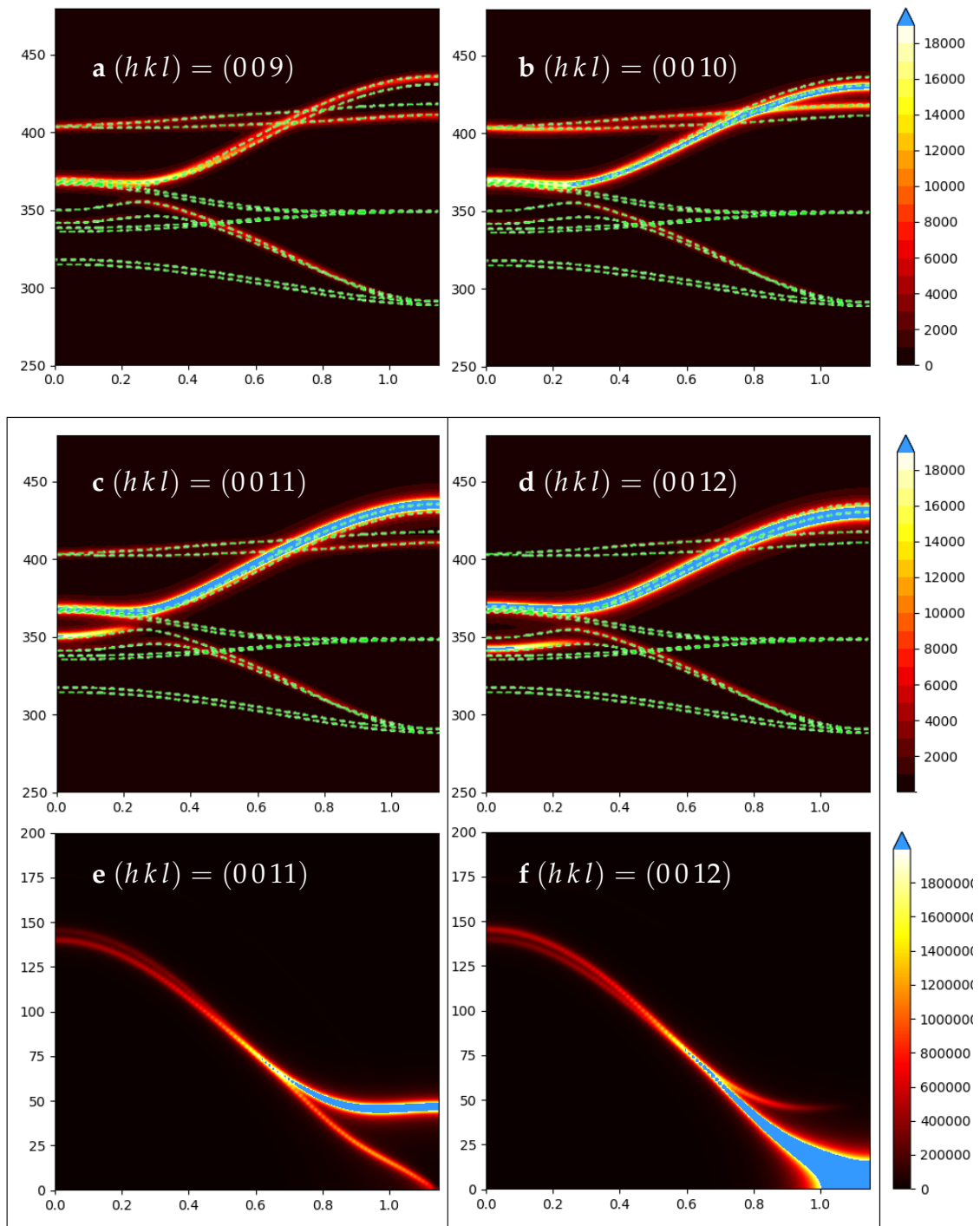


Figure 4.20.: Simulated dynamical structure factor at the $(0\ 0\ l)$ Bragg peaks with $l = 9 \dots 12$ in the $M - \Gamma$ direction.

and strengthens the observations made with MoS₂. A dotted guide to the eye has been inserted, where the DFT calculations were not able to fully reproduce the van-der-Waals force driven nature of this branch.

4.4. Comparison of the phonon dispersion from IXS with the literature

For WS₂, only one experimental determination of the phonon dispersion by inelastic neutron scattering is present. In this work Sourisseau *et al.* [121] present the dispersion of phonons with Σ_1 and Σ_3 ($\Gamma - M$) as well as T_1 and T_3 symmetry ($\Gamma - K$). The branches with Σ_1 and T_1 symmetry correspond to the E_{1u}^Γ (LA) and E_{1u}^Γ (LO) branches with A_1 symmetry and those with Σ_3 and T_3 symmetry correspond to the E_{1u}^Γ (TA) and E_{1u}^Γ (TO) branches with B_1 symmetry [119]. A good agreement can be found, when comparing the INS T_1 branch to the transverse in-plane branch and the T_3 to the longitudinal branch. Although, for larger momentum, INS measurements indicate higher phonon energies.

In the case of the $\Gamma - K$ direction, only little agreement is found. The Σ_1 branch

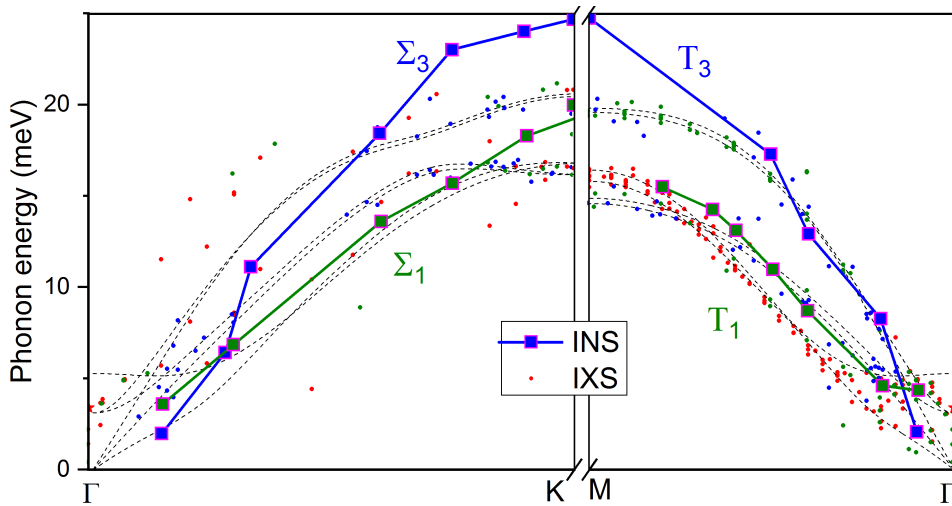


Figure 4.21.: Comparison of the phonon dispersions in WS₂ obtained by IXS and INS [121] for the low-energy branches. Squares depict INS measurements, while (green / blue / red) circles depict IXS data.

rather agrees with the transverse out-of-plane branch for momenta up to $\frac{3}{4}\overline{\Gamma K}$. For higher momenta the INS measurements again exhibit larger phonon energies. The first data point of the Σ_3 branch is in excellent agreement with the A_{2u} (ZA) branch. At higher momenta, however, the INS measurements, again, overshoot the IXS measurements and DFT calculations.

It might be noteworthy that in a follow-up publication [125], the data points of the Σ_3 and T_3 branches only cover the two data points with smallest phonon momentum.

Considering the agreement of the INS and IXS data only at low momenta in the context of the accordance of IXS and DFT, one can conclude that the IXS measurements substantially advance the understanding of the phononic properties in WS_2 .

4.5. Conclusion: inelastic scattering on TMDCs

In this chapter, I have shown results of inelastic X-ray scattering measurements on MoS_2 and WS_2 to obtain the basal plane phonon dispersions. For both materials the presented measurements are the first covering the full basal plane dispersion along the $\Gamma - K - M - \Gamma$ directions. The measurements were supported by dynamical structure factor simulations to interpret and discuss the data. With the simulations as well as considerations of the phonon displacements and their coupling to the respective scattering geometries, activation and deactivation of branches were explained.

For MoS_2 all but the $E_{2u}^\Gamma/E_{2u}^\Gamma$ (LO) Davydov pair were experimentally determined. The measurements are in excellent agreement with DFT-D3 calculations. The shortcoming of the measurement of the $E_{2u}^\Gamma/E_{2u}^\Gamma$ (LO) Davydov pair was cleared by the measurements on WS_2 , which provides data for these branches, again exhibiting good agreement with the DFT-D3 calculated dispersion.

A quadratic dispersion of the ZA branch around the Γ point could be observed for both materials, providing evidence of the 2D nature of TMDCs even in their bulk form.

From the evaluation of the out-of-plane dispersion I was able to find that only little error has to be taken into account for most phonons for the projection of reciprocal space points onto the basal plane. This negligible dependency on the Miller index l further underlines the 2D-nature of this material. While little error in the energies is observed, I have been able to observe the systematic activation and deactivation of the two branches of the same Davydov pair in basal planes with even or odd Miller index l . This can be exploited in future experiments to probe signal of a specific branch of desire.

Furthermore, the small out-of-plane dispersion allowed the usage of a larger subset of the measured data, which was selected and evaluated with a custom python script, yielding a better coverage of the of the dispersion.

The presented data on the phonon dispersion lay the foundation for the investigation of phonon related processes in TMDCs. The observations are also applicable to their single-layered forms, as the observation of the flexural mode as well as the little dispersion in the out-of-plane direction indicate that the materials' properties are governed by the single-layer building blocks, of which the bulk material is constructed.

5. Resonances of the degree of circular polarization with excitonic transitions

Parts of this chapter have been published in [126].

In this chapter I will discuss the resonance behavior of the conservation of circular polarization. At first I will discuss the results of measurements performed at 20 K on two MoS₂ samples (hereafter described by “series 1” and “series 2” MoS₂, resp.). In a second section I will evaluate the influence of adsorbates on the resonance and close this chapter with a comparison of my data with the literature.

The question of why the valley polarization in TMDCs is not conserved in full and is subject to large variation, both for different TMDCs and for different samples of the same material is subject of current debate in the community. Different mechanisms leading to a reduced valley polarization (or *depolarization mechanisms*) have been suggested, some include scattering on phonons.

One of the reasons for the diverse speculations on the depolarization mechanism is certainly the lack of data with excitation close to the emission lines, in particular from within the energy range of two LA(*K*) phonons above the emission energy. I have been able to overcome the technical restrictions of previously reported results by using a triple monochromator setup. Further, in contrast to previous reports, I used tunable lasers to analyze the resonance, rather than detuning the emission by

5. Resonances of the degree of circular polarization with excitonic transitions

changing the sample temperature, as has been done in most previous publications. This enables to decouple the observations from temperature induced effects, which are proven to be strong [127].

For samples used in the experiments shown in this chapter, the single-layeredness was verified by measuring the differences of the Raman shifts of the A'_1 and E' for MoS_2 and by observing the A'_1 mode at $\omega = 239 \text{ cm}^{-1}$ and the absence of the few layer/bulk $A_{1g}/A'_1/B_{2g}^1$ mode [60, 79, 128, 129] for MoSe_2 . Furthermore, the PL spectra were checked for the absence of the indirect band gap originated I peak. Figure 5.1 depicts Raman spectra of prototypical MoS_2 and MoSe_2 flakes, providing evidence for single layer flakes.

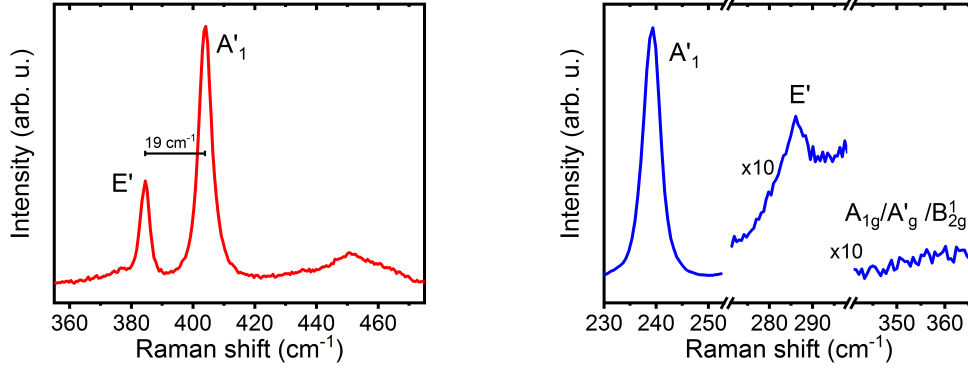


Figure 5.1.: Raman spectra of the MoS_2 (left) and MoSe_2 flakes (right) with 532 nm excitation. The SL nature is proven by the Raman shift difference of the A'_1 and E' for MoS_2 and by the observation of the A'_1 mode at $\omega = 239 \text{ cm}^{-1}$ and the absence of the few layer/bulk $A_{1g}/A'_1/B_{2g}^1$ mode [60] for MoSe_2 . (These images are part of the SI of Ref. [126]).

5.1. Circularly polarized photoluminescence spectroscopy of single-layer TMDCs

Typical circular-polarization resolved photoluminescence (PL) spectra at 20 K are shown in Fig. 5.2. For MoS₂, the *A* emission is found at 1.897 eV (the trion peak emerges after irradiation with higher laser powers, cf. Fig. 3.3 below on page 33). The *B* exciton emission is found at 2.060 eV, 163 meV above the *A* peak, which is in good agreement with the combined conduction band and valence band spin-orbit splitting values of a few meV [12] (CB) + 160 meV [67] (VB). An additional peak at 1.803 eV can be observed, potentially caused by localized excitons (L) [130, 131]. Furthermore, Raman lines are superimposed on the PL emission (cf. Fig. 5.2, marked with asterisks). In the case of MoSe₂, the emission lines of the *A* and *A*⁻ have a full width at half maximum smaller than the trion binding energy, and are

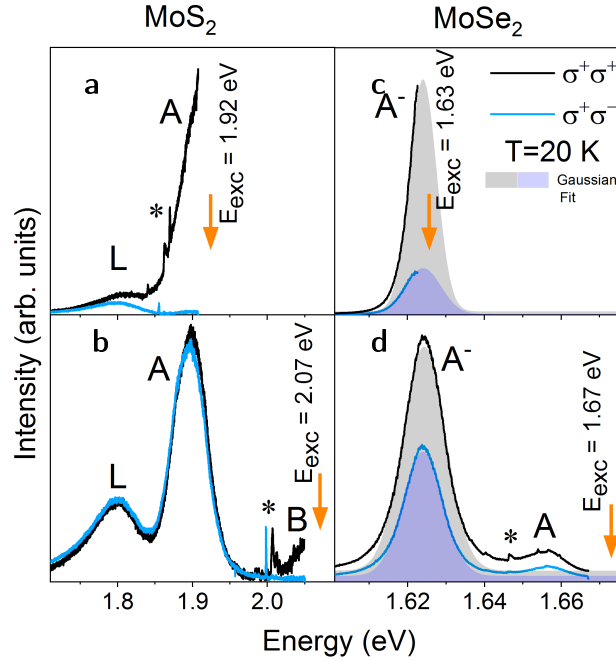


Figure 5.2.: Typical circular-polarization resolved PL spectra in resonance with the *A* (a) and *B* exciton (b) of MoS₂ and spectra in resonance (c) and out of resonance (d) with the trion of MoSe₂. Arrows indicate the excitation energies. Narrow peaks in the vicinity of asterisks (*) are due to Raman scattering and were excluded for fitting. This figure has been published in Ref. [126].

5. Resonances of the degree of circular polarization with excitonic transitions

therefore well separated at energies of 1.656 eV and 1.624 eV, respectively.

Figure 5.3 a depicts the circularly resolved photoluminescence intensity of the A exciton emission as a function of the excess energy ΔE , i.e. the energy above the emission line $\Delta E = E_{\text{exc}} - E_{\text{PL}}$, for the “series 1” MoS₂. The intensity is determined by the area under the Gaussian curve of the fitted peak. With increasing excess energy ΔE up to ≈ 50 meV, a reduction of the intensity of the co-polarized emission can be observed. At higher excess energies, the intensity is relatively constant. For the counter-polarized emission an increase of the intensity is observed, starting at zero for $\Delta E = 0$ meV excess energy. Above about 150 meV, it remains roughly constant at the same value as the co-polarized emission, resulting in the degree of polarization (DOP) ρ converging to $\rho = 0$. The reduced emission intensity for the co-polarization at higher excess energies is due to the reduced absorption, when leaving the resonance. This is corroborated by the agreement of the trend of the intensity with the line shape of the PL emission and the absorption (taken from Ref. [67]). The sample used for the absorption measurements in Ref. [67] is mechanically exfoliated on a SiO₂ substrate, hence comparable to the samples of my studies.

The accordance of the equality of co- and counter-polarized emission intensity at the valence-band spin-orbit splitting has to be considered a coincidence, as for the “series 2” MoS₂ sample equilibrium is restored at lower excess energies (seen as the decrease of the DOP ρ in Fig. 5.4). Furthermore, if the data of MoS₂ and MoSe₂ are interpreted in the same picture, one finds that the decline of the counter-polarized emission of MoSe₂ is only at very low excess energies (see Fig. 5.3 b), while the valence band splitting occurs at higher energies than in MoS₂. For MoSe₂, a strong enhancement of the trion emission at energies around the neutral exciton energy is observed. This stems from the strong absorption of the exciton and subsequent relaxation into the trion state. The degree of polarization, however, does not drastically change around this energy (see Fig. 5.4 below), from which I conclude that the degree of polarization of the trion emission is not affected by the additional absorption and relaxation channels.

Note that each pair of co- and counter-polarized measurement (i.e. pair of data points in Fig. 5.3) was taken at a different spatial position for experimental reasons.

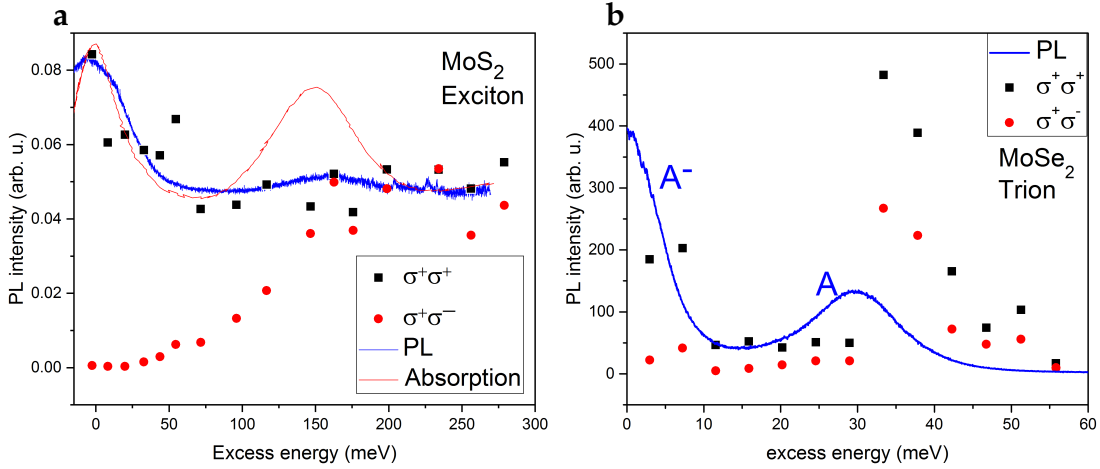


Figure 5.3.: Photoluminescence intensity of the A exciton emission of MoS_2 (a) and the trion emission of MoSe_2 (b) as a function of the excess energy. A PL spectrum has been included as i) a guidance for the energy scaling and ii) to visualize the potential accordance with the trend of the co-polarized intensities. The absorption spectrum is acquired from Ref. [67]. Figure b has been published in Ref. [126].

Therefore, slight changes in the dielectric environment of the measured spot can lead to strong differences of the PL intensity and thereby result in a significant but unknown error for the PLE spectra. This can be clearly seen for the data points corresponding to an excess energy of 55 meV for MoS_2 . Both polarizations exhibit an enhancement in intensity compared to their spectral neighbors, while the trend of the calculated DOP ρ (Fig. 5.4) is smooth.

5.2. Resonance of the degree of polarization $\rho(\Delta E)$

In Fig. 5.4 the resonance behavior of the DOP ρ (black and orange symbols) is depicted. When increasing the excitation energy, thus providing excess energy ΔE^1 to the system, a short plateau with full conservation ($\rho = 1$) in the case of MoS_2 is observed. The energy range of the plateau is sample dependent (cf. Fig. 5.4 a), which can potentially be attributed to environmental and structural effects.

¹Note that the term “excess energy” is used for the energy difference of the excitation and observed emission. This should not be confused with e. g. the exciton kinetic energy.

5. Resonances of the degree of circular polarization with excitonic transitions

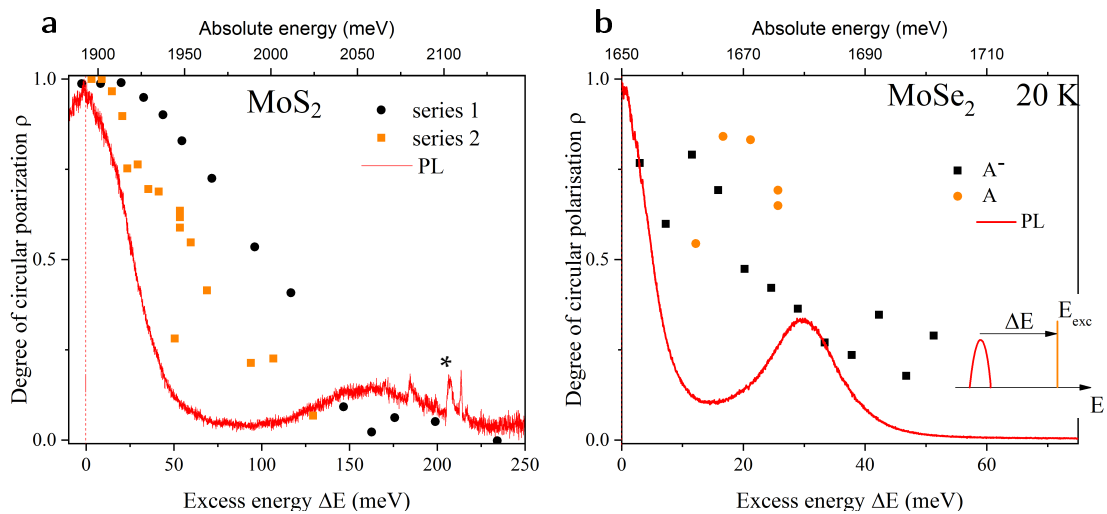


Figure 5.4.: Degree of circular polarization ρ of the A exciton of MoS_2 (a) and A^- trion of MoSe_2 (b) plotted as a function of the photon excess energy ΔE (black and orange symbols). Photoluminescence spectra are plotted as a guidance for the energy scale, superimposed Raman lines are marked with an asterisk (*). The inset depicts the definition of the excess energy ΔE .

Environmental effects include surface adsorbates, which are likely to be present in the series 1 sample. Measurements of this sample were taken ten months after exfoliation; other experiments with low laser power and in cryogenic environment had been performed before. During this period the flake was stored in ambient conditions. In contrast, the flake for series 2 was put in vacuum and was measured shortly after exfoliation.

Consulting AFM micrographs² of the two samples gives further insight (Fig. 5.5).

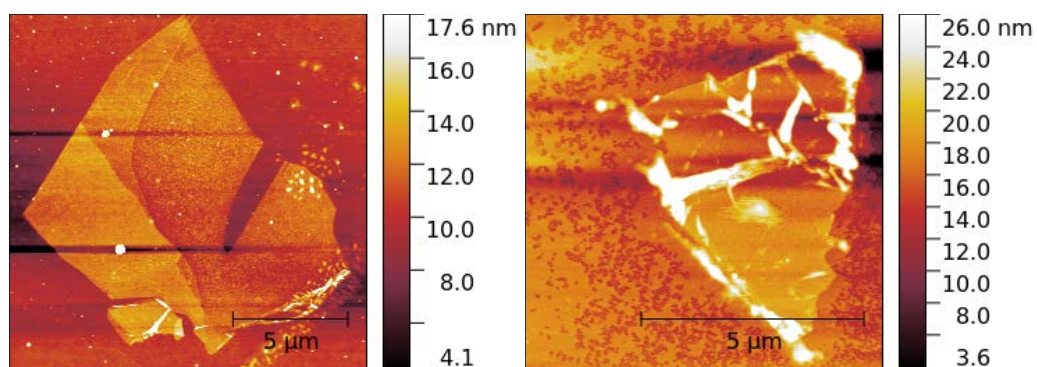


Figure 5.5.: Atomic force microscope images of the series 1 and 2 samples.

While the series 1 sample consists of flat areas, the second sample exhibits a large and irregular height distribution. This height distribution can be decomposed into elongated areas on the inside of the flake and irregular patterns that can be found on most parts of the micrograph. The elongated structures can be attributed to wrinkles of the flake itself, since their orientation is aligned to the edges of the flake, i. e. to lattice planes. Due to the breaking of the crystal's symmetries, a wrinkle could lead to the breakdown of the valley polarization. However, this effect is not dependent on the excess energy provided by the photon. Hence, the different onset of the samples 1 and 2 can not be explained by a breakdown of valley polarization due to a breakdown of the symmetry.

The irregular height variation is considered to be a signature of residue of the adhesive tape which could influence the internal depolarization mechanisms on the surface in a plethora of ways, e. g. through donating charges of specific or arbitrary spin into (unpopulated) valleys. This emphasizes that the sample quality is of importance, since single-layer "2D" materials only consist of surface. Further investigation of the effects of adsorbates will be discussed in section 5.3 below.

For MoSe₂, no plateau but only the decline of polarization for rising excess energies ΔE is observed (Fig. 5.4 b).

Considering the initial injection of carriers in the respective K point ρ_{inj} (*i*), the exciton lifetime t_0 (*ii*) and the depolarization time t_{pol} (*iii*), the DOP ρ in steady state conditions can be written as [132]

$$\rho = \frac{\rho_{\text{inj}}}{(1 + t_0/t_{\text{pol}})}. \quad (5.1)$$

In the following I will discuss the potential effects of the change in excitation energy on the DOP.

(*i*) The dependence on ρ_{inj} reflects how many of the excited excitons (or more general charge carriers) are populating the K valley corresponding to the circular polarization of the exciting photon. By exciting at energies above the A exciton states, processes potentially reducing the injected polarization become accessible,

²AFM measurements were supported by Emanuele Poliani (Technische Universität Berlin).

5. Resonances of the degree of circular polarization with excitonic transitions

e.g. the absorption into the excited states of the A exciton, into the B exciton state and into the numerous contributions to the C band [14]. Direct generation of the excited states of the exciton, e.g. in the $2s$ state at an excess energy of about 200 meV [14, 133] (i.e. for MoS₂ at higher energies than the B exciton), would contribute to a high initial polarization ρ_{inj} through intra-valley relaxation into the excitons ground state. Generation of B excitons in the same valley is allowed as the selection rules are the same, however, the electron and hole spin are opposite to the A exciton (see Fig. 2.6, page 17). Intra-valley relaxation into the A state would consequently need the spins to flip, but would result in a high ρ_{inj} . However, (potentially efficient single phonon) scattering from the B state to a hot A exciton state in the vicinity of the K' valley would reduce ρ_{inj} . This process should be observable as a drop in DOP when getting in resonance with the B exciton. ρ is already near zero at $\Delta E = 150$ meV, leaving this effect hidden in the measurement uncertainty. Transitions forming the C band in absorption are located at several parts of the Brillouin zone [14]. While some of the carriers are injected in the close vicinity of the K points potentially binding to excitons with spin corresponding to the photon helicity, some are injected in parts of the Brillouin zone with parallel valence and conduction bands, leading to an unknown relaxation destination and spin orientation. In these experiments, I focused on the dynamics at excess energies below the spin orbit splitting of the valence band to investigate the A exciton/trion depolarization mechanism not involving the above described processes. Note that the strongest reduction of the DOP is clearly observable at energies below a substantial contribution of the B exciton.

A model discussed in the community [134, 135] considers the drop in DOP being caused by the reduced absorption, when the resonance is left. Revisiting the PLE spectra shown in Fig. 5.3 one can examine the role of absorption on the conservation of polarization. For the co-polarized emission the intensity is reduced roughly by a factor of 2, which is in accordance with a drop of the absorbance from $\approx 8\%$ to $\approx 4\%$ in between A and B states [67]. For the counter-polarized emission the low signal and its convolution with the signature of the depolarization mechanism do not allow a clear analysis of its dependence on the absorption. However, the required excess energy for the equilibrium of polarized emissions is significantly larger

than the FWHM of the absorption curve, allowing to marginalize the absorption as a driving factor for the depolarization. Further indication that the availability of absorption channels has no direct implication of the conservation is found in the PLE of MoSe₂. At the energy of the neutral exciton a clear rise in the trion PL intensity is detected. However, considering Fig. 5.4 it is clear that the trend of the calculated DOP ρ is smooth and continuous, proving that the additional absorption channel only results in a higher luminosity but not a different DOP. Note that these considerations only hold for the neutral exciton being the additional absorption channel when investigating the polarization charged exciton. The underlying processes are different in the case of higher energy transitions.

A further implication of these observations is that the depolarization is not limited through a (phonon-)bottleneck, which would manifest in a constant counter-polarization while the emission intensity of the co-polarization changes as a function of the absorption efficiency.

(ii) The intrinsic recombination time of the excitons depends linearly on the effective excitonic temperature [136] and thereby on the interplay of excess energy provided by the photons and heat transport within the sample and the cryostat. Experimentally observed lifetimes, however, are not necessarily the intrinsic lifetimes, as extrinsic effects can alter the lifetimes.

Photogenerated excitons will thermalize through scattering on phonons and scatter out of the light cone. These hot excitons are restricted to radiatively decay. Due to this circumstance measured exciton lifetimes are those of the exciton ensemble rather than that of a single state. Measured lifetimes reach up to several ns [137–139]. Further, possible non-radiative channels include exciton-exciton scattering (recombination of one exciton, with its energy transferred to the other in form of kinetic energy or dissolution), interband carrier phonon scattering, exciton capture by defects and the relaxation into dark states [140]. The existence of these is confirmed through the multi-exponential decay of the transient of radiative luminescence [128, 140]. The most important one is argued to be the first, which is proportional to the exciton density and thereby to the excitation power density. Estimated lifetimes range from 2 ps to 5 ps [127, 137, 141] for an exciton density of 10^{12} [140]. This density roughly corresponds to an excitation power of 13 mW on a

5. Resonances of the degree of circular polarization with excitonic transitions

$2\ \mu\text{m}^2$ laser spot, with a lifetime of 5 ps, an absorbance of 10 % and a photon energy of 2 eV. These manifold external perturbations on the exciton's lifetime result in a parameter not readily accessible for the investigation (with cw-experiments) in this thesis. Therefore, the following discussion will focus on other dependencies and, where necessary, consider the lifetime in an uninterpreted (fitting) parameter.

(iii) t_{pol} reflects all processes reducing the DOP, such as the aforementioned depolarization mechanisms, which we now evaluate in more detail. In previous studies performed by Kioseoglou *et al.* [142–144] (combination of variation of temperature and excitation energy to vary ΔE), a similar decrease of the DOP in MoS₂ and MoSe₂ was observed. Combining their own data and selected values from the literature (cf. section 5.4, below), they proposed a model of simultaneous scattering of electron and hole by two LA phonons between the K and K' points (*2LA phonon model*). In their model scattering is only possible if sufficient energy is provided to emit the two LA phonons.³ At higher energies the DOP should follow

$$\rho = 1 \left/ 1 + \frac{C\Delta E}{e^{\hbar\omega_q/\Delta E - \hbar\omega_q} - 1} \right. \quad (5.2)$$

which is equation (5.1) with $\rho_{\text{inj}} = 1$, $t_0 = C\Delta E$ (C being a fitting parameter) and $t_{\text{pol}} = e^{(\hbar\omega_q/\Delta E - \hbar\omega_q)} - 1$. $\hbar\omega_q$ is proposed to be the energy of two phonons facilitating the scattering process. These two phonons are phonons from the K point, i. e. phonons with a wave vector $\overline{\Gamma K}$ (cf. Fig. 5.6). However, the phonon dispersion of MoSe₂ is not experimentally known at the K point. Therefore, the phonon energy

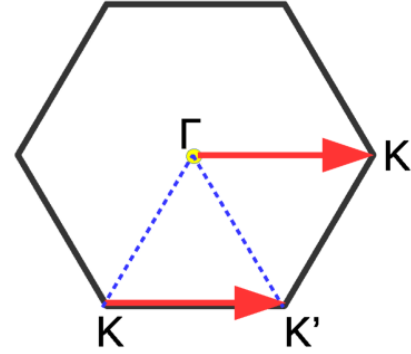


Figure 5.6.: Schematic illustration of the reciprocal space of hexagonal systems; the two arrows are of the same length and orientation, indicating that K to K' scattering requires the momentum of a K -point phonon.

³The authors claim that the *longitudinal* phonons are required for the scattering process. However, also the E' ($E_{2g}^{\Gamma}/E_{1u}^{\Gamma}$ or TA/TO) and E'' ($A_{2u}^{\Gamma}/B_{2g}^{\Gamma}$ or ZA/ZO) phonons exhibit longitudinal oscillations of the molybdenum and sulfur atoms, respectively (cf. table A II).

of $E_{2\text{LA}} = 39 \text{ meV}$ can only be taken from calculations [62]. For MoS₂ IXS measurements find $E_{2\text{LA}} = 59.6 \text{ meV}$ (cf. section 4.2 or [108]). In my measurements of MoS₂, on the other hand, the decrease of the DOP ρ starts already well below 60 meV excess energy (Fig. 5.4 a). For MoSe₂, no full conservation of polarization can be observed. Note that the measurement on MoSe₂ closest to resonance was performed with an excess energy of 3 meV, well below the energy of two LA phonons (Fig. 5.4 b).

A further requirement to be met following the 2LA phonon model of Ref. [143] to access allowed states in the respective other K valley is a spin flip of both the electron and the hole. In Ref. [143] this is suggested to be either mediated by short range scattering on impurities or scattering through the nearly spin-degenerate Γ point [145]. The often observed localized exciton peak L around 1.8 eV might hint at exciton scattering on defects. These could support the scattering between the K valleys. Depending on the type of defect, it could, e.g. allow a spin flip and provide the necessary amount of momentum for an electron (hole) to scatter to the respective other K valley, reducing the required excess energy to one LA(K) phonon equivalent. On the other hand, Mak *et al.* [18] have also observed a “trapped exciton” feature around 1.8 eV and still achieved full conservation of circular polarization with approximately 39 meV excess energy. The second proposed spin flip mechanism, however, is not possible considering excitons, as no excitonic states in an accessible energy range are present. In the single-particle picture (assuming that the exciton binding energy somehow can be overcome), scattering through Γ is not feasible for electrons as the states are about 1 eV higher than the conduction band minimum at the K point. For the hole scattering through Γ would require an additional LA(K) phonon to scatter from the Γ to the K' point, pushing the onset of the decline in polarization to $3E_{\text{LA}}$ (cf. Fig. 5.6, dashed lines.) Further, also the single layer valence bands at Γ are at lower energies than accessible for the photogenerated hole by emission of a phonon [14], hence, rendering them inaccessible without additional energy transfer from the lattice. Figure 5.8 displays the fits of my data with the 2 LA phonon model [equation (5.2)]. While the model follows the data of MoS₂ to some extent, only little concordance is found for MoSe₂. Evaluating the onset of the fit, i.e. the combined energy of the phonons realizing the charge

5. Resonances of the degree of circular polarization with excitonic transitions

transfer between valleys, one obtains 32 meV and 5 meV for the fits of the series 1 and 2 data, respectively. From IXS (section 4.2 or [108]) the phonon energies of the low energy phonon branches at the K point range from 23.3 meV for the E'' (A_{2u}^Γ , B_{2g}^Γ or ZA, breathing-like) to 29.9 meV for the A_1' (E_{1u}^Γ or LA) and A_2' (E_{2g}^Γ or shear) modes. With these values the fits do not meet an agreement with the demand of $2E_{\text{phonon}} = \hbar\omega_q$.

Considering hot carriers being subject to scattering would allow to consider phonons with a smaller wave vector q , and hence different energy. The reduction of the wave vector would cause a red shift of the phonons of the A_1' and A_2' branches. However, since these are the highest energy branches under consideration, the assumed red shift is negligible regarding the difference to the fit result. The other four branches (with E' and E'' symmetry) exhibit almost no dispersion in the close vicinity of the K point. Therefore, hot carriers being responsible for a softening of the 2LA-requirement can be discarded.

For series 1, the onset is similar to the energy of one A_1' or A_2' phonon. This might be an indication for a one phonon assisted process. This is a reasonable consideration for doped samples, with readily populated valleys in the K and K' points for either electrons or holes for n- or p-type samples. In an n-type system, a photogenerated exciton at the K point could scatter with a K' electron. Consequently, the change in momentum through the emission of a K' point phonon would allow the hole to scatter to the K' point and bind with the doping-originated electron (see Fig. 5.7 a). Considering a simultaneous (anti-parallel) spin-flip of both the hole and the doping-originated electron, would restore energy-, momentum- and angular-momentum conservation in the process. Note, that a spin-flip for electrons is not prohibited by a large spin-orbit splitting, such as in the valence band, and that MoS₂ samples are typically considered n-type doped [69].

Similarly, this process could be regarded as a valley exchange related momentum-indirect trion decay (see Fig. 5.7 b). A trion $|e_1^K h_1^K e_1^{K'}\rangle$ could decay into an exciton $|e_1^{K'} h_1^{K'}\rangle$ and a free electron $|e_1^K\rangle$, with the hole exchanging the K points and flipped spins of the formed exciton. In contrast to the exciton-electron scattering process, the requirement of the excess energy, i. e. the onset of the decline in DOP, would not

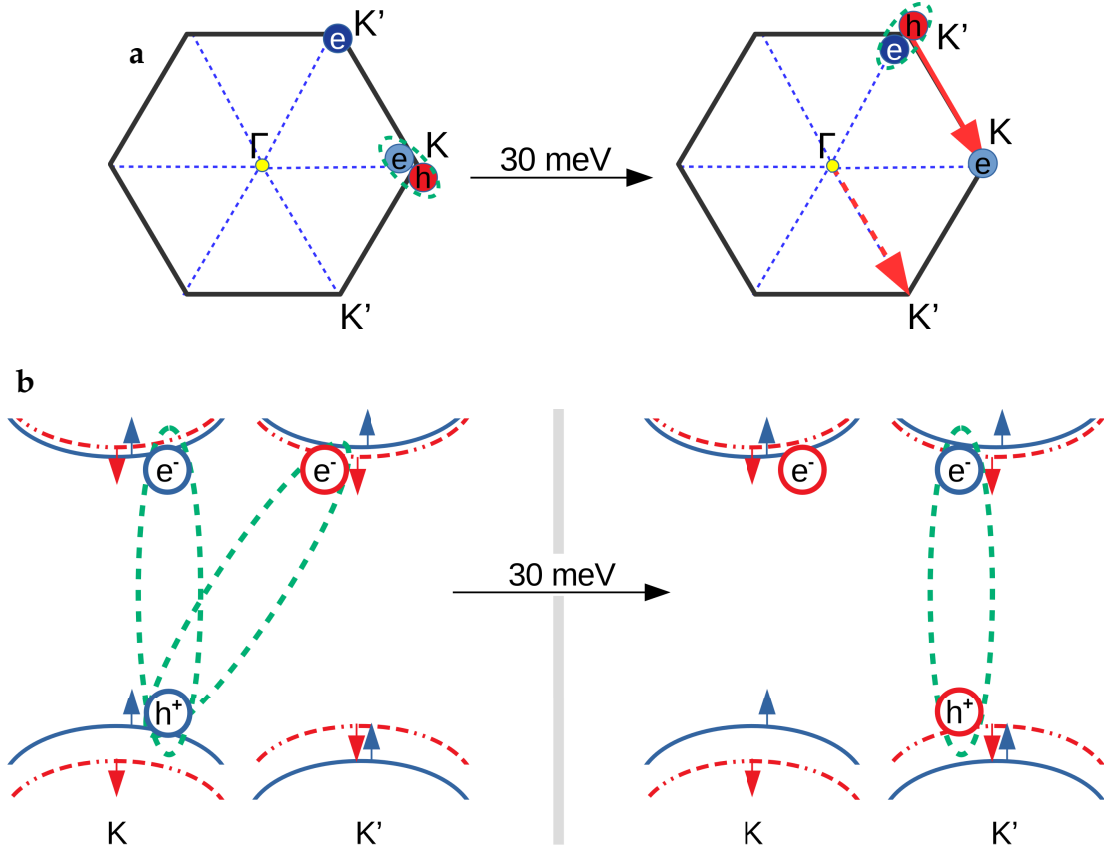


Figure 5.7.: Schematic illustration of the proposed valley depolarization mechanisms for the scattering of a single hole from K to K' (a) and the decay of a momentum-indirect trion (b). Left and right sketches illustrate the initial and final state, respectively.

be due to the emission of a phonon for momentum conservation but due to the trion binding energy. Further theoretical investigation of these processes is necessary, to evaluate the applicability and whether it has a competitive probability.

In another approach, Baranowski *et al.* [146] attributed the decline in the DOP ρ with rising excess energy to the valley exchange mechanism. The PLE measurements of Ref. [146] (at 4.5 K, with varying excitation energy) for MoSe₂ are shown in Fig. 5.8 b for comparison (stars). They present a rate equation model where in steady-state conditions the maximum DOP ρ is depending on the times of excitonic recombination, scattering between the bright and dark states within the valley, and the valley exchange [146]. From these findings they conclude a maximum possible polarization of about 35% in MoSe₂. In my measurements, however, I found a higher

5. Resonances of the degree of circular polarization with excitonic transitions

degree of polarization. According to the Maialle-Silva-Sham mechanism [147], underlying the valley exchange, the exchange efficiency is proportional to the exciton center-of-mass momentum [140]. Assuming parabolic bands, the dependence of the conservation of polarization translates into a proportionality of $\rho \propto 1/\sqrt{\Delta E}$. This relation is fitted to the measurements of MoSe₂ (cf. Fig. 5.4 b, dashed line) and is in good agreement with my data and the values acquired by Baranowski *et al.* [146], however, deviates from those of Ref. [143]. As the assumption of parabolic bands is only valid close to the band extrema, it is reasonable that the fit does not describe the trend at higher excess energies. States with $k_X > k_{\text{photon}}$, leading to the enhanced valley exchange, require an interaction with the lattice to obey momentum conservation. Momentum can either be gained by intra-valley scattering of the photogenerated exciton on phonons or potentially by simultaneous generation (or annihilation) of a phonon. Successive (intra-valley) cooling then enables the exciton in the K' valley to again couple to light and relax radiatively. Consequently, this sequence of processes needs to be as fast as the emergence of the emission with opposite polarization to be relevant. In time-resolved Faraday rotation measurements on MoS₂, a fast decay with a time constant of 200 fs has been measured [148]. Considering fast creation of hot excitons through thermalization with phonons on the order of 100 fs [149], instantaneous valley exchange [150] and fast thermalization (cooling into the light cone) in the K' valley (again ≈ 100 fs), one certainly is within the argued time regime.

Intriguingly the measurements of MoS₂ and MoSe₂ agree to some extent selectively with either the phonon model or the valley exchange derived model (cf. Fig. 5.8). I therefore suggest that the difference might be attributed to different intrinsic properties of the materials. The interplay of different exciton- or electron-phonon coupling and exchange constants as well as lifetimes, and the availability of scattering or relaxation channels could lead to a different dominant depolarization mechanism.

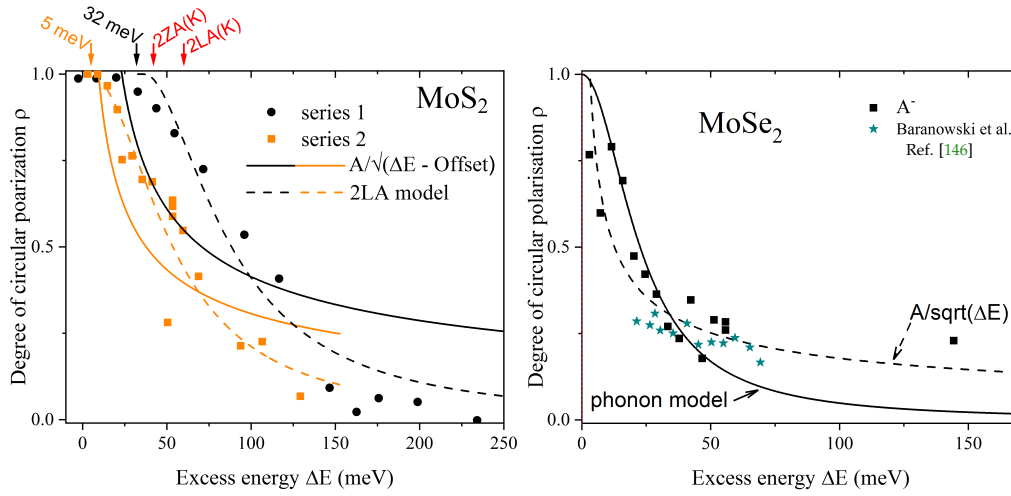


Figure 5.8.: Fits of the DOP of MoS₂ and MoSe₂ following the 2 LA phonon model and valley exchange derived $a/\sqrt{\Delta E}$ relation. Stars depict measurements from Ref. [146].

5.3. Influence of surface contaminants on the PL

A further series of circularly polarized PL measurements was performed on samples that have been annealed in vacuum⁴ at a temperature of 150 °C for 60 h. During this process all adsorbates, such as water, oxygen and nitrogen were removed.

Prior to the measurement no breach of the vacuum was accepted. The final vacuum at room temperature was around $5 \cdot 10^{-7}$ mbar, indicating a low leakage rate and hence low recontamination of the (cooled) surfaces.

Figure 5.9 presents photoluminescence spectra at 20 K measured before and after the annealing process. Fit curves are included for the spectra taken before the annealing process. The spectra acquired on the annealed samples were measured in the XY lab, hence the signal-to-noise ratio differs from the spectra of the pre-annealing samples taken in the LabRAM lab, due to the low sensitivity of the triple monochromator setup.

Comparing the spectra, specific changes induced by the annealing process are

⁴During the heating process the pressure was as high as 10^{-3} mbar due to evaporating adsorbates, however, decreased to 10^{-5} mbar or better after 60 h. Note that the samples were annealed together with the cryostat in which the measurements were performed to exclude recontamination during a transfer process and from desorbing species from the measurement chamber.

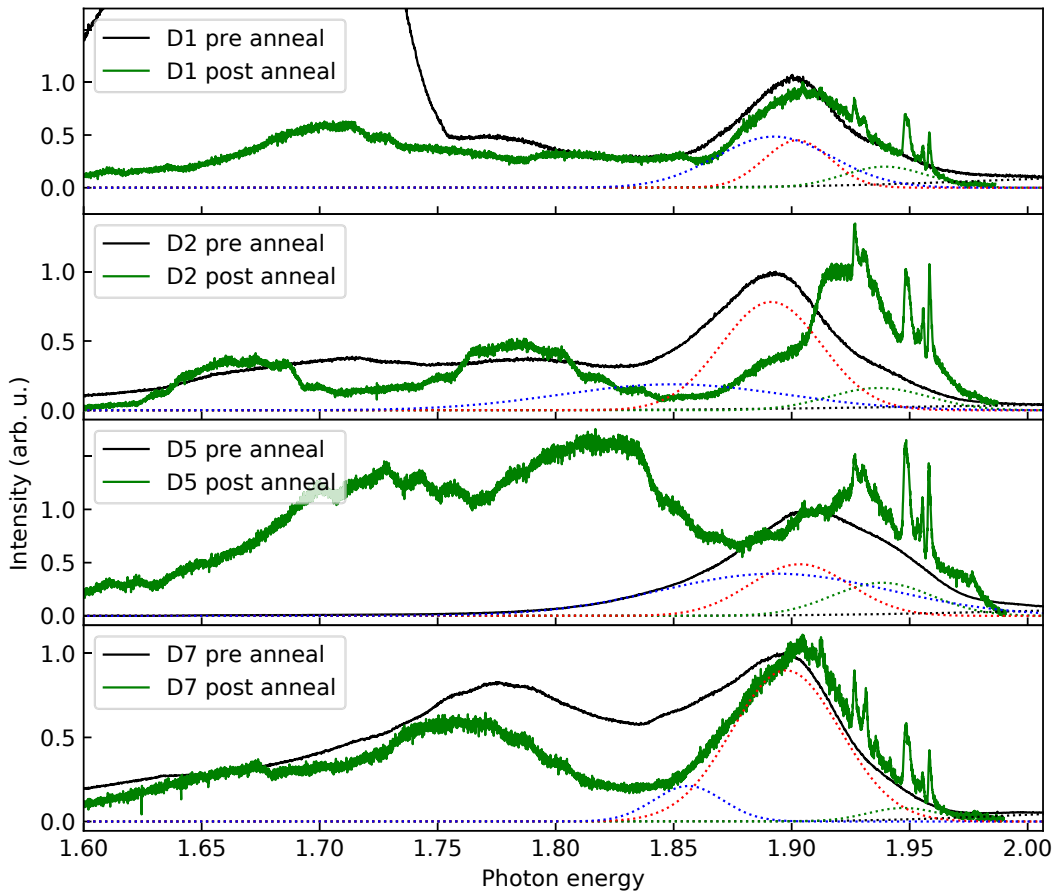


Figure 5.9.: Photoluminescence spectra of the samples prior to and after the annealing process. The post-anneal spectra (green lines) are circularly co-polarized and acquired with an excitation energy of 2.0065 eV (in line with the high-energy border of the plot). Sharp lines in between 1.96 eV and 1.90 eV are Raman lines. Dotted lines depict the fits of the exciton, trion and the highest energy defect contribution to the spectrum.

observed. All four samples exhibit a blue shift of the excitonic transition, which is largest for the D2 sample with a shift of 22 meV. This blue shift is attributed to a change of the dielectric environment. The desorption of molecules leads to a reduction of the dielectric constant of the environment, which then leads to an increased exciton binding energy, in accordance to the Wannier-Mott-exciton formula given in equation 2.6 (page 14). The large shift observed for the case of sample D2 could be due to a larger amount or a different type of contaminant. Since all four samples were treated in the same fashion (handling in air prior to the annealing,

etc.) a different concentration and composition of adsorbed components of air is unlikely. A different type of contaminant could be the presence of residual adhesive tape from the exfoliation process, as observed for the series 2 samples (see AFM micrograph in Fig. 5.5, page 80). The dielectric constant of the adhesive could be significant.⁵ Independent of the exact figure of the dielectric constant, the overall volume of the adhesive is larger compared to a few layers of adsorbed molecules, rendering the adhesive a more effective dielectric. Removing or chemically altering the adhesive could therefore have a large implication on the exciton binding energy, as observed for the shift of the sample D2.

Furthermore, emission below the trion state has changed. In the case of the sample D1 and D7 the relative intensity is reduced, compared to the excitonic transition. While for the sample D5 emission is found where the pre-annealed sample did not exhibit luminescence. For sample D2 the low energy emission remained comparable.

These changes of the low energy luminescence are attributed to the release of adsorbates which could passivate or stimulate luminescence. This kind of behavior has been observed by Tongay *et al.* [131] for the strength of the excitonic emission, where physisorbed adsorbates on sulfur vacancies were found to facilitate the luminescence through charge donation. They found a pronounced (reversible) increase in luminosity when nitrogen was introduced to the sample chamber. In the present case, adsorbates not only loosely physisorbed to the surface, but also adsorbates attached comparably firm to defect sites were desorbed. Therefore the direct electronic structure of these sites has changed, as observed in the changed luminescence before and after the annealing process indicated.

Furthermore, closely evaluating the line shape of the spectra, one observes sudden changes in intensity for the post-annealed spectra at energies below the trion (see also Fig. 5.10). This is explained by a non-constant emission intensity, i. e. a blinking-like behavior: Since these spectra are acquired using a high dispersion spectrometer, a stitching process of multiple sub-spectra is necessary to measure a

⁵Dielectric constants contained in the spec sheets of adhesive tapes are given to ASTM standards [151] and are therefore only covering frequencies up to radio frequencies. The dielectric constant of the used 3M Magic Scotch Tape 810 for the visible range and for low temperatures is unknown.

full PL spectrum. The stitched full spectrum will then have the observed drop or increase whenever the signal significantly changed over time. The depicted spectra are acquired by averaging two sub-spectra with an accumulation time of 10s each, before stitching. The timescale of the changes in emission intensity, therefore has to be correspondingly long. I attribute these changes to loosely bound adsorbates originating from atoms or molecules of the residual gas in the vacuum. The general long time scale is in line with the low pressure of the sample chamber of $4 \cdot 10^{-7}$ mbar, since kick-out processes and (re-)condensation are rare in these conditions. The magnitude of the observed changes implies a strong influence of relatively few physisorbed atoms and molecules on the electronic system of MoS₂.

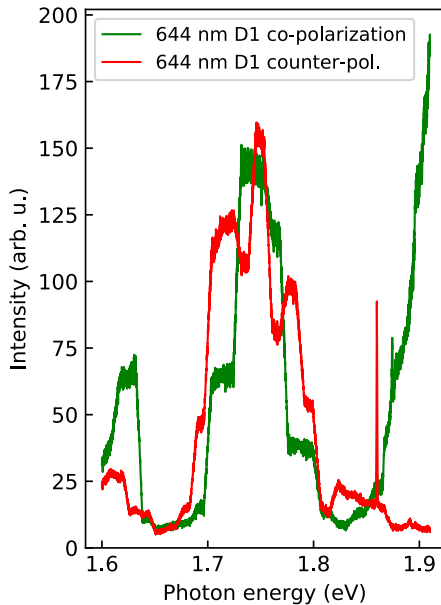


Figure 5.10.: Blinking-like intensity changes of the defect originated luminescence of the D1 sample. The excitation energy coincides with the high-energy frame.

the substrate (e.g. Si/SiO₂). The TMDC material in the desired thickness is then produced by exfoliation onto the viscoelastic PDMA (which sits on a transparent substrate, e.g. glass), allowing to align and stamp the TMDC single- or few-layer

Artifacts originated by the setup (such as temperature induced drift of the sample, air motion or vibrations coupling to the liquid helium transfer tube, etc.) can be ruled out, since the excitonic emission does not show this effect to the same extent.

From these observations, we can conclude that, due to the 2D-nature of these structures, it is of importance to protect the surface, e.g. from chemical degradation through oxidation in ambient atmosphere (which the selenides are prone to) [152] or changes due to surface contamination.

A possibility to reduce the effects of exposure to ambient air is the encapsulation in a wide band gap layered material such as hexagonal boron nitride (h-BN) through the so-called *all-dry viscoelastic stamping* [153]. In this procedure few-layer h-BN is directly exfoliated onto

onto the h-BN on the final substrate. Stamping a capping (few-)layer of h-BN on-top results in a structure (Si/SiO₂/h-BN/TMDC/h-BN) where the TMDC is decoupled from the substrate and the ambient atmosphere. Ideally this process is performed in an inert atmosphere, i.e. in a glove box to prevent chemical changes and physisorbed water on the interfaces.⁶

A side effect of this procedure is that the crystal properties are closer to its free-standing state, as the interactions with h-BN are low and as h-BN exhibits an atomically flat surface (in contrast to SiO₂). This can result in PL emission lines with narrow peaks, allowing to differentiate exciton and trion emission for MoS₂ [42, 155].

Evaluating the full set of circularly polarized spectra, according to the routine described above, one obtains the PLE intensities depicted in figure 5.11. In general the PLE spectra exhibit the same trend, compared to the series 1 and 2: A strong co-polarization and a weak counter-polarization is observed in resonance, and a convergence towards a similar intensity can be found. Here, however, the co-polarization drops up to an order of magnitude from resonance to non-resonance condition, while the counter-polarized emission remains at low count numbers. In the case of the D2 sample, the counter-polarized emission remains at constant intensities throughout the full measured energy range. This could indicate a bottleneck of the depolarization, which is not dependent on the excess energy, such as the phonon scattering probability.⁷

Sub-figure 5.12 **a** depicts the resonance of the calculated DOP ρ of the annealed samples. For samples D1 and D2 the DOP is given for both the neutral and the charged exciton, while for the samples D5 and D7 only the trion DOP is given, due to

⁶Furthermore, a cleaning step to remove polymer residue off the top face of the TMDC before the structure is capped, might be necessary to obtain best quality samples with clean interfaces (inevitable if hetero-structures with overlap of the sub-structures' electronic systems are desired). It has been shown that dry cleaning the of a single-layer MoS₂ by scanning the surface with an AFM in contact mode removes residue like a snowplough, yielding an enhancement of the luminescence of several orders of magnitude. [154]

⁷The change of the lattice temperature as a function of the photon excess energy is negligible, as proven by constant spectral position of the PL emission in the power series shown in section 3.2 on page 33.

5. Resonances of the degree of circular polarization with excitonic transitions

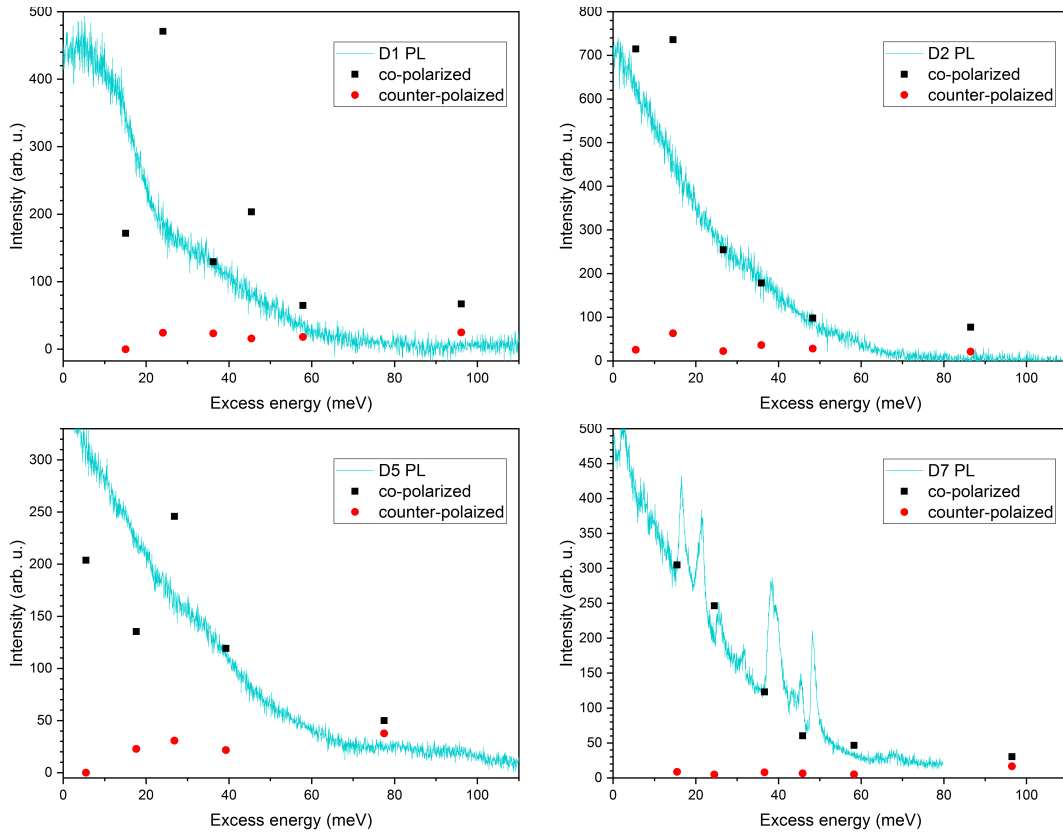


Figure 5.11.: PLE intensities of the D1, D2, D5 and D7 samples' trion emission. PL spectra are included for a guidance for the scaling; for D7 the PL excited with 618 nm (97 meV excess energy) is included, hence superimposed peaks are due to Raman scattering.

a vanishing luminescence of the neutral exciton (cf. Fig. 5.9). In sub-figure 5.12 b a comparison of the DOP's of the annealed samples and those of series 1 and 2 is given. In general, a good agreement of the shape for all series can be found. Differences are mainly found for the point-to-point scattering and the onset of the decline from $\rho = 1$. While the variation of the onset indicates slight differences in the depolarization mechanism, the strong scattering could be partially originated by a variation of the emission intensity over time. However, this variation is, if at a present, on a different time scale than the dynamics observed for the defect bound exciton peaks, since large variation within one measurement was not observed. Still, a slight variation over the period of the measurement (approximately 2×20 min) can not be ruled out. A simultaneous measurement of co- and counter-polarized emission would clarify upon this effect.

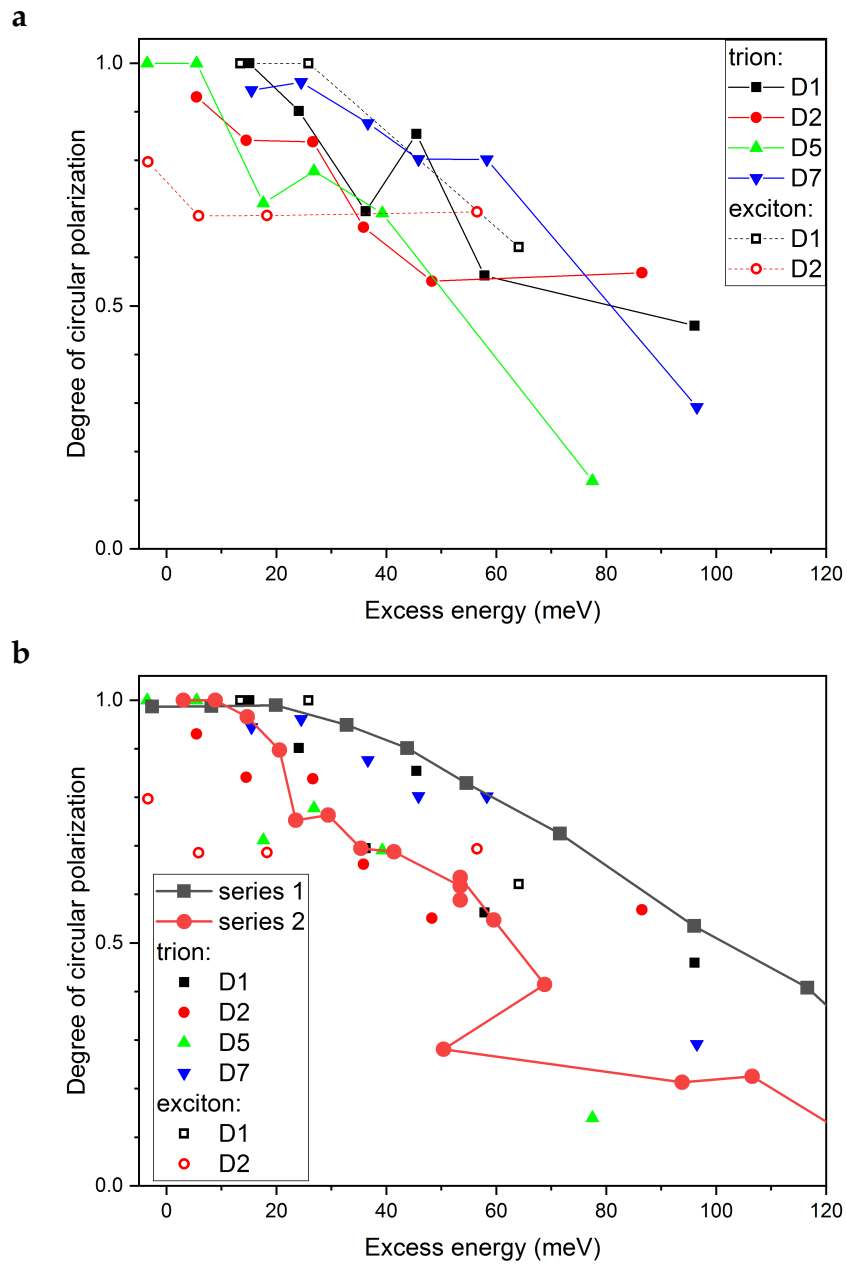


Figure 5.12: **a:** Resonance profile of the degree of circular polarization of the annealed samples. DOP for trions depicted with full symbols while exciton derived data is shown with open symbols. **b:** Comparison of the data shown in **a** with the DOP of series 1 and 2, as of Fig. 5.4 **a**.

In conclusion, the agreement of the calculated DOP's of all samples shows that the observed trend is robust for MoS₂. Furthermore, it proves that the trend does not depend on adsorbates interfering with the internal mechanics, e. g. by donating charges into the valley corresponding to the counter-polarization.

Measurements on samples encapsulated in hBN would allow to better distinguish contributions to the spectra and hence allow for a better analysis, especially of the counter polarized emission, which is often on the scale of the noise and buried in the intensities originating from bound excitons or Raman lines.

5.4. Comparison of DOP ρ values with the literature

Figure 5.13 depicts the values of the degree of polarization (DOP) ρ of “series 1” MoS₂ presented in section 5.2 and the values of Ref. [143] and the references within [143], namely [15, 18, 19, 26]. They mostly fall well in line with my data.

The work of Mak *et al.* [18] contains a comparison of the circularly polarized photoluminescence (PL) emission of single-layer MoS₂ on SiO₂ and on h-BN substrate. I have performed a fit of the spectra in Ref. [18] to obtain the intensity and the spectral position of the emission. From this I determined the DOP ρ and the excess energy ΔE . In the spectra of MoS₂ on SiO₂, the signal-to-noise ratio and the contribution from Raman lines lead to a larger fitting error than in the case of the h-BN substrate. The same procedure was performed to obtain the neutral and charged exciton DOP ρ for the spectra presented by Cao *et al.* [15]. In the work of Sallen *et al.* [26], a temperature series of the circular polarization is presented. For three temperatures (4K, 125 K, and 300 K), the circularly resolved spectra are given, of which I extracted the DOP ρ and emission energies. Further values could potentially be extracted from the temperature series plot of the circular polarization⁸ considering the Varshni equation, however, were omitted here. The last reference used by the authors of Ref. [143] is another temperature series performed by Zeng *et al.* [19]. In this article no circularly resolved PL spectra are

⁸In Ref. [26] no definition of the degree of circular polarization is given.

5.4. Comparison of DOP ρ values with the literature

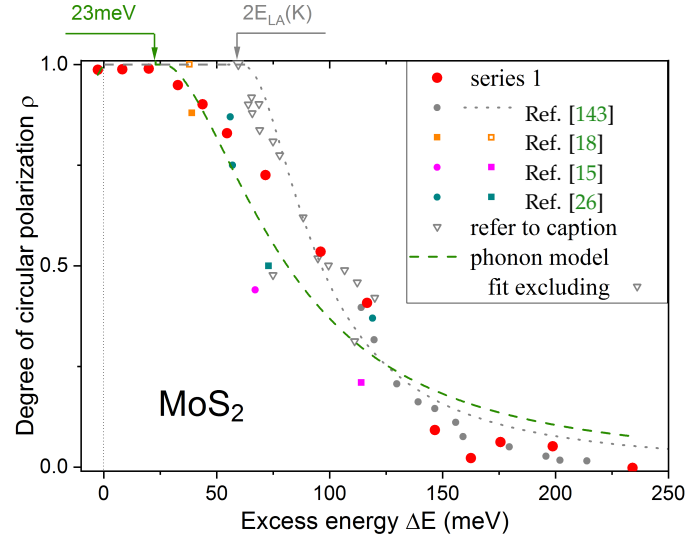


Figure 5.13.: Comparison of DOP values measured in my experiments (presented in section 5.2) and given in the literature. Circles / squares depict the DOP ρ calculated from the emission originated from the exciton / trion. The value obtained for MoS₂ on h-BN (SiO₂) from Ref. [18] is depicted as an open (filled) square. Open triangles depict the values of Refs. [15, 18, 19, 26] as given in Ref. [143]. This figure has been published in Ref. [126].

shown, precluding the above process. Here, the polarization coefficient is differently defined as $P = \pm I(\sigma_{\pm})/I_{\text{tot}}$. Therefore, I did not consider the data of Ref. [19]. The values of ρ extracted from Refs. [15, 18, 26] as described above are summarized in Tab. 5.1 and plotted in Fig. 5.13. Fitting my data and the values of Refs. [15, 18, 26, 143] with the model given in Ref. [143], one obtains the curve plotted in Fig. 5.13 with a dashed green line. The obtained energy onset of the decline given by the fit is $\hbar\omega_q = 23$ meV, different than the value reported in Ref. [143]. I further include in Fig. 5.13 the values of Refs. [15, 18, 19, 26] (open, gray triangles) as plotted and used to fit the phonon model (dashed gray line) by the authors of Ref. [143].

5. Resonances of the degree of circular polarization with excitonic transitions

ΔE (meV)	DOP ρ	remark			Ref.
38	0.98	$T = 14$ K	trion	h-BN	[18]
39	0.88	$T = 14$ K	trion	SiO ₂	
114	0.21	$T = 83$ K	trion	} SiO ₂	[15]
67	0.44	$T = 83$ K	exciton		
73	0.50	$T = 4$ K	trion	} SiO ₂	[26]
56	0.87	$T = 4$ K	} exciton		
57	0.75	$T = 125$ K			
119	0.37	$T = 300$ K			

Table 5.1.: Extracted excess energies ΔE and degrees of polarization ρ from Refs. [15, 18, 26].

5.5. Conclusion: Resonances of the degree of circular polarization

In this chapter I presented circularly resolved photoluminescence measurements with varying excitation energy on samples as exfoliated on SiO₂ and on vacuum annealed samples. With the results of these experiments I evaluated the applicability of different mechanisms, currently debated in the community. I find that the nature of the generation and valley depolarization of excitons in TMDCs is so far not fully understood as none of the proposed mechanisms can describe the DOP in TMDCs in the vicinity of the resonances. However, the trends of the DOP of MoS₂ and MoSe₂ are partly in agreement with the models stemming from the *2LA phonon* mechanism and the valley exchange, respectively. This suggests that more than one mechanism is reducing the DOP in different TMDCs and that the most relevant mechanism is determined by the small, yet important differences of the materials in the MoS₂-family of TMDCs.

Further, I propose a mechanism potentially being responsible for the depolarization in doped samples.

The results obtained from the annealed samples indicate that the sample environment is a crucial component of the electronic system of quasi two-dimensional systems. The comparison of the photoluminescence spectra before and after the

5.5. Conclusion: Resonances of the degree of circular polarization

annealing process reveal that the optical band gap is sensitive to the presence of surface contamination. A blue shift of the excitonic transitions of up to 22 meV was observed as an effect of the environmental changes through the annealing.

Further, a strong dynamic of the luminescence intensity of defect states on the second-timescale was observed, indicating a strong influence of the residual atmosphere, even in high vacuum.

These results clearly indicate that encapsulation of 2D-materials will be necessary to maintain the properties of the material.

6. Summary

In this thesis phononic and excitonic properties in transition metal dichalcogenides were investigated. In the first part, the phonon dispersion relations of MoS₂ and WS₂ have been determined by means of inelastic X-ray scattering. The usage of inelastic X-ray scattering instead of neutron scattering enabled us to probe a single crystallite.

For MoS₂ eight out of the nine Davydov pairs were observed and showed excellent agreement with the van-der-Waals corrected DFT-D3 calculations. Contributions to the ninth Davydov pair were measured in WS₂ and found to be in good agreement with the DFT calculations. This observation completes the overall agreement with the ab-initio calculated dispersion and concludes that these van-der-Waals corrected simulations may also be used in similar layered structures, where no experimental data is at hand. Moreover, the experimental results lay the foundation for theoretical considerations, e. g. regarding the electron phonon coupling, and for the determination of material properties, such as the thermal conductivity and the elastic moduli.

Simulations of the dynamical structure factor have been performed to acquire additional information about the scattering intensities in the IXS experiments. From the analysis of these simulations and the phonon eigenvectors, it was possible to deduct that a destructive interference causes the longitudinal E_{2u}^{Γ} and E_{1g}^{Γ} branches to be obscured in the IXS experiment, for measurements with negligible out-of-plane component. Further, several occurrences of activation and deactivation of branches could be explained considering the dynamical structure factor and phonon displacement patterns. Furthermore, taking the simulations into account allowed to resolve ostensible contradictions of IXS and DFT derived dispersions. This rendered the

6. Summary

simulation of the dynamical structure factor a powerful tool in the analysis of IXS spectra.

A comprehensive overview of the phonon energies, symmetries and displacement patterns has been constructed for MoS₂, which is applicable (apart from the phonon energies) to all TMDCs with D_{6h}^4 symmetry.

In the IXS measurements of MoS₂, a negligible out-of-plane dispersion was observed for the optical phonons with longitudinal displacement in the $\Gamma - A$ direction. Following this observation, the dispersion in $(0\ 0\ l)$ direction along the $\Gamma - K - M$ direction in WS₂ was investigated. The analysis of the DFT data showed negligible dispersion for all (high energy) optical branches as well as for high in-plane momenta in the case of the acoustic and low-energy optical branches. This observation enabled us to consider a larger set of measurements to build the in-plane dispersion relation of WS₂, consequently resulting in a better coverage of the in-plane momenta.

Further, investigation was done on the implication of the out-of-plane component of the reciprocal space point at which the inelastic scattering occurs. It was found that the scattering cross section of the two branches forming a Davydov pair alternates with the Miller index l . For example, the A_{2u}^Γ branch was found to be active in the vicinity of Bragg peaks with even l , while the B_{2g}^Γ branch is only observed at Bragg peaks with odd l . This dependence could be exploited in future experiments to purposefully target specific branches of interest.

In accordance with the low dispersion found in the out-of-plane direction, a quadratic dispersion of the A_{2u} (ZA) branch has been observed for both materials, which further emphasizes the 2D-nature of these layered TMDCs. This strongly suggests that many of the found properties in the bulk materials are applicable to few- or single-layer sheets.

In the second part of the thesis, the effects of the excess energy, i. e. the difference of the photon energy and the exciton or trion state, on the conservation of the degree of polarization was explored. Furthermore, the effects of surface adsorbates through photoluminescence experiments on vacuum annealed samples were evaluated.

Circularly polarized PLE spectroscopy was used to investigate the nature of the

valley depolarization in MoS₂ and MoSe₂. It has been observed that the circular polarization is conserved to a high degree when little excess energy is provided to the system. MoS₂ is found to fully conserve the circular polarization in resonance, while for MoSe₂ a maximum DOP of 84 % / 79 % for the neutral A and charged A^- exciton (resp.) is observed. This value represents the highest reported value of circular polarization observed in MoSe₂. Using these results, several mechanisms discussed in the community are evaluated considering the measured phonon dispersions. While the *2 LA phonon model* shows agreement to some extent with the measurements on MoS₂, the trend of the DOP in MoSe₂ shows a better agreement with the $a/\sqrt{\Delta E}$ model, which was derived from the Maialle-Silva-Sham mechanism. From these considerations, it is evident that the valley depolarization in TMDCs is governed by at least two mechanisms. The most competitive mechanism in different materials is consequently determined by the intrinsic properties of the material.

On the basis of the excess energy-onset of the decline of polarization for one of the MoS₂ samples, being on the order of a single $A'_1(K)$ or $A'_2(K)$ phonon (E_{1u}^Γ or $E_{2g}^{1\Gamma}$ branch, resp.) two further mechanisms are proposed for n-doped samples. The first proposes that a K bound, photo-generated exciton scattering with a K' point electron under the emission of a phonon could lead to an exciton at the K' point, hence reducing the valley polarization. The second proposed mechanism considers a momentum-indirect trion decay. In this case, the onset in the DOP resonance profile is explained by the requirement to overcome the trion binding energy, which matches the onset of the DOP decline and the phonon energy under consideration. A theoretical investigation will be necessary to evaluate the applicability and competitiveness of these processes. Experimentally, insights into the depolarization in connection to doping could be gained by performing measurements on e. g. hBN/SL-TMDC/graphene/hBN hetero-structures through electrostatic doping.

The results, gained by the analysis of the vacuum annealed MoS₂ samples, emphasize the importance of the sample environment in the case of quasi two-dimensional materials. Strong changes in the material upon annealing were observed, indicated by a strong blue shift of up to 22 meV for the excitonic transitions. Furthermore, the annealed samples exhibited a long timescale dynamic, argued to be originated

6. Summary

by adsorbates from the residual gas in the high vacuum, which potentially interferes with the electronic properties. Throughout the investigation of the TMDC few-layer systems, multiple indications stress that the sample quality is paramount and encapsulation is a requirement to fully control and maintain the material's properties.

To further acquire a deeper understanding of the processes underlying the valley depolarization, it will be necessary to perform measurements on clean and atomically flat samples, as can be possibly provided by van-der-Waals hetero-structures. Moreover, it is of high relevance to gain further insights into the sample-to-sample variation and gather larger statistics. For these experiments, a setup using a low dispersion triple-monochromator will be of use, to perform a large number of PLE measurements. Further, the usage of a polarizing beam displacer in combination with a multi-binning read-out procedure of the CCD will allow to simultaneously measure co- and counter-polarized emission and thereby double the throughput and enhance the comparability of the acquired spectra.

A. Appendix

A 1. Design of an IXS-sample holder

A sample holder has been designed to allow highest flexibility in scattering geometries for the measurements on MoS₂ (cf. Fig. A1). On one side it allows grazing incidence in all but the directions where the thin clamps obstruct the beam path. It is fitted with a central 3 mm hole to allow measurements in transmission. The other side has an opening angle of 84°. One corner exhibits a recession of 1 mm with edges parallel to the M3 fittings. A fitted silicon wafer (inheriting the parallelism from the edges) allows the pre-alignment of the mounted sample in correspondence to the mount-axes, e.g., via HRXRD. For the measurements at the ESRF on WS₂ no sample holder was required, as the crystal was directly glued at its edge to a polymer cone (see Fig. 4.12 on page 59).

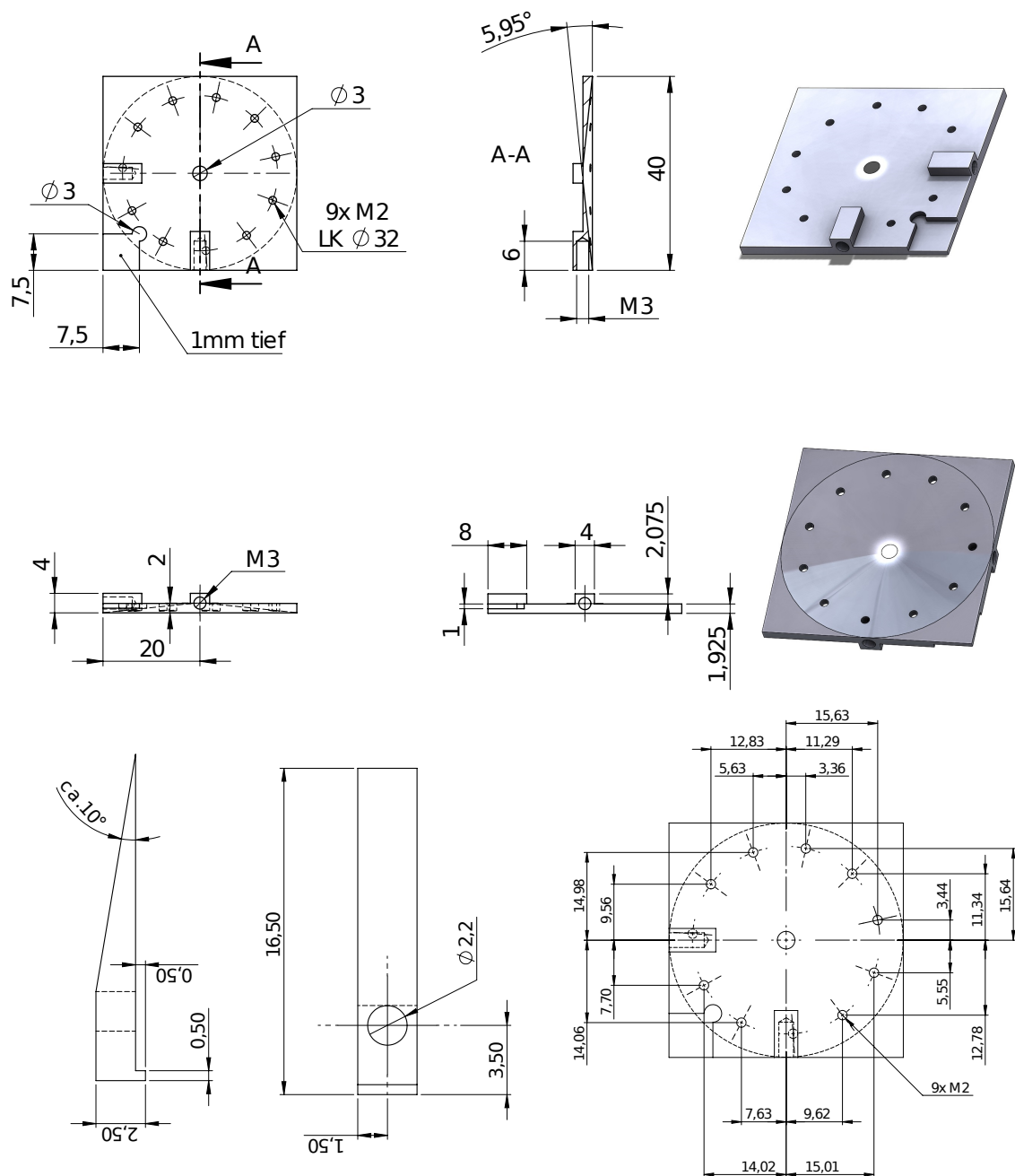


Figure A1.: Drawing of the sample holder and clamps used for the experiments at SPring-8. Designed in collaboration with Andreas Ludewig (Technische Universität Berlin).

A 2. Displacement patterns of phonons at basal-plane high-symmetry points

A comprehensive compilation of all displacement patterns of D_{6h}^4 TMDCs at the Γ , K and M points has been produced, as displayed on the following pages in tables [A I](#), [A II](#) and [A III](#). Each displacement pattern is depicted in the $[0\ 0\ 1]$, $[2\ -1\ 0]$ and $[1\ 1\ 0]$ directions (upper-right (red), lower-left (green) and lower-right (blue) image, resp.). The three projection planes are also depicted in the bottom-right panel of table [A I](#). For each phonon the irreducible representation is given according to the high-symmetry point and for the K and M points of the corresponding phonon at Γ of the same branch. Further, the phonon energies from DFT-D3 calculations are presented in cm^{-1} and meV. Frames surround the displacement patterns of each two phonons forming a Davydov pair.

This compilation has been published in [\[108\]](#).

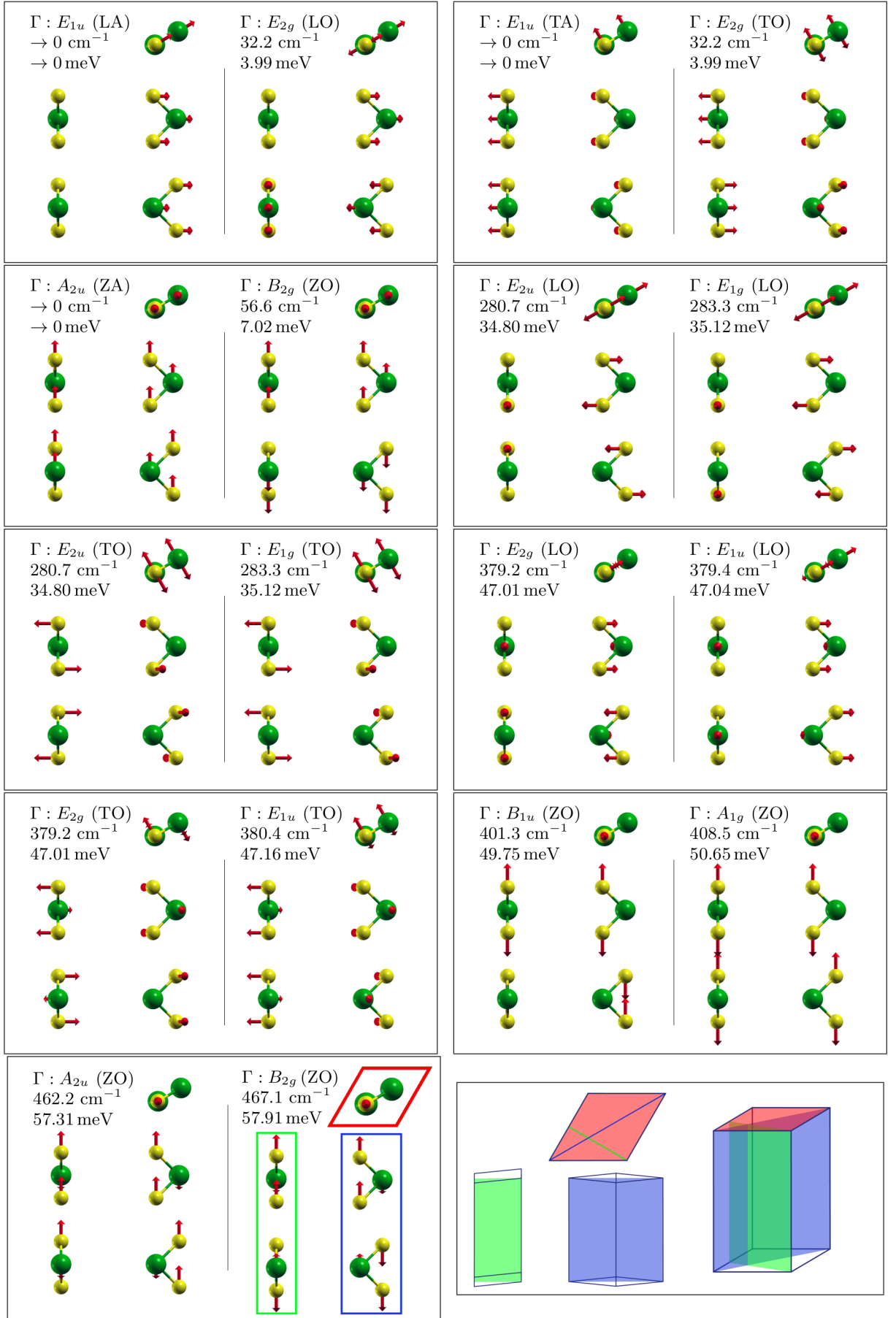


Table A I.: Phonon eigenvectors at the Γ point including the phonon energies of MoS_2 .

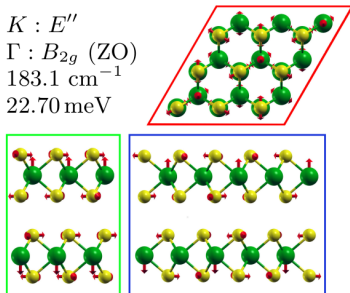
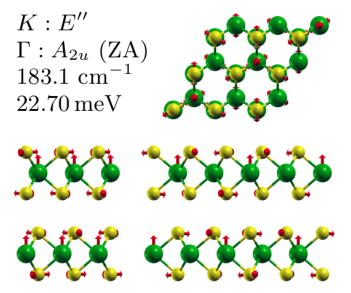
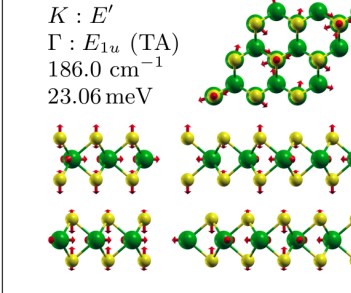
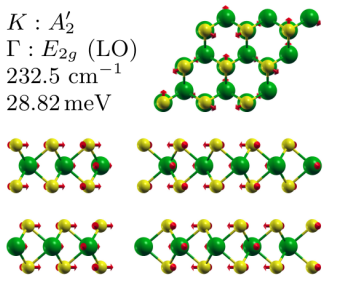
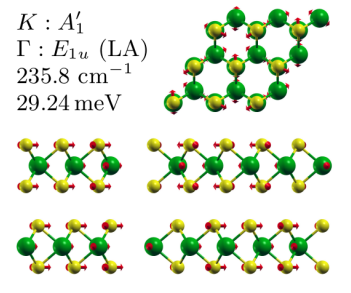
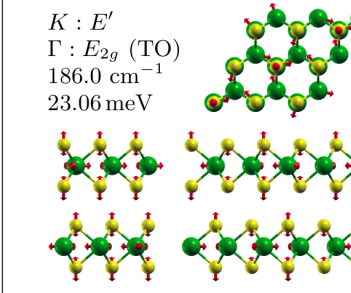
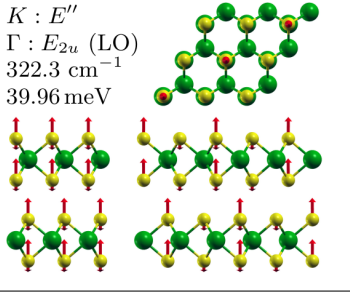
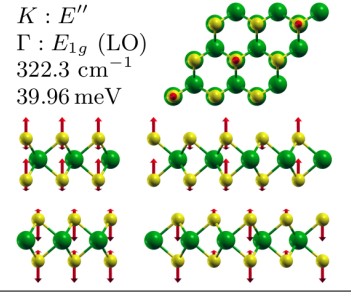
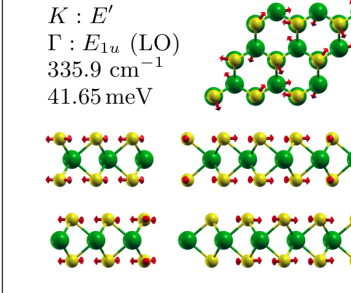
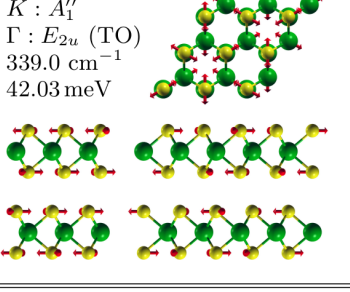
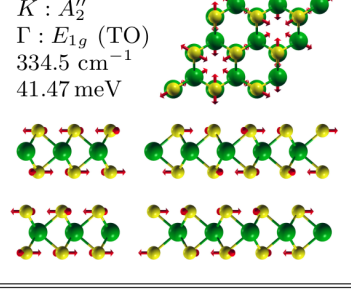
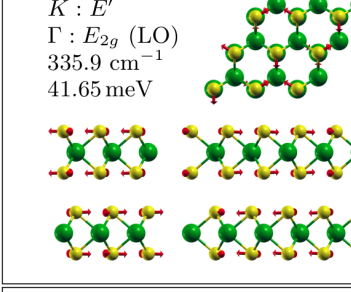
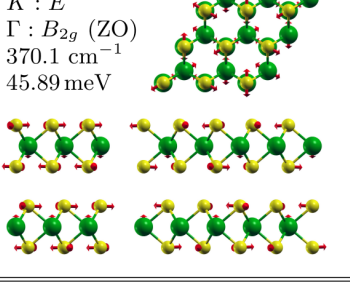
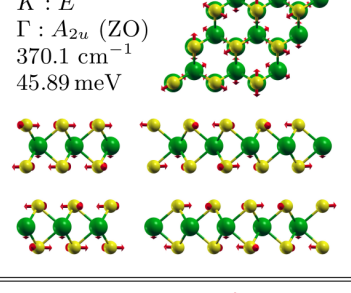
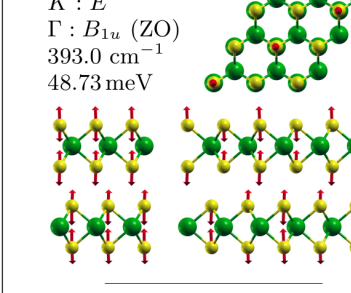
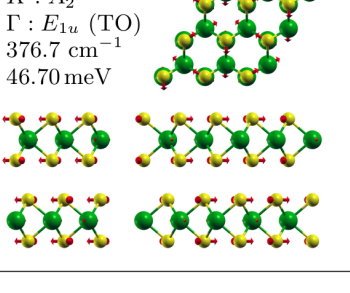
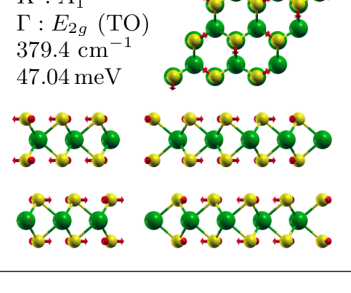
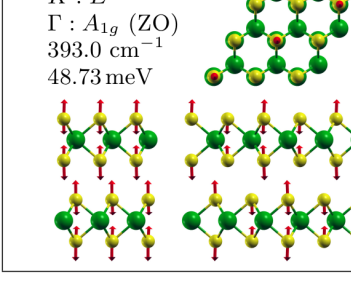
<p>$K : E''$ $\Gamma : B_{2g} \text{ (ZO)}$ 183.1 cm^{-1} 22.70 meV</p> 	<p>$K : E''$ $\Gamma : A_{2u} \text{ (ZA)}$ 183.1 cm^{-1} 22.70 meV</p> 	<p>$K : E'$ $\Gamma : E_{1u} \text{ (TA)}$ 186.0 cm^{-1} 23.06 meV</p> 
<p>$K : A'_2$ $\Gamma : E_{2g} \text{ (LO)}$ 232.5 cm^{-1} 28.82 meV</p> 	<p>$K : A'_1$ $\Gamma : E_{1u} \text{ (LA)}$ 235.8 cm^{-1} 29.24 meV</p> 	<p>$K : E'$ $\Gamma : E_{2g} \text{ (TO)}$ 186.0 cm^{-1} 23.06 meV</p> 
<p>$K : E''$ $\Gamma : E_{2u} \text{ (LO)}$ 322.3 cm^{-1} 39.96 meV</p> 	<p>$K : E''$ $\Gamma : E_{1g} \text{ (LO)}$ 322.3 cm^{-1} 39.96 meV</p> 	<p>$K : E'$ $\Gamma : E_{1u} \text{ (LO)}$ 335.9 cm^{-1} 41.65 meV</p> 
<p>$K : A''_1$ $\Gamma : E_{2u} \text{ (TO)}$ 339.0 cm^{-1} 42.03 meV</p> 	<p>$K : A''_2$ $\Gamma : E_{1g} \text{ (TO)}$ 334.5 cm^{-1} 41.47 meV</p> 	<p>$K : E'$ $\Gamma : E_{2g} \text{ (LO)}$ 335.9 cm^{-1} 41.65 meV</p> 
<p>$K : E''$ $\Gamma : B_{2g} \text{ (ZO)}$ 370.1 cm^{-1} 45.89 meV</p> 	<p>$K : E''$ $\Gamma : A_{2u} \text{ (ZO)}$ 370.1 cm^{-1} 45.89 meV</p> 	<p>$K : E'$ $\Gamma : B_{1u} \text{ (ZO)}$ 393.0 cm^{-1} 48.73 meV</p> 
<p>$K : A'_2$ $\Gamma : E_{1u} \text{ (TO)}$ 376.7 cm^{-1} 46.70 meV</p> 	<p>$K : A'_1$ $\Gamma : E_{2g} \text{ (TO)}$ 379.4 cm^{-1} 47.04 meV</p> 	<p>$K : E'$ $\Gamma : A_{1g} \text{ (ZO)}$ 393.0 cm^{-1} 48.73 meV</p> 

Table A II.: Eigenvectors of the MoS₂ phonons at the K point.

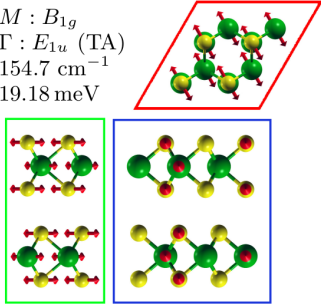
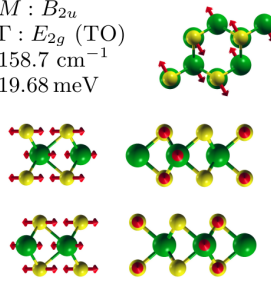
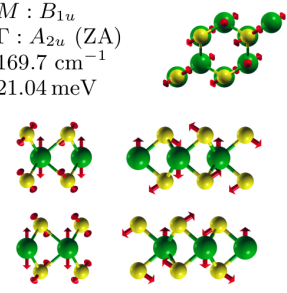
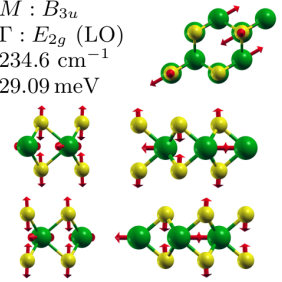
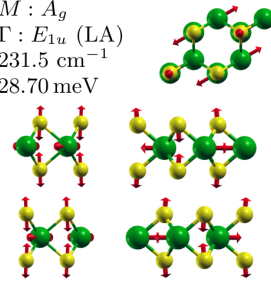
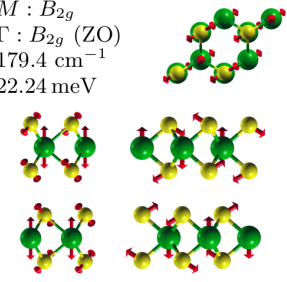
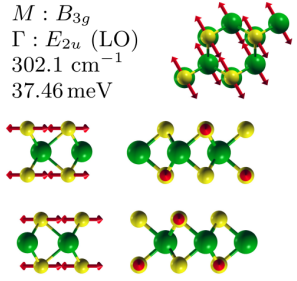
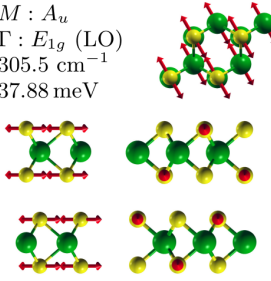
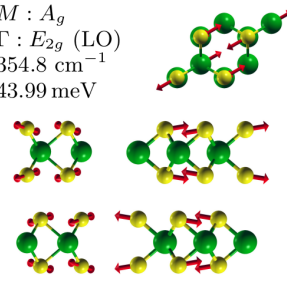
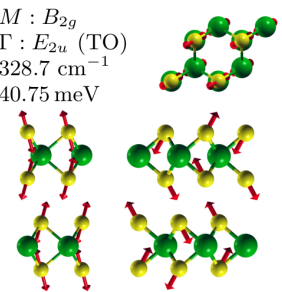
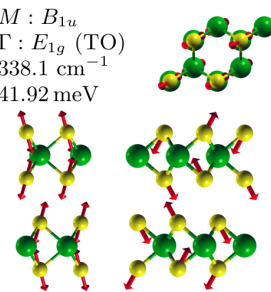
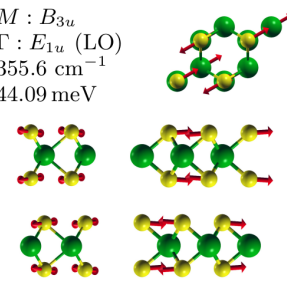
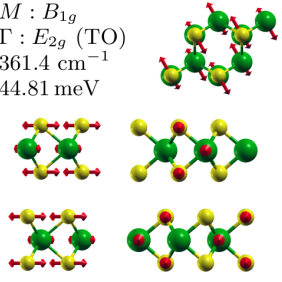
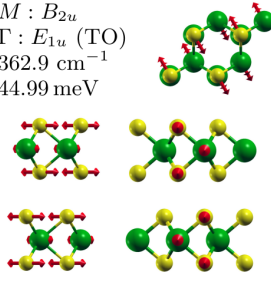
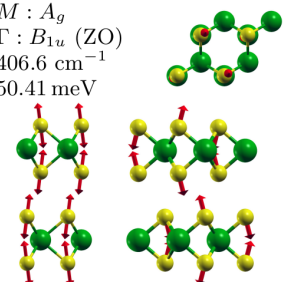
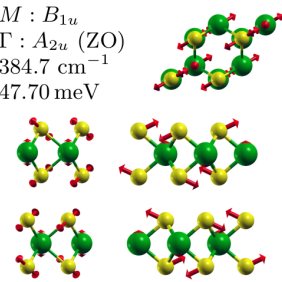
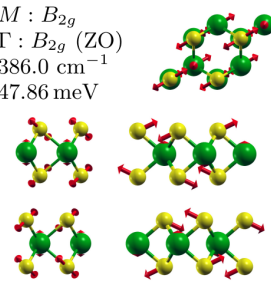
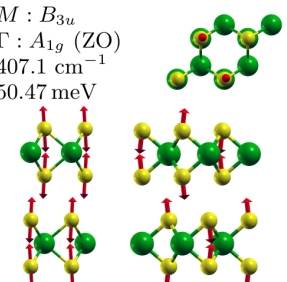
<p> $M : B_{1g}$ $\Gamma : E_{1u} (\text{TA})$ 154.7 cm^{-1} 19.18 meV </p> 	<p> $M : B_{2u}$ $\Gamma : E_{2g} (\text{TO})$ 158.7 cm^{-1} 19.68 meV </p> 	<p> $M : B_{1u}$ $\Gamma : A_{2u} (\text{ZA})$ 169.7 cm^{-1} 21.04 meV </p> 
<p> $M : B_{3u}$ $\Gamma : E_{2g} (\text{LO})$ 234.6 cm^{-1} 29.09 meV </p> 	<p> $M : A_g$ $\Gamma : E_{1u} (\text{LA})$ 231.5 cm^{-1} 28.70 meV </p> 	<p> $M : B_{2g}$ $\Gamma : B_{2g} (\text{ZO})$ 179.4 cm^{-1} 22.24 meV </p> 
<p> $M : B_{3g}$ $\Gamma : E_{2u} (\text{LO})$ 302.1 cm^{-1} 37.46 meV </p> 	<p> $M : A_u$ $\Gamma : E_{1g} (\text{LO})$ 305.5 cm^{-1} 37.88 meV </p> 	<p> $M : A_g$ $\Gamma : E_{2g} (\text{LO})$ 354.8 cm^{-1} 43.99 meV </p> 
<p> $M : B_{2g}$ $\Gamma : E_{2u} (\text{TO})$ 328.7 cm^{-1} 40.75 meV </p> 	<p> $M : B_{1u}$ $\Gamma : E_{1g} (\text{TO})$ 338.1 cm^{-1} 41.92 meV </p> 	<p> $M : B_{3u}$ $\Gamma : E_{1u} (\text{LO})$ 355.6 cm^{-1} 44.09 meV </p> 
<p> $M : B_{1g}$ $\Gamma : E_{2g} (\text{TO})$ 361.4 cm^{-1} 44.81 meV </p> 	<p> $M : B_{2u}$ $\Gamma : E_{1u} (\text{TO})$ 362.9 cm^{-1} 44.99 meV </p> 	<p> $M : A_g$ $\Gamma : B_{1u} (\text{ZO})$ 406.6 cm^{-1} 50.41 meV </p> 
<p> $M : B_{1u}$ $\Gamma : A_{2u} (\text{ZO})$ 384.7 cm^{-1} 47.70 meV </p> 	<p> $M : B_{2g}$ $\Gamma : B_{2g} (\text{ZO})$ 386.0 cm^{-1} 47.86 meV </p> 	<p> $M : B_{3u}$ $\Gamma : A_{1g} (\text{ZO})$ 407.1 cm^{-1} 50.47 meV </p> 

Table A III.: Eigenvectors of the MoS₂ phonons at the M point.

A 3. Python scripts used for IXS data analysis

In the following section the python script used for the IXS data manipulation is given. The script has a detailed in-line documentation, so in this short introduction, only an overview of the general mechanics of the script will be given.¹

The first step approached by the script is to fold the reciprocal space points, where the measurements have been performed into the irreducible part of the first Brillouin zone (BZ), i.e. the triangle formed by the Γ , K and M high symmetry points (section A 3.2, page XXVIII). This is performed in the following steps, which are also depicted in figure A 2. First, the Miller indices ($h k l$) are reduced by their respective off-rounded values, resulting in a data set *close* to the first BZ's center. For l this is sufficient, as all values are now in the interval $l \in [-0.5, 0.5]$. Therefore, all remaining steps will only consider the h and k values.

Second, the data is rotated around C_6 until all points have coordinates with $h > 0$ and $k > 0$. All data points now lie within the diamond shape with its corners at

¹lambda-functions were provided by Sebastian Weigand (Technische Universität Berlin), as well as several tips regarding the regular expression, efficiency and form of the scripts.

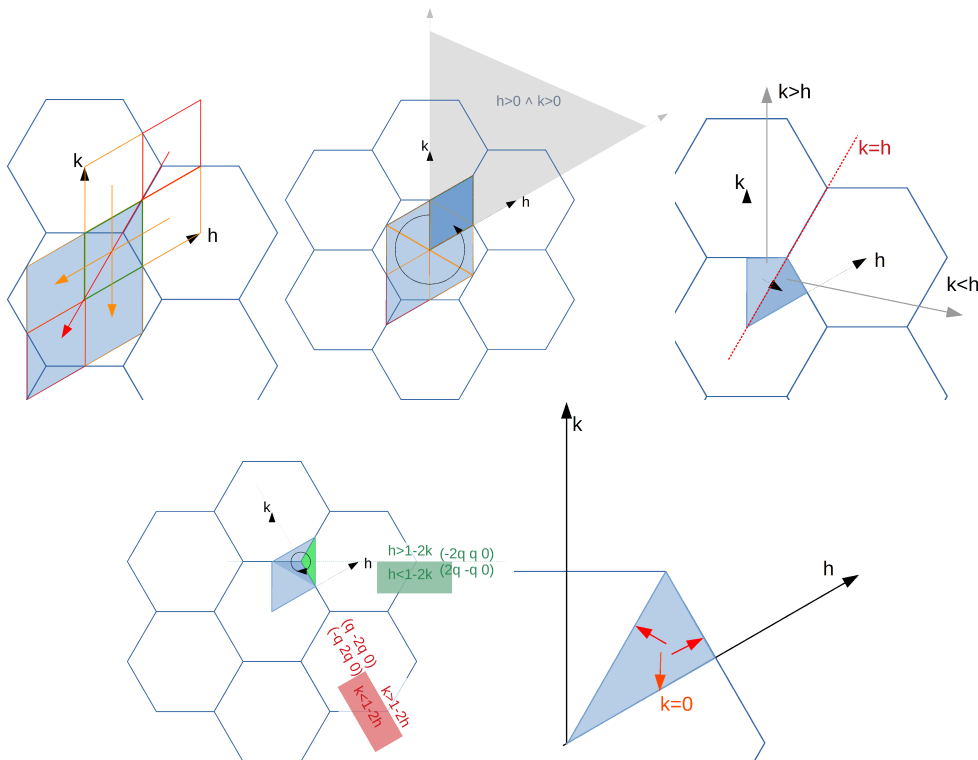


Figure A 2.: Illustrations of the steps followed for the zone folding procedure. See text for detailed description.

A. Appendix

$\Gamma - M - M' - M''$ (with the different M point in the directions $[100]$, $[010]$ and $[110]$).

Third, the data points are flipped into the triangle $\Gamma - M$ ($[110]$ direction) $- M$ ($[100]$ direction), i. e. exploiting the mirror symmetry along $[110]$.

Finally, one C_3 rotation around the K point of all $(h k)$ which are outside of the first BZ, i. e. data with $h > 1 - 2k$ (see Fig. A 2), brings all $(h k)$ into the first BZ. However, half of the area rotated by the C_3 rotation is projected into the *upper* irreducible triangle. A further run of the flip-function (included in the C_3 -rotation function) will mirror them into the *lower* triangle.

The figures shown in the script include all reciprocal space points measured during the beam time to measure the dispersion of WS_2 (cf. section 4.3) Next, the data set can be refined to discard $(h k l)$ not meeting a desired accuracy in l (value can be set in the INPUT-section of the script).

To estimate the error by projecting the data onto the high symmetry lines, the DFT calculated² 2D-dispersion is used (section A 3.3.2, page XXX). Therefore, the calculation file is read and transformed into the same coordinate system as the measurement's $(h k l)$. Afterwards, the phonon energies at the respective points are found and compared to the (calculated) value at the projected point. The calculated difference in energy is plotted for each phonon and projection³ and can be used to discard data from further analysis.

Finally, a table is generated which includes all data, to be used to fill in the experimental data. Furthermore, a list is generated which spectra (i. e. scan number and analyzer) meets the desired accuracy in l and $\Delta\omega$, to better navigate through the large number of spectra.

The next feature of the script is that it reads and splits the FOURC / SPEC file containing all measurement information gathered during the beam time (section A 3.4, page XLIII). This function finds the different information of use for spectral analysis, by exploiting regular expressions to match repeated expressions in the file, such as the scan execution commands or scan numbers. The spectra will be saved in individual files. After the acquisition of the single spectra-files, the spectra will be plotted to identify, e. g., scans containing Stokes-anti-Stokes pairs needed for the calibration. Note that the plots only use the estimated energy of the beamline at this point and are not suited for exact analysis.

²DFT calculations were performed by Roland Gillen (Friedrich-Alexander Universität, Erlangen-Nürnberg).

³Note that the values of the 2D-dispersion used here are not sorted by phonon branches, but by the phonon energy at the respective reciprocal space point for computational reasons. The use of the script with this dispersion to analyze the applicability of the projection of values all over the BZ onto the high symmetry lines is therefore uncertain. However, the use of a very low acceptance value for the error from projection leads to a sufficient small acceptance that only data from the high symmetry lines will be kept for further analysis, even if the comparison of the error was made for a different branch.

The last part of the script (section A 3.6, page XLVI) uses the user-provided offsets-table (which is acquired by fitting the Stokes-anti-Stokes pairs, and Bragg peaks in the raw spectra produced in the last step) to correct each individual spectrum by its respective offset and by the X-ray flux. The corrected spectra are then interpolated and averaged if multiple scans at the same reciprocal space points were acquired.

A second script, converts the table, by now filled with the experimental values, into a plot-friendly format (section A 3.7, page XLVI).

A 3.1. Header: import of libraries and definitions of variables and functions

```
>>> ### IMPORT LIBRARIES
... %matplotlib inline
... import numpy as np
... import pandas as pd
... import matplotlib.pyplot as plt
... from matplotlib.colors import Normalize
... from IPython.display import set_matplotlib_formats
... set_matplotlib_formats('png', 'pdf')
... import math
... from scipy.interpolate import interp1d
... import re
... import os
... from io import StringIO
... import glob
...
... pd.set_option("display.max_columns", 10)
...
... #####

>>> ### INPUTs: Definition of used filepath's and global constants
...
... #####
... ### paths
... # inputs
... hkl_source_file = "input_hkl_meas"
... dispersion_path = "./input_2D-dispersion-IBZ.dat"
... scan_list = 'input_scan-correction-list.txt'
... offset_table = 'input_SAS-offsets.tsv'
... # SPEC files: scan_no_offset need to be set at a larger number than the
... # last scan of the previous file, i.e. ~August has 267 scans
... # -> starting ~October at scan=300
... files = [{"name": "input_WS2_fourc_August", "scan_no_offset": 0 },
...          {"name": "input_WS2_fourc_October", "scan_no_offset": 300}]
```

A. Appendix

```
...
... # outputs
... output_file_name =f"output_pre-selection_of_hkl_to_evaluate-{hkl_source_file}"
... # 'temporary' folder for raw spectra
... raw_spectra = './raw_spectra/'
... # write spectra to
... output_file_path = './corrected_spectra/'
...
...
...
...
... l_tolerance=0.025 # out-of-plane tolerance in reciprocal lattice vector
... ↔ units
... acceptable_frequency_error=0.1 ## in inverse cm!!
... '''
... if "remove_out_of_bounds_vals = True" rows will be discarded, if either of
... the above criteria is not met. However, be aware that a change of
... tolerances will result in a differently shaped table, i.e., transferring
... experimental values from the old to the new table will require a script or
... some tedious work!
... The set tolerance will still be in effect, as q-values for insufficiently
... fitting (hkl) will be removed from the table (see below,
... sec.~\ref{sec:remove-q}).
... '''
... remove_out_of_bounds_vals = False
...
... ## in the order given in the calculated dispersion
... phonon_symmetry_names = [
... "A12u", "E11u", "E21u", "E12g", "E22g", "B12g",
... "E12u", "E22u", "E11g", "E21g", "E32g", "E42g",
... "E31u", "E41u", "B1u", "A1g", "A32u", "B22g"
... ]
...
... directions = ["GK", "GM", "KM"]
...
... #####

>>> ### DEFINITIONS of FUNCTIONS
... #####
...
... ### generate random values --> proof of principle for 'arbitrary'
... # values; fixed seed to have a fixed pattern in multiple runs
... def rand_hkl(spread):
...     np.random.seed(1)
...     random_h = np.random.random(1000)*2*spread-spread
...     np.random.seed(2)
...     random_k = np.random.random(1000)*2*spread-spread
...     np.random.seed(3)
...     random_l = np.random.random(1000)*2*spread-spread
```

A 3. Python scripts used for IXS data analysis

```
...     # write values to data frame
...     hkl = pd.DataFrame({"h": random_h, "k": random_k, "l": random_l})
...     return hkl
...
...     ### transformations
...     # hex --> cart
...     def hex_to_cart_x(h, k):
...         x=h+k/2
...         return x
...
...     def hex_to_cart_y(h, k):
...         y=np.sqrt(3)/2*k
...         return y
...
...     # cart --> hex
...     def cart_to_hex_h(x, y):
...         h = x - y/np.sqrt(3)
...         return h
...
...     def cart_to_hex_k(x, y):
...         k = 2/np.sqrt(3)*y
...         return k
...
...     # measured resistivity to energy of analyzers and main monochromator
...     def resistance_to_energy(R):
...         # calibration curve of Temp sensor
...         c = 0.001130065
...         g = 0.0002405245
...         e = 0.0000001089848
...         f = -266.5
...         Temp_SI = f + (1/ (c+(g*np.log(R) + e*np.log(R)**3)))
...
...     # thermal expansion of Si as function of T with a_Si = a_Si(Temp=22.5°C)
...     T = Temp_SI - 22.5 # + 273.15
...     a_Si = np.sqrt(8) * 1.920157562 # CODATA
...
...     a = 2.581 * 10**(-6) # 1/K
...     b = 0.008 * 10**(-6) # 1/K^2
...     a_T = a_Si * (1 + a * T + b * T**2)
...
...     # corresponding distance change of (999) lattice planes
...     d = a_T / (np.sqrt(3)*9)
...
...     # photon energy: Analyzer and main monochromator temperature to photon
...     # energy conversion (Bragg's law and thermal expansion)
...     h = 6.62606896 # 10**(-34) Js
...     c = 2.99792458 # 10**8 m/s, as defined
...     e = 1.602176487 # 10**(-19) C
...     theta = 89.98 / (2*np.pi)
...     E = (h / e) * c / (2* d * np.sin(theta)) * 10**6
```

A. Appendix

```
...     return E
...
...
...
...     #####
...     ### plotting
...     pointsize = 2
...     a=1/(2*np.sqrt(3)) # 0,288
...     b=1/np.sqrt(3)     # 1,577
...     c=0.5*np.sqrt(3)/2 # 0,433
...
...     def plot(h, k):
...         ax1 = plt.subplot(121)
...         ax1.set_aspect("equal")
...         ax1.set_xlabel('h')
...         ax1.set_ylabel('k')
...         ax1.set_title('in hexagonal coordinates')
...         ax1.plot([0,0.5,1/3,0], # triangle gamma - M - K - gamma
...                 [0,0 ,1/3,0],
...                 [0,1/2,1/2,0 ,0], # first sector: gamma - M - K - M - gamma
...                 [0,0 ,1/2,1/2,0])
...         ax1.scatter(h, k, s=pointsize, zorder=9001)
...
...         x = hex_to_cart_x(h,k)
...         y = hex_to_cart_y(h,k)
...
...         ax2 = plt.subplot(122)
...         ax2.scatter(x, y, s=pointsize, zorder=9001)
...         ax2.set_aspect("equal")
...         ax2.set_xlabel('x')
...         ax2.set_ylabel('y')
...         ax2.yaxis.tick_right()
...         ax2.yaxis.set_label_position("right")
...         xmin, xmax = ax1.get_xlim()
...         ymin, ymax = ax1.get_ylim()
...         ax2.set_xlim(-0.05, xmax)
...         ax2.set_ylim(-0.05, ymax)
...         ax2.set_title('in cartesian coordinates')
...         # six triangles of the hexagon
...         ax2.plot(
...         [0,-1/2,-1/2,0], [0, a,- a,0],
...         [0,1/2,3/4,1/4,0], [0, 0, c,c,0], #first 'sector
...         [0,0,-1/2,0], [0,b, a,0],
...         [0,1/2,1/2,0], [0, -a, a,0],
...         [0,1/2, 0,0], [0, a, b,0],
...         [0,-1/2,0,0], [0,-a,-b,0],
...         [0,0,1/2,0], [0,-b,-a,0])
...         plt.show()
...
...     # plot all using the estimated Energy
```

A 3. Python scripts used for IXS data analysis

```
... def plot_all_Emonot(scan, f): # all analyzers at one (hkl)
...     fig, ax = plt.subplots(1,1)
...     for index in range(1, 10):
...         scan.plot("E_monot", f"deta{index}", ax=ax)
...     plt.text(0.01, 0.9,f, transform=ax.transAxes, fontsize=12)
...
... # plot all using the calculated energy (from resistances)
... def plot_all(scan, f): # all analyzers at one (hkl)
...     fig, ax = plt.subplots(1,1)
...     for index in range(1, 10):
...         energy = resistance_to_energy(scan.Resistance_mono) -
...     ↪ resistance_to_energy(scan[f"Resistance_A{index}"])
...         plt.plot(energy, scan[f"deta{index}"])
...     plt.text(0.01, 0.9, f, transform=ax.transAxes, fontsize=12)
...
... #####
... ### zone-folding
... #####
... # rotation of data into the 1. sector (0 =< phi < 60)
... def rotation_6(h,k):
... # hex --> cart + folding into the 1. quadrant:
...     # abs(x): reflect points on sigma_d -> right half space (x>0)
...     x=abs(hex_to_cart_x(h, k))
...     # abs(y): reflect points on sigma_v -> upper half space (y>0)
...     y=abs(hex_to_cart_y(h, k))
... # calculating angle
...     r=np.sqrt(x**2 + y**2)
...     phi=np.arccos(x/r)
...     phi[np.isnan(phi)] = 0 # intercept nan's as a consequence of r=0
...
...     sector=np.floor(phi/(np.pi/3)) # In which sector is the point?
...     # How far to rotate to rotate into 1. sector?
...     rot_phi = -(np.pi/3)*sector
... # rotate!
...     x_neu=x*np.cos(rot_phi)-y*np.sin(rot_phi)
...     y_neu=(x*np.sin(rot_phi)+y*np.cos(rot_phi))
... # cart --> hex
...     h_rot = cart_to_hex_h(x_neu, y_neu)
...     k_rot = cart_to_hex_k(x_neu, y_neu)
... # write values to data frame
...     df = pd.DataFrame({"h": h, "k": k, "h_rot":h_rot, "k_rot":k_rot,
...     ↪ "phi":phi, "rot_phi":rot_phi, "x_neu": x_neu, "y_neu": y_neu,})
...     return df
...
... #####
... # flip the 'upper' irreducible triangle of the 1. sector into the 'lower'
... # by reflection on the bisecting line (h h 0) = Gamma - K direction
... def flip(h, k):
... # is the data point in the 'upper'?
...     h_smaller_k = h<k
```

A. Appendix

```
... # initialize return variables
...     h_flip, k_flip = h, k
... # replace all point where TRUE with reversed h and k
...     h_flip.values[h_smaller_k] , k_flip.values[h_smaller_k] =
...     ↪ k[h_smaller_k], h[h_smaller_k]
...     return h_flip, k_flip
...
... #####
... # C3-rotation around K-point (1/3 1/3 0)
... def rotation_3(h_flip,k_flip):
... # is the point located out of the 1.BZ? -> TRUE/FALSE
... # !! only considers the 'lower' irreducible triangle
... # --> data needs to be flipped beforehand
... #         or rotation_3 needs to be run twice on the dataset
...     out_of_BZ = (h_flip>1/3) & (k_flip>(1-2*h_flip))
... # project K-point onto the origin: K -> (0 0 0)
...     h_0=h_flip[out_of_BZ] - 1/3
...     k_0=k_flip[out_of_BZ] - 1/3
... # hex -> cart:
...     x=hex_to_cart_x(h_0, k_0)
...     y=hex_to_cart_y(h_0, k_0)
... # rotate by -120° if out_of_BZ == TRUE!
...     x_neu=x*np.cos(-2*np.pi/3)-y*np.sin(-2*np.pi/3)
...     y_neu=x*np.sin(-2*np.pi/3)+y*np.cos(-2*np.pi/3)
... # cart --> hex
...     h_rot = cart_to_hex_h(x_neu, y_neu)
...     k_rot = cart_to_hex_k(x_neu, y_neu)
... # projection of the K-point back to (1/2 1/3 0)
...     h_rot3=h_rot + 1/3
...     k_rot3=k_rot + 1/3
... # initialize return variable with input values
...     h_1BZ, k_1BZ = h_flip, k_flip
... # rotation brings points into the 'upper' irreducible triangle
... # --> flip those down and write into return variable
...     h_1BZ.values[out_of_BZ], k_1BZ.values[out_of_BZ]=flip(h_rot3,k_rot3)
...     return h_1BZ, k_1BZ
...
... #####
... ### error-plot
... def plot_error_heatmap(error_df):
...     direction = error_df.name
...     scaling_min = error_df[list(phonon_symmetry_names)].min().min()
...     scaling_max = error_df[list(phonon_symmetry_names)].max().max()
...     # used data -> colored, discarded -> grey
...     a=acceptable_frequency_error
...     for i in phonon_symmetry_names:
...         norm = Normalize(vmin=-a, vmax=a)
...         data_vals = error_df[i].copy().values
...         data_vals[data_vals < -a] = a+1
...         sc = plt.scatter(error_df.x_IBZ, error_df.y_IBZ, c=data_vals,
```

A 3. Python scripts used for IXS data analysis

```
... ↪ norm=norm, cmap=plt.cm.nipy_spectral)
...     plt.colorbar(sc)
...     plt.title( f"{direction}-projection phonon {i}")
...     plt.show()
...
... #####
... ### search routine
... # P: measured (hkl) (tuple: (h,k)) which should be found
... # in dispersion D (tuple: two columns)
... def find_closest_index(P,D):
...     norm = (P[0] - D[0])**2 + (P[1] - D[1])**2
...     closest_index = norm.idxmin()
...     return closest_index
...
... #####
... ### rearrange data: separate rows for diff phonons,
... ### for all analyzers & scans
... def re_arange_data(input_df, input_calc, keep_cols, transpose_cols,
... ↪ direction):
...     keep_cols = [*keep_cols, f"q_{direction}"]
...     result_df = pd.DataFrame()
...     for index, row in input_df.iterrows():
...         initial_df = pd.DataFrame([row]*len(transpose_cols))[keep_cols]
...         initial_df["Phonon"] = transpose_cols
...         initial_df["error" + direction] = row[transpose_cols].values
...         initial_df["calc_energy_hkl"] = input_calc.loc[index,
... ↪ transpose_cols].values/8.06554
...         if result_df.empty:
...             result_df = initial_df
...         else:
...             result_df = result_df.append(initial_df, ignore_index=True)
...     return result_df.reset_index(drop=True)
...
... #####
... ### read and split fourc file
... def read_and_split_FOURC(data_file_name, scan_number_offset):
...     with open(data_file_name) as data_file:
...         file_data = data_file.read()
...
...     # Regular expression to find scans
...     measurement_regex = re.compile("#S
... ↪ (?P<scan_nr>\d+)\s*(ascan|)\s*(?P<scan_type>\w+).*?#L
... ↪ (?P<header>.*?)\n(?:P<data>.*?)(\n\s*\n|#C)", re.M | re.S)
...
...     # for each match of the RegEx, define scan_nr, etc
...     for match in re.finditer(measurement_regex, file_data):
...         scan_nr = str(int(match.group("scan_nr")) + scan_number_offset)
...         scan_type = match.group("scan_type")
...         header = match.group("header")
...         columns = re.split("\s{2}", header)
```

A. Appendix

```
...     #correct single/double-spaces issue from fourc
...     for index, value in enumerate(columns):
...         columns[index] = value.replace(" ", "_")
...         data = match.group("data")
...
...     # create df with "data" for each scan and "header" as coulumn names
...     df = pd.read_csv(StringIO(data), sep="\s+", header=None,
... ↪ names=columns)
...
...     df.rename(columns={'prem_ad5': 'Resistance_mono',
...                        'prem_ad6': 'Resistance_A1',
...                        'prem_ad7': 'Resistance_A2',
...                        'prem_ad8': 'Resistance_A3',
...                        'prem_ad9': 'Resistance_A4',
...                        'prem_ad10': 'Resistance_A5',
...                        'prema_ad13': 'Resistance_A6',
...                        'prem_ad12': 'Resistance_A7',
...                        'prema_ad14': 'Resistance_A8',
...                        'prem_ad15': 'Resistance_A9',
...                        },
...                inplace=True)
...
...     # write to file, with scan number (3 digit) and scan type
...     filename =
... ↪ f"{raw_spectra}/scan_nr_{scan_nr.zfill(3)}_{scan_type}.tsv"
...     df.to_csv(filename, sep="\t", index=False)
...
...     # generation of simple, uncorrected, xy-style spectra for
...     # Stokes-anti-Stokes shift determination
...     for index in range(1, 10):
...         df_spectra=pd.DataFrame()
...         df_spectra[f"d_Resistance_{index}"] = df["Resistance_mono"] -
... ↪ df[f"Resistance_A{index}"]
...         df_spectra[f"deta{index}"] = df[f"deta{index}"] / df["ione"]
...         spec_filename = f"{raw_spectra}/for-offset-
... ↪ fitting/spectrum_nr_{scan_nr.zfill(3)}_{scan_type}_{index}.txt"
...         df_spectra.to_csv(spec_filename, sep=" ", index=False,
... ↪ header=False)
...
...     #####
...     ### interpolation and correction function
...     # will be called for each (hkl), and each analyzer seperately
...     def interpolate_and_correct(scans_row, offsets_df, analyzer):
...         # find relevant scan(s)/offsets in a row, ie discard NaN's
...         not_nan_scans = scans_row[scans_row != "nan"]
...         offsets = offsets_df.loc[not_nan_scans, f"A{analyzer}"]
...
...         # initialize
...         interpol_funcs = []
```

A 3. Python scripts used for IXS data analysis

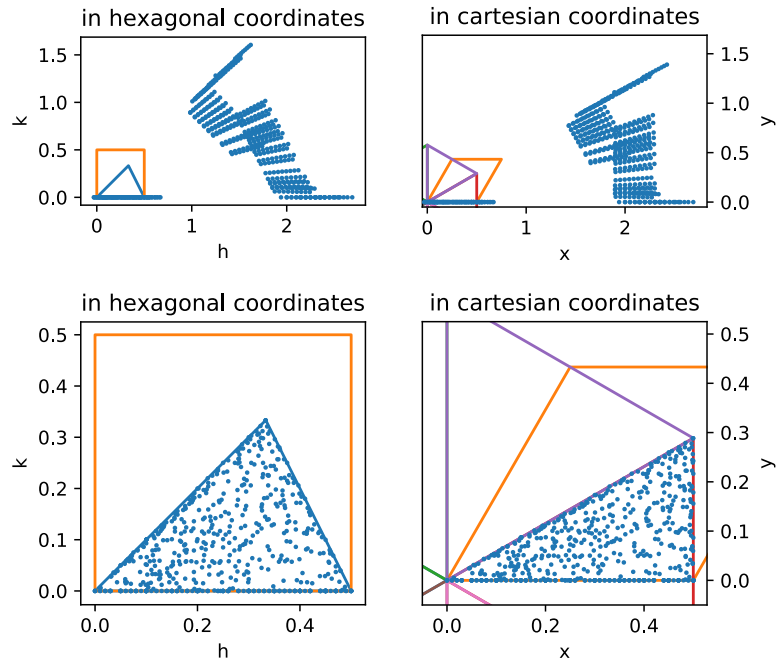
```
...     shared_min = np.nan
...     shared_max = np.nan
...     sample_len = 0
...     # for each scan at (hkl) on analyzer
...     for scan_nr, offset in zip(not_nan_scans, offsets):
... #         print(f"scannr: {scan_nr}, offsets: {offsets[scan_nr]}")
...         # read spectrum
...         scan = pd.read_csv(f'{raw_spectra}scan_nr_{scan_nr}_monot.tsv',
↪     sep="\s+")
...         x =resistance_to_energy(scan["Resistance_mono"]) -
↪     resistance_to_energy(scan[f"Resistance_A{analyzer}"] + offsets[scan_nr])
...         y = scan[f"deta{analyzer}"]/scan.ione
...         # define interpolation function and add to df
...         interpol_func = interp1d(x, y, kind='nearest')
...         interpol_funcs.append(interpol_func)
...         # find minimal overlap of all scans to be interpolated on (hkl)
...         x_min = np.min(x)
...         x_max = np.max(x)
...         if np.isnan(shared_min):
...             shared_min = x_min
...         elif shared_min < x_min:
...             shared_min = x_min
...         if np.isnan(shared_max):
...             shared_max = x_max
...         elif shared_max > x_max:
...             shared_max = x_max
...         # set number of interpolation points to
...         sample_len = len(x)
...         # calculate new x-values
...         x_new = np.linspace(shared_min, shared_max, num=sample_len,
↪     endpoint=True)
...         # apply interpolation
...         results = list(map(lambda interpol_func: interpol_func(x_new),
↪     interpol_funcs))
...         average = np.mean(results, axis=0)
...         # write df to export and set file name
...         out_nrs = "_".join(not_nan_scans)
...         interpol = pd.DataFrame({f"E_{out_nrs}_A{analyzer}": x_new,
↪     f"scan_{out_nrs}_A{analyzer}": average})
...         file_name = f"{output_file_path}{out_nrs}_A{analyzer}_corr.txt"
...
...     return interpol, file_name
```

A 3.2. Folding of actual, measured (hkl) into one irreducible part of the 1. BZ

```

>>> # create DataFrame to collect coordinates
... coordinates = pd.DataFrame()
...
... # read values from file
... coordinates = hkl = pd.read_csv(hkl_source_file+".txt", sep="\s+")
... hkl = pd.DataFrame({"h": hkl.h, "k": hkl.k, "l": hkl.l})
... coordinates = pd.DataFrame({"scan_no": coordinates.scan, "Analyzer":
...   ↪ coordinates.Analyzer, "h": coordinates.h, "k": coordinates.k, "l":
...   ↪ coordinates.l})
...
... ## For a proof of concept the following line can be
... ## uncommented, which will result applying the transformations
... ## on uniform distribution hkl random values
... # hkl = rand_hkl(10)
...
... # plot original data
... plot(hkl.h, hkl.k)
...
... # subtract 'nearest' reciprocal lattice vector
... hkl_round = hkl-hkl.round()
...
... # rotate points by n*60° into the first sector
... df = rotation_6(hkl_round.h, hkl_round.k)
...
... # flip values below the bisecting line (Gamma - K)
... df["h_flip"], df["k_flip"]=flip(df.h_rot,df.k_rot)
...
... # rotate points by -120° around the M-point
... # !! only considers the 'lower' irreducible triangle
... # --> data needs to be flipped beforehand
... # or rotation_3 needs to be run twice on the dataset
... coordinates["h_IBZ"], coordinates["k_IBZ"]= rotation_3(df.h_flip,
...   ↪ df.k_flip)
... coordinates["l_IBZ"] = hkl_round.l
...
... # also add the cartesian coordinates to the data frame
... coordinates["x_IBZ"] = hex_to_cart_x(coordinates["h_IBZ"],
...   ↪ coordinates["k_IBZ"])
... coordinates["y_IBZ"] = hex_to_cart_y(coordinates["h_IBZ"],
...   ↪ coordinates["k_IBZ"])
...
... plot(coordinates["h_IBZ"], coordinates["k_IBZ"])
...
... ## write data to file
... # coordinates.to_csv("IBZ-coords_of_" + file + ".csv", index=False)
... coordinates.head()

```



scan_no	Analyzer	h	k	l	h_IBZ	k_IBZ	l_IBZ	x_IBZ	y_IBZ	
0	64,84	A1	2.15	0.0	0.12	0.15	0.0	0.12	0.15	0.0
1	64,84	A6	2.20	0.0	0.07	0.20	0.0	0.07	0.20	0.0
2	64,84	A2	2.25	0.0	0.00	0.25	0.0	0.00	0.25	0.0
3	64,84	A7	2.30	0.0	-0.07	0.30	0.0	-0.07	0.30	0.0
4	84	A3	2.35	0.0	-0.14	0.35	0.0	-0.14	0.35	0.0

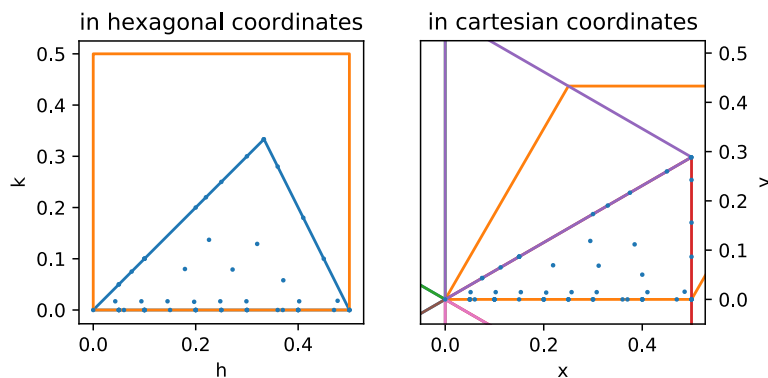
A 3.3. Evaluation of error from projection onto high-symmetry directions

A 3.3.1. Refine data set to neglect measurements with too large l-coordinate

Keeping a full set will allow to alter tolerances afterwards, without the need of reorganizing rows in the results-table.

A. Appendix

```
>>> in_bounds_l = pd.DataFrame()
... in_bounds_l["in_bounds_l"] = abs(coordinates.l_IBZ)<l_tolerance
...
... # 'remove' all sets that do not meet l=0 sufficiently
... hkl_to_check = coordinates[in_bounds_l.in_bounds_l]
... # plot refined data set
... plot(hkl_to_check.h_IBZ, hkl_to_check.k_IBZ)
... print("evaluating " + str(len(hkl_to_check))
...       + " spectra (in l-tolerance), neglecting "
...       + str(len(df)-len(hkl_to_check)) +
...       " spectra (out of l-tolerance)")
...
... if remove_out_of_bounds_vals:
...     # keep refined data set above
...     print("Data with insufficient accuracy has been removed!")
... else:
...     # restore all
...     hkl_to_check = coordinates
...     print("Data with insufficient accuracy is retained in the dataframe!")
```



evaluating 63 spectra (in l-tolerance), neglecting 531 spectra (out of l-tolerance)
Data with insufficient accuracy is retained in the dataframe!

A 3.3.2. Read DFT calculated dispersion from file

```
>>> # read calculated dispersion from file + transform into above used basis
... dispersion_from_file = pd.read_csv(dispersion_path, sep="\s+", header=None,
...   ↪ names=["x", "y", *phonon_symmetry_names])
...
... 
```

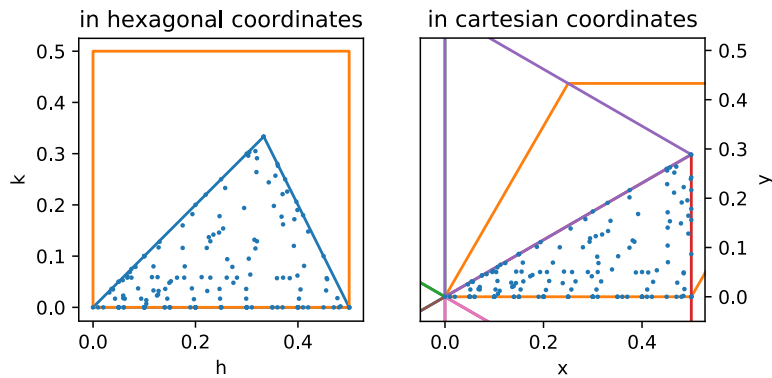
XXX

A 3. Python scripts used for IXS data analysis

```

... # df for dispersion (with same data) in new coordinates
... dispersion = pd.DataFrame(dispersion_from_file.copy().values,
... ↪ columns=['x_sim', 'y_sim', *phonon_symmetry_names])
...
... # convert dispersion into the basis of the measured (hkl)
... # 3.16=a_DFT-D3
... # exchange axes --> M is in x-direction
... dispersion.x_sim=dispersion_from_file.y/(2/(np.sqrt(3)*3.162599642))
... dispersion.y_sim=dispersion_from_file.x/(2/(np.sqrt(3)*3.162599642))
...
... h_sim = cart_to_hex_h(dispersion.x_sim, dispersion.y_sim)
... k_sim = cart_to_hex_k(dispersion.x_sim, dispersion.y_sim)
... plot(h_sim,k_sim)
...
... dispersion.head()

```



	x_sim	y_sim	A12u	E11u	E21u	...	E41u	B1u	\
0	0.000000	0.0	-0.0000	0.0000	0.0000	...	349.8582	410.7828	
1	0.010000	0.0	2.6651	4.4043	6.3868	...	349.8549	410.7502	
2	0.019999	0.0	5.2904	8.8079	12.7872	...	349.8449	410.6542	
3	0.029999	0.0	7.8435	13.2092	19.2124	...	349.8287	410.4996	
4	0.039999	0.0	10.3060	17.6038	25.6699	...	349.8069	410.2939	

	A1g	A32u	B22g
0	417.7075	430.1785	435.3697
1	417.6877	430.0977	435.2881
2	417.6289	429.8560	435.0437
3	417.5330	429.4552	434.6376
4	417.4024	428.8985	434.0715

[5 rows x 20 columns]

A 3.3.3. Find calculated frequencies for measured (hkl)

```
>>> # find closest index and add it in an addtl column to the df
... hkl_to_check = hkl_to_check.assign(closest_index=hkl_to_check.apply(lambda
...   ↪ row: find_closest_index((row["x_IBZ"], row["y_IBZ"]), (dispersion.x_sim,
...   ↪ dispersion.y_sim)), axis=1))
...
... # use found index to create new df with columns
... # x, y, index, and the frequencies of all branches at (x, y)
... frequencies_hkl = pd.DataFrame(hkl_to_check[["x_IBZ", "y_IBZ"]])
... frequencies_hkl["closest_index"] = hkl_to_check["closest_index"]
... frequencies_hkl[dispersion.columns] = frequencies_hkl.apply(lambda row:
...   ↪ dispersion.iloc[int(row["closest_index"])], axis=1)
...
... frequencies_hkl.head()
```

	x_IBZ	y_IBZ	closest_index	x_sim	y_sim	...	E41u	B1u	\
0	0.15	0.0	15	0.150001	0.0	...	349.9633	407.0013	
1	0.20	0.0	20	0.199999	0.0	...	350.6684	403.0078	
2	0.25	0.0	25	0.250001	0.0	...	352.7736	390.8843	
3	0.30	0.0	30	0.299999	0.0	...	356.3286	379.2486	
4	0.35	0.0	35	0.350000	0.0	...	360.5876	370.6068	

	A1g	A32u	B22g
0	413.9219	414.1729	418.4736
1	405.7073	407.2766	412.3837
2	394.9349	404.6402	411.0450
3	382.4733	403.6529	409.5276
4	371.4683	402.8530	407.6985

[5 rows x 23 columns]

A 3.3.4. Projection onto high symmetry lines (in cartesian coordinates)

```
>>> #initialize df's
... projected_GM = pd.DataFrame()
... projected_GK = pd.DataFrame()
... projected_KM = pd.DataFrame()
... frequencies_projected_GM = pd.DataFrame()
... frequencies_projected_GK = pd.DataFrame()
... frequencies_projected_KM = pd.DataFrame()
...
... # get coordinates to project onto the Gamma-M direction
... projected_GM["x_IBZ"], projected_GM["y_IBZ"] = frequencies_hkl["x_IBZ"],
...   ↪ frequencies_hkl["y_IBZ"]
...
... 
```

A 3. Python scripts used for IXS data analysis

```
... # projection onto the Gamma-M line, by dropping the y value
... projected_GM["x_GM"]=projected_GM["x_IBZ"]
... projected_GM["y_GM"]=0
... ## find hkl in calculation
... projected_GM["closest_index"] = projected_GM.apply(lambda row:
... ↪ find_closest_index((row["x_GM"], row["y_GM"]), (dispersion.x_sim,
... ↪ dispersion.y_sim)), axis=1)
... # use found index to create new df with columns
... # x, y, index, and the frequencies of all branches at (x, y)
... frequencies_projected_GM = pd.DataFrame(projected_GM[["x_IBZ", "y_IBZ",
... ↪ "x_GM", "y_GM", "closest_index"]])
... frequencies_projected_GM[dispersion.columns] =
... ↪ frequencies_projected_GM.apply(lambda row:
... ↪ dispersion.iloc[int(row["closest_index"])], axis=1)
...
...
... # # Gamma-K direction
... # projection onto the Gamma-K line, by multiplying
... # with the respective unitvector in cartesian coords
... K_x=hex_to_cart_x(1/3,1/3)
... K_y=hex_to_cart_y(1/3,1/3)
... rr=np.sqrt(K_x**2+K_y**2) # radius
... K_x_norm=K_x/rr # normalizing
... K_y_norm=K_y/rr # normalizing
...
...
... projected_GK["x_IBZ"], projected_GK["y_IBZ"] = frequencies_hkl["x_IBZ"],
... ↪ frequencies_hkl["y_IBZ"] # get coordinates
... projected_GK["x_GK"] = (K_x_norm*projected_GK.x_IBZ + K_y_norm*
... ↪ projected_GK.y_IBZ) * K_x_norm
... projected_GK["y_GK"] = (K_x_norm*projected_GK.x_IBZ + K_y_norm*
... ↪ projected_GK.y_IBZ) * K_y_norm
...
... frequencies_projected_GK["h_GK"], frequencies_projected_GK["k_GK"] =
... ↪ cart_to_hex_h(projected_GK.x_GK, projected_GK.y_GK),
... ↪ cart_to_hex_k(projected_GK.x_GK, projected_GK.y_GK)
...
... # find hkl in calculation
... projected_GK["closest_index"] = projected_GK.apply(lambda row:
... ↪ find_closest_index((row["x_GK"], row["y_GK"]), (dispersion.x_sim,
... ↪ dispersion.y_sim)), axis=1)
... # use found index to create new df with columns x, y, index,
... # and the frequencies of all branches at (x, y)
... frequencies_projected_GK = pd.DataFrame(projected_GK[["x_IBZ", "y_IBZ",
... ↪ "x_GK", "y_GK", "closest_index"]])
... frequencies_projected_GK[dispersion.columns] =
... ↪ frequencies_projected_GK.apply(lambda row:
... ↪ dispersion.iloc[int(row["closest_index"])], axis=1)
...
...
...

```

A. Appendix

```
... # # K-M direction
... # scalar product with (-1 2 0) to project onto the line through (000)
... # parallel to K-M direction
... # adding 0.5 to the x-value pushes the projected values onto KM-direction
... KM_x=hex_to_cart_x(-1,2)
... KM_y=hex_to_cart_y(-1,2)
... rr=np.sqrt(KM_x**2+KM_y**2) # radius
... KM_x_norm=KM_x/rr # normalizing
... KM_y_norm=KM_y/rr # normalizing
...
... projected_KM["x_IBZ"], projected_KM["y_IBZ"] = frequencies_hkl["x_IBZ"],
... ↪ frequencies_hkl["y_IBZ"] # get coordinates
... projected_KM["x_KM"] = (KM_x_norm*projected_KM.x_IBZ +
... ↪ KM_y_norm*projected_KM.y_IBZ)*KM_x_norm + 0.5
... projected_KM["y_KM"] = (KM_x_norm*projected_KM.x_IBZ +
... ↪ KM_y_norm*projected_KM.y_IBZ)*KM_y_norm
... frequencies_projected_KM["h_KM"], frequencies_projected_KM["k_KM"] =
... ↪ cart_to_hex_h(projected_KM.x_KM, projected_KM.y_KM),
... ↪ cart_to_hex_k(projected_KM.x_KM, projected_KM.y_KM)
...
... # find hkl in calculation
... projected_KM["closest_index"] = projected_KM.apply(lambda row:
... ↪ find_closest_index((row["x_KM"], row["y_KM"]), (dispersion.x_sim,
... ↪ dispersion.y_sim)), axis=1)
... # use found index to create new df with columns x, y, index,
... # and the frequencies of all branches at (x, y)
... frequencies_projected_KM = pd.DataFrame(projected_KM[["x_IBZ", "y_IBZ",
... ↪ "x_KM", "y_KM", "closest_index"]])
... frequencies_projected_KM[dispersion.columns] =
... ↪ frequencies_projected_KM.apply(lambda row:
... ↪ dispersion.iloc[int(row["closest_index"])], axis=1)
```

A 3.3.5. Calculate a 'q'-axis (abscissa) for later plotting along Γ -K-M- Γ :

$$0 = \Gamma = 1 + 1/\sqrt{3}, K = 2/3, M = 1$$

```
>>> # Gamma-K:
... q_GK = 2*cart_to_hex_h(projected_GK.x_GK, projected_GK.y_GK)
...
... # Gamma-M: q('second' gamma point) - q(GM)
... q_GM = 1+1/np.sqrt(3) - 2/np.sqrt(3) * cart_to_hex_h(projected_GM.x_GM,
... ↪ projected_GM.y_GM)
...
... # K-M: M to K from 1 to 2/3
... q_KM = 1-projected_KM.y_KM*2/np.sqrt(3)
...
... q_projected = pd.DataFrame()
... q_projected["q_GK"] = q_GK
```

```
... q_projected["q_GM"] = q_GM
... q_projected["q_KM"] = q_KM
```

A 3.3.6. Calculate error for projected data onto high-symmetry line

Calculate error for projected data onto high-symmetry line by evaluating the difference in the (calculated) phonon energy from the projected and measured (hkl).

```
>>> error_GK=frequencies_hkl-frequencies_projected_GK
... #restore x and y coordinates & drop irrelevant columns
... error_GK.x_IBZ=frequencies_hkl.x_IBZ
... error_GK.y_IBZ=frequencies_hkl.y_IBZ
... error_GK = error_GK.drop(["closest_index", "x_GK", "y_GK", "x_sim",
... ↪ "y_sim"], axis=1)
... error_GK.name="GK"
...
... error_GM=frequencies_hkl-frequencies_projected_GM
... #restore x and y coordinates
... error_GM.x_IBZ=frequencies_hkl.x_IBZ
... error_GM.y_IBZ=frequencies_hkl.y_IBZ
... error_GM = error_GM.drop(["closest_index", "x_GM", "y_GM", "x_sim",
... ↪ "y_sim"], axis=1)
... error_GM.name="GM"
...
... error_KM=frequencies_hkl-frequencies_projected_KM
... #restore x and y coordinates, drop other non-sense columns
... error_KM.x_IBZ=frequencies_hkl.x_IBZ
... error_KM.y_IBZ=frequencies_hkl.y_IBZ
... error_KM = error_KM.drop(["closest_index", "x_KM", "y_KM", "x_sim",
... ↪ "y_sim"], axis=1)
... error_KM.name="KM"
...
... error_GK.head()
```

	A12u	A1g	A32u	B12g	B1u	...	E32g	E41u	E42g	\
0	9.7141	-1.3067	-4.0516	13.3197	-0.7096	...	-0.4750	-0.0343	-0.4277	
1	12.9793	-3.3784	-6.2349	15.1047	-3.3447	...	-0.7566	0.3681	-0.6332	
2	12.5267	-7.5797	-0.3062	15.2788	-7.4113	...	-1.2884	1.8114	-1.1290	
3	13.3254	-8.3259	0.1616	14.6088	-7.6239	...	-1.2795	4.0386	-1.7064	
4	17.8271	-10.5743	0.5951	15.9572	-8.0595	...	1.6760	7.1461	6.2199	

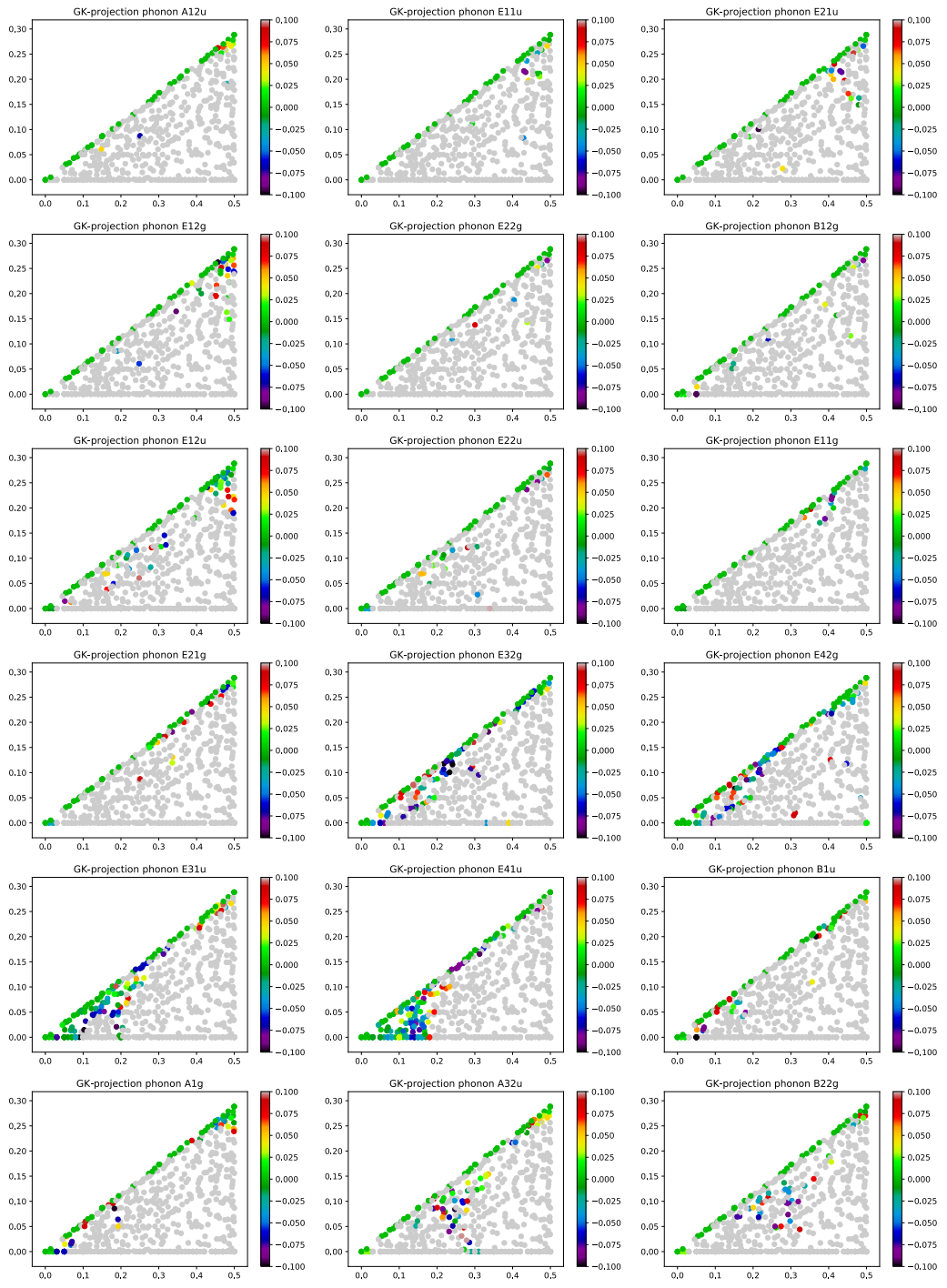
	x_IBZ	y_IBZ
0	0.15	0.0
1	0.20	0.0
2	0.25	0.0
3	0.30	0.0
4	0.35	0.0

[5 rows x 20 columns]

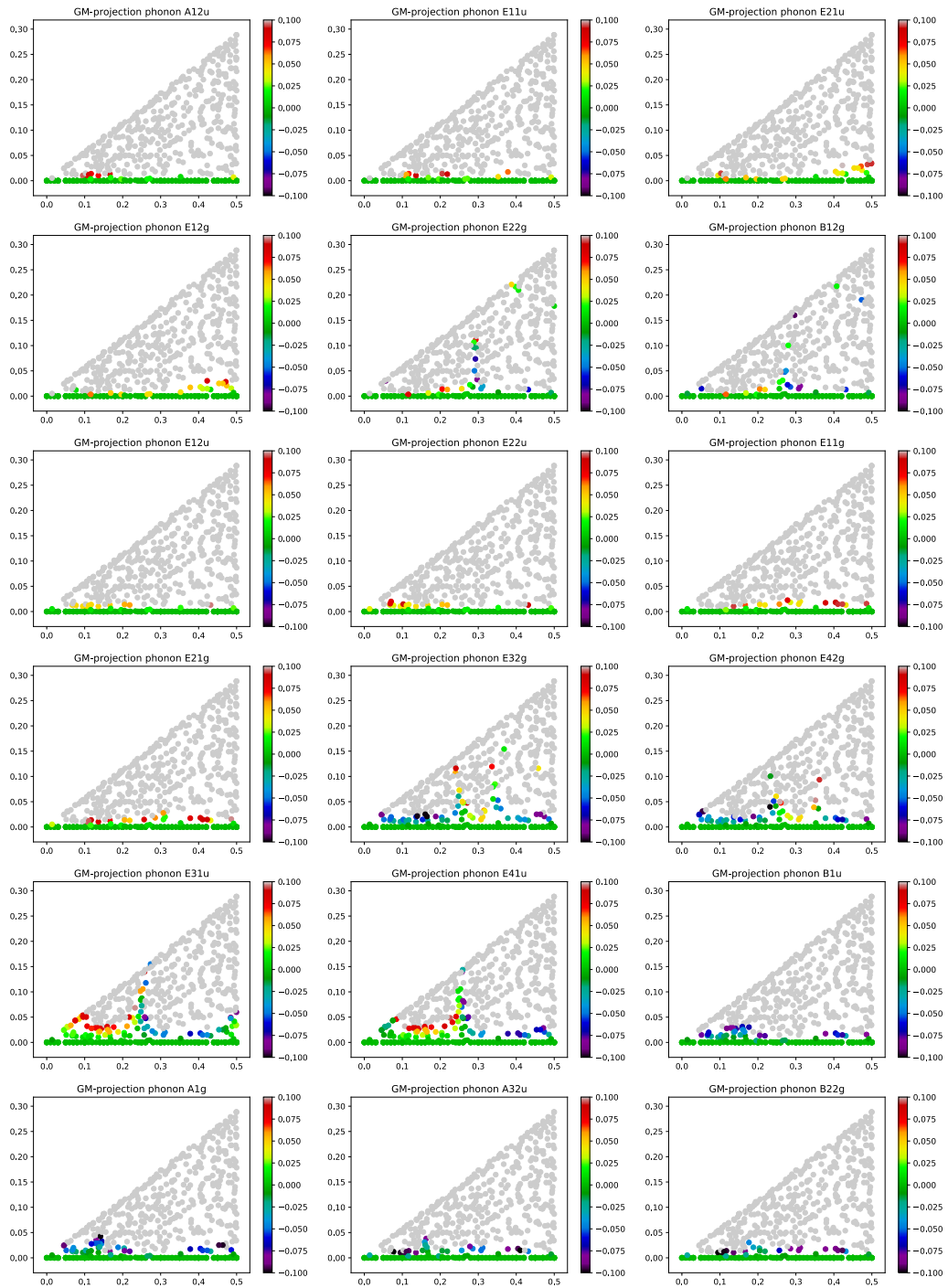
A 3.3.7. Plot error-heatmaps for hk in the IBZ

```
>>> plot_error_heatmap(error_GK)
... plot_error_heatmap(error_GM)
... plot_error_heatmap(error_KM)
```

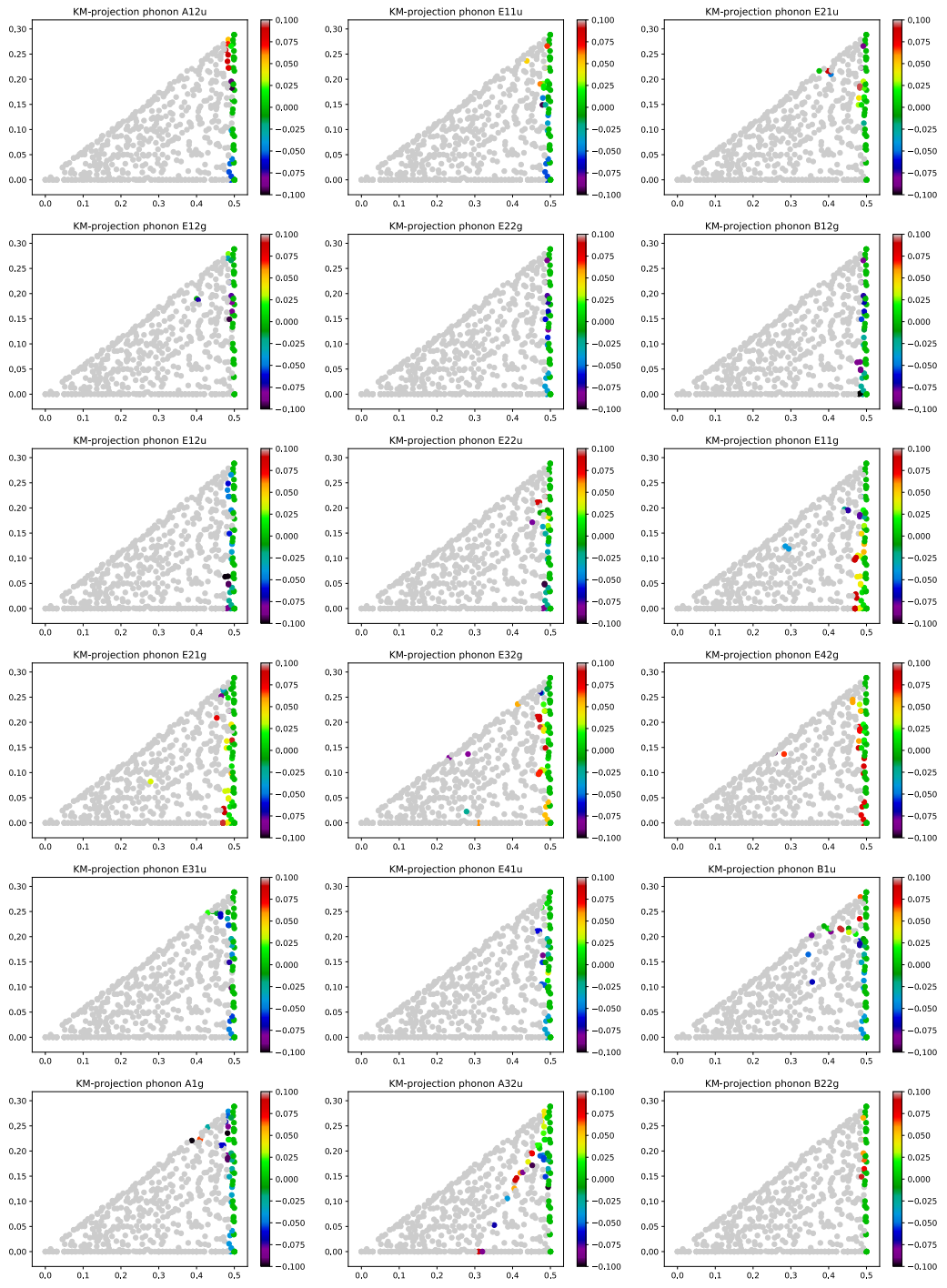
A 3. Python scripts used for IXS data analysis



A. Appendix



A 3. Python scripts used for IXS data analysis



A 3.3.8. Cleaning and reconstruction dataframes

Remove columns that are not relevant for the upcoming steps and rearrange data so that each phonon on each analyzer at each hkl is in an own row: sub-rows spanning across 'keep_cols' will remain rows, sub-rows spanning across 'transpose_cols' will become new error-column. This will allow to differentiate the errors for different phonons at the same reciprocal space point. Further, it will facilitate the process to fill in the fitted phonon energy from the IXS measurements into the table.

```
>>> ## first remove coordinate-columns from error-df's
... error_GK_clean=error_GK.drop(["x_IBZ", "y_IBZ"], axis=1)
... error_GM_clean=error_GM.drop(["x_IBZ", "y_IBZ"], axis=1)
... error_KM_clean=error_KM.drop(["x_IBZ", "y_IBZ"], axis=1)
...
... ## second concatenate df's containing the coordinates and resp error
... ## not to loose the connection of rows
... pre_results_GK = pd.concat((hkl_to_check.drop({"closest_index"}, axis=1),
...                               q_projected.q_GK,
...                               in_bounds_l.in_bounds_l,
...                               error_GK_clean), axis=1)
... pre_results_GM = pd.concat((hkl_to_check.drop({"closest_index"}, axis=1),
...                               q_projected.q_GM,
...                               in_bounds_l.in_bounds_l,
...                               error_GM_clean), axis=1)
... pre_results_KM = pd.concat((hkl_to_check.drop({"closest_index"}, axis=1),
...                               q_projected.q_KM,
...                               in_bounds_l.in_bounds_l,
...                               error_KM_clean), axis=1)
...
... # finally reconstruct!
... keep_cols = ["scan_no", "Analyzer", "h", "k", "l", "h_IBZ", "k_IBZ",
... ↪ "l_IBZ", "x_IBZ", "y_IBZ", "in_bounds_l"]
... transpose_cols = phonon_symmetry_names
...
... error_GK_rearranged = re_arange_data(pre_results_GK, frequencies_hkl,
... ↪ keep_cols, transpose_cols, "GK")
... error_GM_rearranged = re_arange_data(pre_results_GM, frequencies_hkl,
... ↪ keep_cols, transpose_cols, "GM")
... error_KM_rearranged = re_arange_data(pre_results_KM, frequencies_hkl,
... ↪ keep_cols, transpose_cols, "KM")

>>> error_GK_rearranged.head()
```

	scan_no	Analyzer	h	k	l	...	in_bounds_l	q_GK	\
0	64,84	A1	2.15	0.0	0.12	...	False	0.15	
1	64,84	A1	2.15	0.0	0.12	...	False	0.15	
2	64,84	A1	2.15	0.0	0.12	...	False	0.15	
3	64,84	A1	2.15	0.0	0.12	...	False	0.15	

```

4  64,84      A1  2.15  0.0  0.12      ...      False  0.15

   Phonon  errorGK  calc_energy_hkl
0  A12u    9.7141          5.078370
1  E11u    3.1731          6.377998
2  E21u    8.1879          7.777210
3  E12g    7.1453          8.443142
4  E22g   14.1653         11.849560

```

[5 rows x 15 columns]

A 3.3.9. Evaluation which (hkl) can be projected with acceptable error

```

>>> error_GK_rearranged["acct_err"]=acceptable_frequency_error
... error_GM_rearranged["acct_err"]=acceptable_frequency_error
... error_KM_rearranged["acct_err"]=acceptable_frequency_error
...
... # add (boolean) columns for which phonon the projection is acceptable,
... # further neglecting the l-out_of_bounds rows
... error_GK_rearranged=error_GK_rearranged.assign(fit_for_GK =
... ↪ (abs(error_GK_rearranged.errorGK) < error_GK_rearranged.acct_err) &
... ↪ error_GK_rearranged.in_bounds_l)
... error_GM_rearranged=error_GM_rearranged.assign(fit_for_GM =
... ↪ (abs(error_GM_rearranged.errorGM) < error_GK_rearranged.acct_err) &
... ↪ error_GK_rearranged.in_bounds_l)
... error_KM_rearranged=error_KM_rearranged.assign(fit_for_KM =
... ↪ (abs(error_KM_rearranged.errorKM) < error_GK_rearranged.acct_err) &
... ↪ error_GK_rearranged.in_bounds_l)
...
... # build final df containing all (relevant) data
... if remove_out_of_bounds_vals:
...     results = pd.concat((error_GK_rearranged.drop({"acct_err"}), axis=1),
...                          error_GM_rearranged.q_GM,
... ↪ error_GM_rearranged.errorGM, error_GM_rearranged.fit_for_GM,
...                          error_KM_rearranged.q_KM,
... ↪ error_KM_rearranged.errorKM, error_KM_rearranged.fit_for_KM
...                          ), axis=1
...     )
... else:
...     results = pd.concat((error_GK_rearranged,
...                          error_GM_rearranged.q_GM,
... ↪ error_GM_rearranged.errorGM, error_GM_rearranged.fit_for_GM,
...                          error_KM_rearranged.q_KM,
... ↪ error_KM_rearranged.errorKM, error_KM_rearranged.fit_for_KM
...                          ), axis=1
...     )
...
... # if data was chosen to be discarded in the INPUT-section,

```

A. Appendix

```
... # rows containing no q-value, i.e. not regarded as accurate
... # enough, will be dismissed
... if remove_out_of_bounds_vals:
...     at_least_one_acceptable=(results.fit_for_GK|results.fit_for_GM|results.
... ↪ fit_for_KM)
...     results = results[at_least_one_acceptable]
...     results.head()
...
... # add columns with the information, what was regarded as "acceptable"
... results["accept_l_deviation"]=l_tolerance
... results["accept_error"]=str(acceptable_frequency_error) + ' cm-1'
```

A 3.3.10. Remove q -values for directions with insufficient accuracy

Remove q -values for directions with insufficient accuracy, i.e. by removing the abscissa, the possibility for plotting is removed, ultimately discarding the data point for plotting (even if all columns were kept and a fitted phonon energy is included).

```
>>> drop_val = ""
... for direction in directions:
...     results.loc[~results[f"fit_for_{direction}"], f"q_{direction}"] =
... ↪ drop_val
... ## sort by phonon?
... #results.sort_values("Phonon").head()
```

```
>>> results.head()
```

	scan_no	Analyzer	h	k	l	...	q_KM	errorKM	fit_for_KM	\
0	64,84	A1	2.15	0.0	0.12	...	-88.2601		False	
1	64,84	A1	2.15	0.0	0.12	...	-80.3429		False	
2	64,84	A1	2.15	0.0	0.12	...	-77.2173		False	
3	64,84	A1	2.15	0.0	0.12	...	-77.3503		False	
4	64,84	A1	2.15	0.0	0.12	...	-77.9358		False	

	accept_l_deviation	accept_error
0	0.025	0.1 cm-1
1	0.025	0.1 cm-1
2	0.025	0.1 cm-1
3	0.025	0.1 cm-1
4	0.025	0.1 cm-1

```
[5 rows x 25 columns]
```

```
results
```

```
>>> # creating a column to insert fit values
... results["experimental_phonon_energy"] = ""
... results["weak_phonon_peaks"] = ""
...
... new_order = ['h', 'k', 'l', 'h_IBZ', 'k_IBZ', 'l_IBZ', 'x_IBZ', 'y_IBZ',
... ↪ 'accept_l_deviation', 'accept_error', 'errorGK', 'fit_for_GK', 'q_GK',
... ↪ 'errorGM', 'fit_for_GM', 'q_GM', 'errorKM', 'fit_for_KM', 'q_KM',
... ↪ 'scan_no', 'Analyzer', 'Phonon', 'calc_energy_hkl',
... ↪ 'experimental_phonon_energy']
... results = results[new_order]
...
... results.to_csv(output_file_name + ".csv", index=False)
```

A 3.3.11. Create list of spectra to fit

This step creates a list of spectra that need to be evaluated, i.e. facilitates the process of finding which spectra need to be fitted.

```
>>> fitlist = pd.DataFrame({
...     "scan_no": results.scan_no,
...     "Analyzer": results.Analyzer,
...     "index of results-table": results.index
... })
... at_least_one_to_fit =
... ↪ (results.fit_for_GK|results.fit_for_GM|results.fit_for_KM)
... fitlist = fitlist[at_least_one_to_fit]
... fitlist = fitlist.drop_duplicates(subset = {"scan_no", "Analyzer"})
... fitlist.to_csv("output_fitlist.csv", index=False)
```

A 3.4. Read FOURC files and split scans into files

This reads and splits the FOURC file(s) specified in the "files"-variable (INPUTS, section A 3.1), by matching the string-pattern to a regular expression. Each spectrum is written to the output path defined in INPUTS. If multiple FOURC files are used, it is necessary to choose a "scan_no_offset" for the subsequent file that is larger than the largest scan number (including offset) of the preceding file. Otherwise bijectiveness is lost.

```
>>> for file_dict in files:
...     file = file_dict["name"]
...     scan_no_offset = file_dict["scan_no_offset"]
...     read_and_split_FOURC(file, scan_no_offset)
```

A 3.5. Plot all spectra

To correct the spectra for an energy offset in the ‘correction and interpolation’ step, spectra containing Stokes and anti-Stokes pairs and/or Bragg peaks need to be identified for fitting. Since these plots are for visible inspection only, the energy is only the estimated energy “E_monot” from the FOURC file and not normalized to the flux “ione”, which only induce changes relevant for fitting.

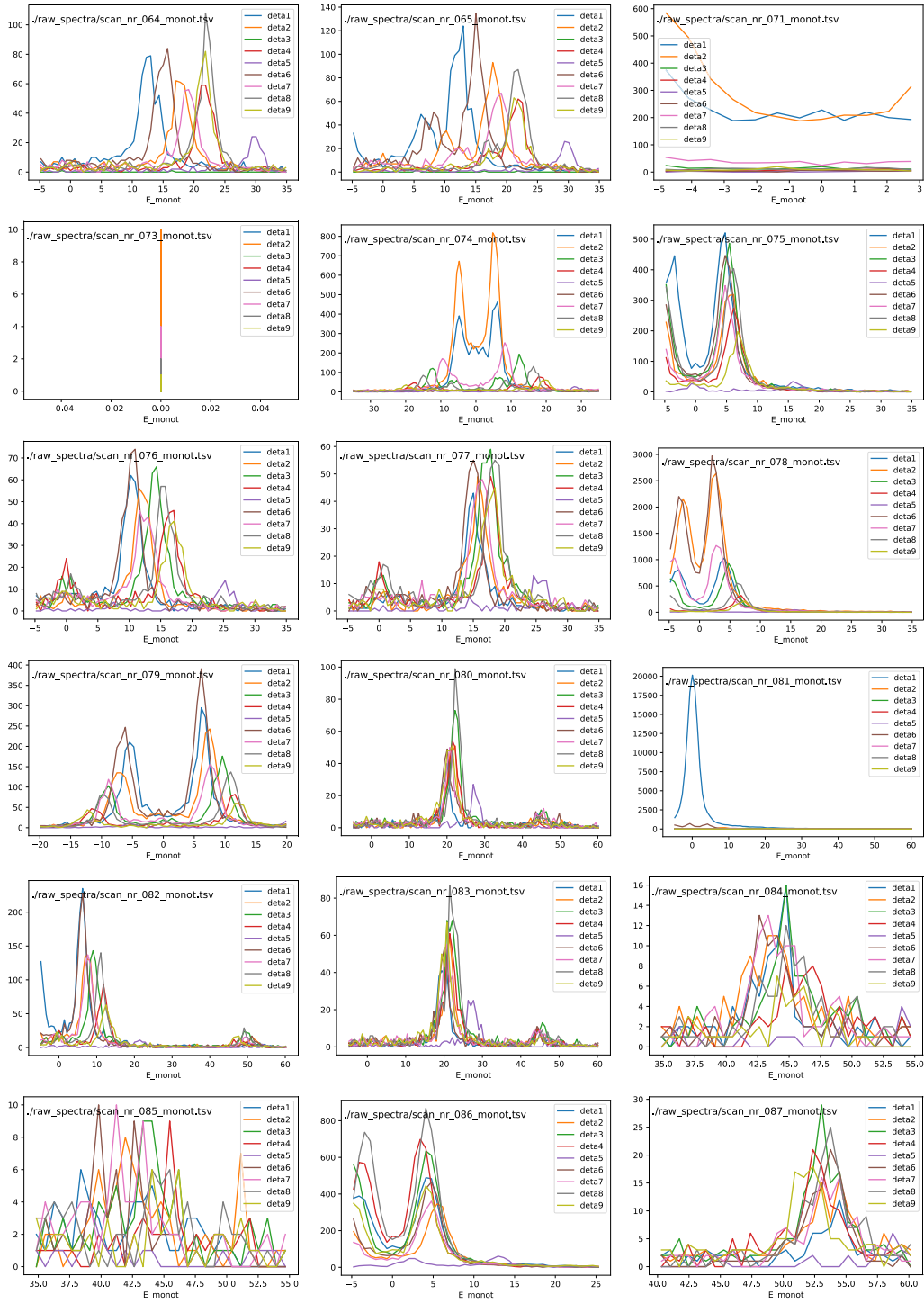
The spectra 95 and 157 contain no data and hence produce an error below.

```
>>> # path =r'./raw_spectra' # use your path
... allFiles = sorted(glob.glob(raw_spectra + "/*.tsv"))
...
... for f in allFiles:
...     scan = pd.read_csv(f, sep="\s+")
...     try:
...         if "Temperature" in scan.columns:
...             plot_all_Emonot(scan, f)
...     except Exception as e:
...         print("error in: ", f)
```

```
/home/hans/anaconda3/lib/python3.7/site-packages/matplotlib/pyplot.py:522:
RuntimeWarning: More than 20 figures have been opened. Figures created through the
pyplot interface (`matplotlib.pyplot.figure`) are retained until explicitly closed and
may consume too much memory. (To control this warning, see the rcParam
`figure.max_open_warning`).
max_open_warning, RuntimeWarning)
```

```
error in: ./raw_spectra/scan_nr_095_monot.tsv
error in: ./raw_spectra/scan_nr_157_monot.tsv
```

A 3. Python scripts used for IXS data analysis



A 3.6. Offset correction and interpolation of spectra

Offset correction through the given Stokes-anti-Stokes-pairs / Bragg-shift in the 'offset_table' (INPUTS). If multiple spectra are given for one (hkl), the common energy range will be interpolated and averaged. Spectra will be written to the 'output_file_path' defined.

```
>>> # list of scans, covert to three digits if less
... scans = pd.read_csv(scan_list, sep="\s+", dtype=np.float)
... scans = scans.applymap(lambda x: '{0:0>3.0f}'.format(x))
...
... # offsets of all analyzers for all scans determined by SAS or Bragg peaks
... offsets = pd.read_csv(offset_table, sep="\t")
... offsets["scan"]=offsets["scan"].apply(lambda x: '{0:0>3.0f}'.format(x))
... offsets.index=offsets.scan
... # for each line in 'scans' (one (hkl))
... for index, row in scans.iterrows():
...     # for each analyzer
...     for analyzer in range(1, 10):
...         interpol, file_name = interpolate_and_correct(row, offsets,
... ↪ analyzer)
...         interpol.to_csv(file_name, index=False, sep=" ")
...
... offsets.head()
```

	scan	A1	A2	A3	A4	A5	A6	A7	A8	\
scan										
064	064	-263.24	-395.6	-132.62	148.67	-302.68	-294.66	-325.86	-364.73	
065	065	-263.24	-395.6	-132.62	148.67	-302.68	-294.66	-325.86	-364.73	
066	066	-263.24	-395.6	-132.62	148.67	-302.68	-294.66	-325.86	-364.73	
067	067	-263.24	-395.6	-132.62	148.67	-302.68	-294.66	-325.86	-364.73	
068	068	-263.24	-395.6	-132.62	148.67	-302.68	-294.66	-325.86	-364.73	
	A9									
scan										
064		-347.15								
065		-347.15								
066		-347.15								
067		-347.15								
068		-347.15								

A 3.7. Python script to reformat measurement table

Script to reformat the previously generated table, now filled with values from the experiment, into a shape so that the dispersion can be readily plotted. This means that rows and columns are sorted so that for each reciprocal space point hkl, two sets of coulmnns for each phonon exists. The second set of phonon-columns is present to allow to distinguish datapoint originating from strong and weak peaks.

A 3. Python scripts used for IXS data analysis

```
>>> import pandas as pd
... inputfilename = "output_pre-selection_of_hkl"
... phonon_symmetry_names = [ ## in the order given in the calculated dispersion
... "A12u", "E11u", "E21u", "E12g", "E22g", "B12g",
... "E12u", "E22u", "E11g", "E21g", "E32g", "E42g",
... "E31u", "E41u", "B1u", "A1g", "A32u", "B22g"
... ]
... weak_phonon_symmetry_names = [s + "_weak" for s in phonon_symmetry_names]
...
... pd.set_option("display.max_columns", 100)

>>> riesentabelle = pd.read_csv(f"{inputfilename}.csv", sep=",")#,
... ↔ header=infer)#, names=["x","y", *phonon_symmetry_names])

>>> riesentabelle.iloc[15:20]
```

	h	k	l	h_IBZ	k_IBZ	l_IBZ	x_IBZ	y_IBZ	accept_l_deviation	\
15	2.15	0.0	0.12	0.15	0.0	0.12	0.15	0.0	0.025	
16	2.15	0.0	0.12	0.15	0.0	0.12	0.15	0.0	0.025	
17	2.15	0.0	0.12	0.15	0.0	0.12	0.15	0.0	0.025	
18	2.20	0.0	0.07	0.20	0.0	0.07	0.20	0.0	0.025	
19	2.20	0.0	0.07	0.20	0.0	0.07	0.20	0.0	0.025	

	accept_error	errorGK	fit_for_GK	q_GK	errorGM	fit_for_GM	q_GM	\
15	0.1	cm-1	-1.3067	False	NaN	0.0	False	NaN
16	0.1	cm-1	-4.0516	False	NaN	0.0	False	NaN
17	0.1	cm-1	-4.5078	False	NaN	0.0	False	NaN
18	0.1	cm-1	12.9793	False	NaN	0.0	False	NaN
19	0.1	cm-1	7.2184	False	NaN	0.0	False	NaN

	errorKM	fit_for_KM	q_KM	scan_no	Analyzer	Phonon	calc_energy_hkl	\
15	43.8692	False	NaN	64,84	A1	A1g	51.319800	
16	10.7930	False	NaN	64,84	A1	A32u	51.350920	
17	14.9217	False	NaN	64,84	A1	B22g	51.884139	
18	-68.0103	False	NaN	64,84	A6	A12u	7.589027	
19	-67.9633	False	NaN	64,84	A6	E11u	7.912874	

	experimental_phonon_energy
15	NaN
16	NaN
17	NaN
18	NaN
19	NaN

```
>>> origin = pd.DataFrame(riesentabelle.copy())
... origin = origin.drop(["experimental_phonon_energy"], axis=1)
```

A. Appendix

```
...
... origin = origin.append(pd.DataFrame(columns=list(phonon_symmetry_names)),
... ↪ sort=False)
...
... for row in range(len(origin)):
...     phonon_under_consideration = origin.loc[row, "Phonon"]
...     weak_phonon_under_consideration = origin.loc[row, "Phonon"] + "_weak"
...     origin.loc[row, phonon_under_consideration] =
... ↪ riesentabelle.loc[row, "experimental_phonon_energy"]
... #     origin.loc[row, weak_phonon_under_consideration] =
... ↪ riesentabelle.loc[row, "weak_phonon_peaks"]
...
... #origin.head(20)

>>> origin.to_csv(f"{inputfilename}-dispersion-for-origin.csv", index=True,
... ↪ sep=",")
```

References

- ¹R. G. Dickinson and L. Pauling, "The crystal structure of molybdenite", *Journal of the American Chemical Society* **45**, 1466–1471 (1923).
- ²R. F. Frindt and A. D. Yoffe, "Physical Properties of Layer Structures: Optical Properties and Photoconductivity of Thin Crystals of Molybdenum Disulphide", *Proceedings of the Royal Society A: Mathematical, Physical and Engineering Sciences* **273**, 69–83 (1963).
- ³J. Wilson and A. Yoffe, "The transition metal dichalcogenides discussion and interpretation of the observed optical, electrical and structural properties", *Advances in Physics* **18**, 193–335 (1969).
- ⁴K. S. Novoselov, A. K. Geim, S. V. Morozov, D. Jiang, Y. Zhang, S. V. Dubonos, I. V. Grigorieva, and A. A. Firsov, "Electric Field Effect in Atomically Thin Carbon Films", *Science* **306**, 666–669 (2004).
- ⁵K. He, N. Kumar, L. Zhao, Z. Wang, K. F. Mak, H. Zhao, and J. Shan, "Tightly Bound Excitons in Monolayer WSe₂", *Physical Review Letters* **113**, 026803 (2014).
- ⁶A. Chernikov, T. C. Berkelbach, H. M. Hill, A. Rigosi, Y. Li, O. B. Aslan, D. R. Reichman, M. S. Hybertsen, and T. F. Heinz, "Exciton Binding Energy and Nonhydrogenic Rydberg Series in Monolayer WS₂", *Physical Review Letters* **113**, 076802 (2014).
- ⁷Z. Ye, T. Cao, K. O'Brien, H. Zhu, X. Yin, Y. Wang, S. G. Louie, and X. Zhang, "Probing excitonic dark states in single-layer tungsten disulphide", *Nature* **513**, 214–218 (2014).
- ⁸B. Zhu, X. Chen, and X. Cui, "Exciton Binding Energy of Monolayer WS₂", *Scientific Reports* **5**, 9218 (2015).
- ⁹C. Zhang, A. Johnson, C.-L. Hsu, L.-J. Li, and C.-K. Shih, "Direct Imaging of Band Profile in Single Layer MoS₂ on Graphite: Quasiparticle Energy Gap, Metallic Edge States, and Edge Band Bending", *Nano Letters* **14**, 2443–2447 (2014).

- ¹⁰M. M. Ugeda, A. J. Bradley, S. F. Shi, F. H. Da Jornada, Y. Zhang, D. Y. Qiu, W. Ruan, S. K. Mo, Z. Hussain, Z. X. Shen, F. Wang, S. G. Louie, and M. F. Crommie, "Giant bandgap renormalization and excitonic effects in a monolayer transition metal dichalcogenide semiconductor", *Nature Materials* **13**, 1091–1095 (2014).
- ¹¹D. Xiao, G.-B. Liu, W. Feng, X. Xu, and W. Yao, "Coupled Spin and Valley Physics in Monolayers of MoS₂ and Other Group-VI Dichalcogenides", *Physical Review Letters* **108**, 196802 (2012).
- ¹²K. Kořmider, J. W. González, and J. Fernández-Rossier, "Large spin splitting in the conduction band of transition metal dichalcogenide monolayers", *Physical Review B* **88**, 245436 (2013).
- ¹³A. Molina-Sánchez, D. Sangalli, K. Hummer, A. Marini, and L. Wirtz, "Effect of spin-orbit interaction on the optical spectra of single-layer, double-layer, and bulk MoS₂", *Physical Review B* **88**, 045412 (2013).
- ¹⁴R. Gillen and J. Maultzsch, "Light-Matter Interactions in Two-Dimensional Transition Metal Dichalcogenides: Dominant Excitonic Transitions in Mono- and Few-Layer MoX₂ and Band Nesting", *IEEE Journal of Selected Topics in Quantum Electronics* **23**, 219–230 (2017).
- ¹⁵T. Cao, G. Wang, W. Han, H. Ye, C. Zhu, J. Shi, Q. Niu, P. Tan, E. Wang, B. Liu, and J. Feng, "Valley-selective circular dichroism of monolayer molybdenum disulphide", *Nature Communications* **3**, 887 (2012).
- ¹⁶X. Xu, W. Yao, D. Xiao, and T. F. Heinz, "Spin and pseudospins in layered transition metal dichalcogenides", *Nature Physics* **10**, 343–350 (2014).
- ¹⁷M. M. Glazov, E. L. Ivchenko, G. Wang, T. Amand, X. Marie, B. Urbaszek, and B. L. Liu, "Spin and valley dynamics of excitons in transition metal dichalcogenide monolayers", *physica status solidi (b)* **252**, 2349–2362 (2015).
- ¹⁸K. F. Mak, K. He, J. Shan, and T. F. Heinz, "Control of valley polarization in monolayer MoS₂ by optical helicity.", *Nature nanotechnology* **7**, 494–498 (2012).
- ¹⁹H. Zeng, J. Dai, W. Yao, D. Xiao, and X. Cui, "Valley polarization in MoS₂ monolayers by optical pumping", *Nature nanotechnology* **7**, 490–493 (2012).
- ²⁰N. C. Bishop, M. Padmanabhan, K. Vakili, Y. P. Shkolnikov, E. P. De Poortere, and M. Shayegan, "Valley Polarization and Susceptibility of Composite Fermions around a Filling Factor $\nu=3/2$ ", *Physical Review Letters* **98**, 266404 (2007).
- ²¹Z. Zhu, J. Wang, H. Zuo, B. Fauqué, R. D. McDonald, Y. Fuseya, and K. Behnia, "Emptying Dirac valleys in bismuth using high magnetic fields", *Nature Communications* **8**, 15297 (2017).

- ²²A. Rycerz, J. Tworzydło, and C. W. J. Beenakker, “Valley filter and valley valve in graphene”, *Nature Physics* **3**, 172–175 (2007).
- ²³D. Xiao, W. Yao, and Q. Niu, “Valley-Contrasting Physics in Graphene: Magnetic Moment and Topological Transport”, *Physical Review Letters* **99**, 236809 (2007).
- ²⁴W. Yao, D. Xiao, and Q. Niu, “Valley-dependent optoelectronics from inversion symmetry breaking”, *Physical Review B* **77**, 235406 (2008).
- ²⁵J. R. Schaibley, H. Yu, G. Clark, P. Rivera, J. S. Ross, K. L. Seyler, W. Yao, and X. Xu, “Valleytronics in 2D materials”, *Nature Reviews Materials* **1**, 16055 (2016).
- ²⁶G. Sallen, L. Bouet, X. Marie, G. Wang, C. R. Zhu, W. P. Han, Y. Lu, P. H. Tan, T. Amand, B. L. Liu, and B. Urbaszek, “Robust optical emission polarization in MoS₂ monolayers through selective valley excitation”, *Physical Review B* **86**, 081301 (2012).
- ²⁷H. Jang, K. P. Dhakal, K. Joo, W. S. Yun, S. M. Shinde, X. Chen, S. M. Jeong, S. W. Lee, Z. Lee, J. Lee, J. Ahn, and H. Kim, “Transient SHG imaging on ultrafast carrier dynamics of MoS₂ nanosheets”, *Advanced Materials* **30**, 1705190 (2018).
- ²⁸C. Ruppert, A. Chernikov, H. M. Hill, A. F. Rigosi, and T. F. Heinz, “The role of electronic and phononic excitation in the optical response of monolayer WS₂ after ultrafast excitation”, *Nano Letters* **17**, 644–651 (2017).
- ²⁹K. Rossnagel, “Two-dimensional materials - more than electrons”, *Nature Materials* **17**, 658–660 (2018).
- ³⁰M. Kang, S. W. Jung, W. J. Shin, Y. Sohn, S. H. Ryu, T. K. Kim, M. Hoesch, and K. S. Kim, “Holstein polaron in a valley-degenerate two-dimensional semiconductor”, *Nature Materials* **17**, 676–680 (2018).
- ³¹L. Yang, N. A. Sinitsyn, W. Chen, J. Yuan, J. Zhang, J. Lou, and S. A. Crooker, “Long-lived nanosecond spin relaxation and spin coherence of electrons in monolayer MoS₂ and WS₂”, *Nature Physics* **11**, 830–834 (2015).
- ³²N. Wakabayashi, H. G. Smith, and R. M. Nicklow, “Lattice dynamics of hexagonal MoS₂ studied by neutron scattering”, *Physical Review B* **12**, 659–663 (1975).
- ³³T. J. Wieting and M. Schlüter, eds., *Electrons and Phonons in Layered Crystal Structures* (D. Reidel publishing company (Dordrecht), 1979).
- ³⁴A. Molina-Sánchez and L. Wirtz, “Phonons in single-layer and few-layer MoS₂ and WS₂”, *Physical Review B* **84**, 1–8 (2011).
- ³⁵C. Ataca, H. Şahin, and S. Ciraci, “Stable, Single-Layer MX₂ Transition-Metal Oxides and Dichalcogenides in a Honeycomb-Like Structure”, *Journal of Physical Chemistry C* **116**, 8983–8999 (2012).

- ³⁶J. M. Lu, O. Zheliuk, I. Leermakers, N. F. Q. Yuan, U. Zeitler, K. T. Law, and J. T. Ye, “Evidence for two-dimensional Ising superconductivity in gated MoS₂”, *Science* **350**, 1353–1357 (2015).
- ³⁷W.-Y. He, B. T. Zhou, J. J. He, N. F. Q. Yuan, T. Zhang, and K. T. Law, “Magnetic field driven nodal topological superconductivity in monolayer transition metal dichalcogenides”, *Communications Physics* **1**, 40 (2018).
- ³⁸J. Ribeiro-Soares, R. M. Almeida, E. B. Barros, P. T. Araujo, M. S. Dresselhaus, L. G. Cançado, and A. Jorio, “Group theory analysis of phonons in two-dimensional transition metal dichalcogenides”, *Physical Review B* **90**, 115438 (2014).
- ³⁹J. W. Leech and D. J. Newman, *How to use groups*, edited by B. L. Worsnop and G. K. T. Conn (Scientific paperbacks (Birkenhead), 1970).
- ⁴⁰A. Splendiani, L. Sun, Y. Zhang, T. Li, J. Kim, C. Y. Chim, G. Galli, and F. Wang, “Emerging photoluminescence in monolayer MoS₂”, *Nano Letters* **10**, 1271–1275 (2010).
- ⁴¹F. Xia, H. Wang, D. Xiao, M. Dubey, and A. Ramasubramaniam, “Two-dimensional material nanophotonics”, *Nature Photonics* **8**, 899–907 (2014).
- ⁴²O. A. Ajayi, J. V. Ardelean, G. D. Shepard, J. Wang, A. Antony, T. Taniguchi, K. Watanabe, T. F. Heinz, S. Strauf, X.-Y. Zhu, and J. C. Hone, “Approaching the intrinsic photoluminescence linewidth in transition metal dichalcogenide monolayers”, *2D Materials* **4**, 031011 (2017).
- ⁴³G. Wang, A. Chernikov, M. M. Glazov, T. F. Heinz, X. Marie, T. Amand, and B. Urbaszek, “Colloquium : Excitons in atomically thin transition metal dichalcogenides”, *Reviews of Modern Physics* **90**, 021001 (2018).
- ⁴⁴J. Hong, K. Li, C. Jin, X. Zhang, Z. Zhang, and J. Yuan, “Layer-dependent anisotropic electronic structure of freestanding quasi-two-dimensional MoS₂”, *Physical Review B* **93**, 075440 (2016).
- ⁴⁵Y. Zhang, T. R. Chang, B. Zhou, Y. T. Cui, H. Yan, Z. Liu, F. Schmitt, J. Lee, R. Moore, Y. Chen, H. Lin, H. T. Jeng, S. K. Mo, Z. Hussain, A. Bansil, and Z. X. Shen, “Direct observation of the transition from indirect to direct bandgap in atomically thin epitaxial MoSe₂”, *Nature Nanotechnology* **9**, 111–115 (2014).
- ⁴⁶A. Kormányos, G. Burkard, M. Gmitra, J. Fabian, V. Zólyomi, N. D. Drummond, and V. Fal’ko, “k.p theory for two-dimensional transition metal dichalcogenide semiconductors”, *2D Materials* **2**, 049501 (2015).
- ⁴⁷K. F. Mak, C. Lee, J. Hone, J. Shan, and T. F. Heinz, “Atomically thin MoS₂: A new direct-gap semiconductor”, *Physical Review Letters* **105**, 2–5 (2010).

- ⁴⁸J. W. Christopher, B. B. Goldberg, and A. K. Swan, “Long tailed trions in monolayer MoS₂: Temperature dependent asymmetry and resulting red-shift of trion photoluminescence spectra”, *Scientific Reports* **7**, 14062 (2017).
- ⁴⁹Z. Y. Zhu, Y. C. Cheng, and U. Schwingenschlögl, “Giant spin-orbit-induced spin splitting in two-dimensional transition-metal dichalcogenide semiconductors”, *Physical Review B* **84**, 1–5 (2011).
- ⁵⁰A. Kormányos, V. Zólyomi, N. D. Drummond, and G. Burkard, “Spin-Orbit Coupling, Quantum Dots, and Qubits in Monolayer Transition Metal Dichalcogenides”, *Physical Review X* **4**, 011034 (2014).
- ⁵¹D. W. Latzke, W. Zhang, A. Suslu, T.-R. Chang, H. Lin, H.-T. Jeng, S. Tongay, J. Wu, A. Bansil, and A. Lanzara, “Electronic structure, spin-orbit coupling, and interlayer interaction in bulk MoS₂ and WS₂”, *Physical Review B* **91**, 235202 (2015).
- ⁵²Y. C. Cheng, Z. Y. Zhu, M. Tahir, and U. Schwingenschlögl, “Spin-orbit-induced spin splittings in polar transition metal dichalcogenide monolayers”, *Europhysics Letters* **102**, 57001 (2013).
- ⁵³M. Selig, G. Berghäuser, A. Raja, P. Nagler, C. Schüller, T. F. Heinz, T. Korn, A. Chernikov, E. Malic, and A. Knorr, “Excitonic linewidth and coherence lifetime in monolayer transition metal dichalcogenides”, *Nature Communications* **7**, 13279 (2016).
- ⁵⁴J. Lindlau, M. Selig, A. Neumann, L. Colombier, J. Förste, V. Funk, M. Förg, J. Kim, G. Berghäuser, T. Taniguchi, K. Watanabe, F. Wang, E. Malic, and A. Högele, “The role of momentum-dark excitons in the elementary optical response of bilayer WSe₂”, *Nature Communications* **9**, 2586 (2018).
- ⁵⁵J. Feng, X. Qian, C. W. Huang, and J. Li, “Strain-engineered artificial atom as a broad-spectrum solar energy funnel”, *Nature Photonics* **6**, 866–872 (2012).
- ⁵⁶D. Y. Qiu, F. H. da Jornada, and S. G. Louie, “Optical Spectrum of MoS₂: Many-Body Effects and Diversity of Exciton States”, *Physical Review Letters* **111**, 216805 (2013).
- ⁵⁷P. Y. Yu, *Fundamentals of semiconductors : physics and materials properties*, eng, 4. ed. (Springer (Berlin, Heidelberg), 2010).
- ⁵⁸A. R. Hutson, “Hall Effect Studies of Doped Zinc Oxide Single Crystals”, *Physical Review* **108**, 222–230 (1957).
- ⁵⁹A. Mang, K. Reimann, and S. Riibenacke, “Band gaps, crystal-field splitting, spin-orbit coupling, and exciton binding energies in ZnO under hydrostatic pressure”, *Solid State Communications*, **94**, 251–254 (1995).
- ⁶⁰N. Scheuschner, R. Gillen, M. Staiger, and J. Maultzsch, “Interlayer resonant Raman modes in few-layer MoS₂”, *Physical Review B* **91**, 235409 (2015).

- ⁶¹H. Peelaers and C. G. Van de Walle, “Effects of strain on band structure and effective masses in MoS₂”, *Physical Review B* **86**, 241401 (2012).
- ⁶²S. Horzum, H. Sahin, S. Cahangirov, P. Cudazzo, A. Rubio, T. Serin, and F. M. Peeters, “Phonon softening and direct to indirect band gap crossover in strained single-layer MoSe₂”, *Physical Review B* **87**, 1–5 (2013).
- ⁶³W. R. L. Lambrecht, A. V. Rodina, S. Limpijumnong, B. Segall, and B. K. Meyer, “Valence-band ordering and magneto-optic exciton fine structure in ZnO”, *Physical Review B* **65**, 075207 (2002).
- ⁶⁴(Nov. 2018) <http://www.ioffe.ru/SVA/NSM/Semicond/GaAs/basic.html>.
- ⁶⁵T. Cheiwchanchamnangij and W. R. L. Lambrecht, “Quasiparticle band structure calculation of monolayer, bilayer, and bulk MoS₂”, *Physical Review B* **85**, 205302 (2012).
- ⁶⁶“Zinc oxide (ZnO) dielectric constants”, in *II-VI and I-VII Compounds; Semimagnetic Compounds*, edited by O. Madelung, U. Rössler, and M. Schulz (Springer Berlin Heidelberg, Berlin, Heidelberg, 1999), pp. 1–10.
- ⁶⁷K. F. Mak, K. He, C. Lee, G. Lee, and J. Hone, “Tightly bound trions in monolayer MoS₂”, *Nature Materials* **12**, 207–211 (2012).
- ⁶⁸A. M. Jones, H. Yu, N. J. Ghimire, S. Wu, G. Aivazian, J. S. Ross, B. Zhao, J. Yan, D. G. Mandrus, D. Xiao, W. Yao, and X. Xu, “Optical generation of excitonic valley coherence in monolayer WSe₂”, *Nature Nanotechnology* **8** (2013).
- ⁶⁹J. S. Ross, S. Wu, H. Yu, N. J. Ghimire, A. M. Jones, G. Aivazian, J. Yan, D. G. Mandrus, D. Xiao, W. Yao, and X. Xu, “Electrical control of neutral and charged excitons in a monolayer semiconductor.”, *Nature Communications* **4**, 1474 (2013).
- ⁷⁰H. Yu, X. Cui, X. Xu, and W. Yao, “Valley excitons in two-dimensional semiconductors”, *National Science Review* **2**, 57–70 (2015).
- ⁷¹A. A. Mitioğlu, P. Plochocka, J. N. Jadcak, W. Escoffier, G. L. J. A. Rikken, L. Kulyuk, and D. K. Maude, “Optical manipulation of the exciton charge state in single-layer tungsten disulfide”, *Physical Review B* **88**, 245403 (2013).
- ⁷²B. Radisavljevic, A. Radenovic, J. Brivio, V. Giacometti, and A. Kis, “Single-layer MoS₂ transistors”, *Nature Nanotechnology* **6** (2011).
- ⁷³K. K. Tiong, P. C. Liao, C. H. Ho, and Y. S. Huang, “Growth and characterization of rhenium-doped MoS single crystals”, *Journal of Crystal Growth* **205**, 543–547 (1999).
- ⁷⁴N. Scheuschner, “Photolumineszenz- und Raman-Spektroskopie von zweidimensionalem MoS₂”, PhD thesis (Technische Universität Berlin, 2017).

- ⁷⁵N. Kumar, S. Najmaei, Q. Cui, F. Ceballos, P. M. Ajayan, J. Lou, and H. Zhao, "Second harmonic microscopy of monolayer MoS₂", *Physical Review B* **87**, 161403 (2013).
- ⁷⁶T. Wieting and J. Verble, "Infrared and Raman studies of long-wavelength optical phonons in hexagonal MoS₂", *Physical Review B* **3**, 4286–4292 (1971).
- ⁷⁷M. Staiger, R. Gillen, N. Scheuschner, O. Ochedowski, F. Kampmann, M. Schleberger, C. Thomsen, and J. Maultzsch, "Splitting of monolayer out-of-plane A₁' Raman mode in few-layer WS₂", *Physical Review B* **91**, 195419 (2015).
- ⁷⁸N. Scheuschner, O. Ochedowski, M. Schleberger, and J. Maultzsch, "Resonant Raman profiles and μ -photoluminescence of atomically thin layers of molybdenum disulfide", *physica status solidi (b)* **249**, 2644–2647 (2012).
- ⁷⁹C. Lee, H. Yan, L. E. Brus, T. F. Heinz, J. Hone, and S. Ryu, "Anomalous Lattice Vibrations of Single- and Few-Layer MoS₂", *ACS Nano* **4**, 2695–2700 (2010).
- ⁸⁰J. Serrano, F. J. Manjón, A. H. Romero, A. Ivanov, M. Cardona, R. Lauck, A. Bosak, and M. Krisch, "Phonon dispersion relations of zinc oxide: Inelastic neutron scattering and ab initio calculations", *Physical Review B* **81**, 174304 (2010).
- ⁸¹M. Krisch and F. Sette, *Light scattering in solids. IX, Novel materials and techniques. Chapter: Inelastic X-Ray Scattering from Phonons*, eng, edited by M. Cardona and R. Merlin, Topics in applied physics (Springer (Berlin, Heidelberg), 2007).
- ⁸²A. Q. R. Baron, "Introduction to high-resolution inelastic x-ray scattering", *arXiv*, 1504.01098v5 (2015).
- ⁸³H. Yumoto, H. Mimura, T. Koyama, S. Matsuyama, K. Tono, T. Togashi, Y. Inubushi, T. Sato, T. Tanaka, T. Kimura, H. Yokoyama, J. Kim, Y. Sano, Y. Hachisu, M. Yabashi, H. Ohashi, H. Ohmori, T. Ishikawa, and K. Yamauchi, "Focusing of X-ray free-electron laser pulses with reflective optics", *Nature Photonics* **7**, 43–47 (2013).
- ⁸⁴E. Burkel, *Springer tracts in modern physics Volume 125: Inelastic scattering of X-Rays with very high energy resolution* (Springer (Berlin, New York, Heidelberg), 1991).
- ⁸⁵E. Burkel, "Phonon spectroscopy by inelastic x-ray scattering", *Reports on Progress in Physics* **63**, 171–232 (2000).
- ⁸⁶M. D'Austo and M. Krisch, "High resolution inelastic X-ray scattering from thermal collective excitations", *Collection SFN* **10**, 487–503 (2010).
- ⁸⁷R. Loudon, "The Raman effect in crystals", *Advances in Physics* **13**, 423–482 (1964).

- ⁸⁸R. F. Frindt, "Single Crystals of MoS₂ Several Molecular Layers Thick", *Journal of Applied Physics* **1928**, 130–132 (1966).
- ⁸⁹K. S. Novoselov, D. Jiang, F. Schedin, T. J. Booth, V. V. Khotkevich, S. V. Morozov, and A. K. Geim, "Two-dimensional atomic crystals", *Proceedings of the National Academy of Sciences* **102**, 10451–10453 (2005).
- ⁹⁰H. P. Boehm, A. Clauss, G. O. Fischer, and U. Hofmann, "Das Adsorptionsverhalten sehr dünner Kohlenstoff-Folien", *Zeitschrift für anorganische und allgemeine Chemie* **316**, 119–127 (1962).
- ⁹¹C. Casiraghi, A. Hartschuh, E. Lidorikis, H. Qian, H. Harutyunyan, T. Gokus, K. S. Novoselov, and A. C. Ferrari, "Rayleigh Imaging of Graphene and Graphene Layers", *Nano Letters* **7**, 2711–2717 (2007).
- ⁹²H. Li, J. Wu, X. Huang, G. Lu, J. Yang, X. Lu, Q. Xiong, and H. Zhang, "Rapid and Reliable Thickness Identification of Two-Dimensional Nanosheets Using Optical Microscopy", *ACS Nano* **7**, 10344–10353 (2013).
- ⁹³*Private communications with Dr. Niko Tombros (HQ graphene, Netherlands).*
- ⁹⁴P. Joensen, R. Frindt, and S. Morrison, "Single-layer MoS₂", *Materials Research Bulletin* **21**, 457–461 (1986).
- ⁹⁵J. N. Coleman, M. Lotya, A. O'Neill, S. D. Bergin, P. J. King, U. Khan, K. Young, A. Gaucher, S. De, R. J. Smith, I. V. Shvets, S. K. Arora, G. Stanton, H.-Y. Kim, K. Lee, G. T. Kim, G. S. Duesberg, T. Hallam, J. J. Boland, J. J. Wang, J. F. Donegan, J. C. Grunlan, G. Moriarty, A. Shmeliov, R. J. Nicholls, J. M. Perkins, E. M. Grieveson, K. Theuwissen, D. W. McComb, P. D. Nellist, and V. Nicolosi, "Two-Dimensional Nanosheets Produced by Liquid Exfoliation of Layered Materials", *Science* **331**, 568–571 (2011).
- ⁹⁶C. Backes, T. M. Higgins, A. Kelly, C. Boland, A. Harvey, D. Hanlon, and J. N. Coleman, "Guidelines for Exfoliation, Characterization and Processing of Layered Materials Produced by Liquid Exfoliation", *Chemistry of Materials* **29**, 243–255 (2017).
- ⁹⁷A. Koma, "Van der Waals epitaxy a new epitaxial growth method for a highly lattice-mismatched system", *Thin Solid Films* **216**, 72–76 (1992).
- ⁹⁸Y. Shi, W. Zhou, A.-Y. Lu, W. Fang, Y.-H. Lee, A. L. Hsu, S. M. Kim, K. K. Kim, H. Y. Yang, L.-J. Li, J.-C. Idrobo, and J. Kong, "van der Waals Epitaxy of MoS₂ Layers Using Graphene As Growth Templates", *Nano Letters* **12**, 2784–2791 (2012).
- ⁹⁹Y. Zhan, Z. Liu, S. Najmaei, P. M. Ajayan, and J. Lou, "Large-Area Vapor-Phase Growth and Characterization of MoS₂ Atomic Layers on a SiO₂ Substrate", *Small* **8**, 966–971 (2012).

- ¹⁰⁰A. M. van der Zande, P. Y. Huang, D. a. Chenet, T. C. Berkelbach, Y. You, G.-H. Lee, T. F. Heinz, D. R. Reichman, D. a. Muller, and J. C. Hone, “Grains and grain boundaries in highly crystalline monolayer molybdenum disulphide”, *Nature Materials* **12**, 554–561 (2013).
- ¹⁰¹M. O’Brien, N. McEvoy, T. Hallam, H.-Y. Kim, N. C. Berner, D. Hanlon, K. Lee, J. N. Coleman, and G. S. Duesberg, “Transition Metal Dichalcogenide Growth via Close Proximity Precursor Supply”, *Scientific Reports* **4**, 7374 (2015).
- ¹⁰²F. Cadiz, C. Robert, G. Wang, W. Kong, X. Fan, M. Blei, D. Lagarde, M. Gay, M. Manca, T. Taniguchi, K. Watanabe, T. Amand, X. Marie, P. Renucci, S. Tongay, and B. Urbaszek, “Ultra-low power threshold for laser induced changes in optical properties of 2D molybdenum dichalcogenides”, *2D Materials* **3**, 045008 (2016).
- ¹⁰³P. Kirkpatrick and A. V. Baez, “Formation of Optical Images by X-Rays”, *Journal of the Optical Society of America* **39**, 766–774 (1948).
- ¹⁰⁴(Dec. 2018) http://www.spring8.or.jp/wkg/BL35XU/instrument/lang-en/INS-0000001392/instrument_summary_view.
- ¹⁰⁵(Dec. 2018) <https://www.esrf.eu/UsersAndScience/Experiments/DynExtrCond/ID28/BeamlineLayout>.
- ¹⁰⁶A. Baron, Y. Tanaka, S. Goto, K. Takeshita, T. Matsushita, and T. Ishikawa, “An X-ray scattering beamline for studying dynamics”, *Journal of Physics and Chemistry of Solids* **61**, 461–465 (2000).
- ¹⁰⁷F. Sette, G. Ruocco, M. Krisch, C. Masciovecchio, and R. Verbeni, “Collective Dynamics in Water by Inelastic X-Rays Scattering”, *Physica Scripta* **T66**, 48–56 (1996).
- ¹⁰⁸H. Tornatzky, R. Gillen, H. Uchiyama, and J. Maultzsch, “Phonon dispersion in MoS₂”, *Physical Review B* **99**, 144309 (2019).
- ¹⁰⁹A. Q. R. Baron, “Phonons in crystals using inelastic X-ray scattering”, *Journal of the Spectroscopical Society of Japan* **58**, 205 (2009).
- ¹¹⁰B. Fåk and B. Dorner, “Phonon line shapes and excitation energies”, *Physica* **234-236**, 1107–1108 (1997).
- ¹¹¹M. A. Moram and M. E. Vickers, “X-ray diffraction of III-nitrides”, *Reports on Progress in Physics* **72**, 036502 (2009).
- ¹¹²S. Mignuzzi, A. J. Pollard, N. Bonini, B. Brennan, I. S. Gilmore, M. A. Pimenta, D. Richards, and D. Roy, “Effect of disorder on Raman scattering of single-layer MoS₂”, *Physical Review B* **91**, 1–7 (2015).
- ¹¹³H. Guo, Y. Sun, P. Zhai, J. Zeng, S. Zhang, P. Hu, H. Yao, J. Duan, M. Hou, and J. Liu, “Resonant raman spectroscopy study of swift heavy ion irradiated MoS₂”, *Nuclear Instruments and Methods in Physics Research* **381**, 1–5 (2016).

- ¹¹⁴J. M. Chen and C. S. Wang, "Second order Raman spectrum of MoS₂", *Solid State Communications* **14**, 857–860 (1974).
- ¹¹⁵J. Carrete, W. Li, L. Lindsay, D. A. Broido, L. J. Gallego, and N. Mingo, "Physically founded phonon dispersions of few-layer materials and the case of borophene", *Materials Research Letters* **4**, 204–211 (2016).
- ¹¹⁶J. Maultzsch, S. Reich, C. Thomsen, H. Requardt, and P. Ordejón, "Phonon dispersion in graphite", *Physical Review Letters* **92**, 075501 (2004).
- ¹¹⁷S. Pisana, M. Lazzeri, C. Casiraghi, K. S. Novoselov, A. K. Geim, A. C. Ferrari, and F. Mauri, "Breakdown of the adiabatic Born–Oppenheimer approximation in graphene", *Nature Materials* **6**, 198–201 (2007).
- ¹¹⁸J. Yan, Y. Zhang, P. Kim, and A. Pinczuk, "Electric field effect tuning of electron-phonon coupling in graphene", *Physical Review Letters* **98**, 166802 (2007).
- ¹¹⁹M. Mohr, J. Maultzsch, E. Dobardžić, S. Reich, I. Milošević, M. Damnjanović, A. Bosak, M. Krisch, and C. Thomsen, "Phonon dispersion of graphite by inelastic X-ray scattering", *Physical Review B* **76**, 035439 (2007).
- ¹²⁰P. A. Bertrand, "Surface-phonon dispersion of MoS₂", *Physical Review B* **44**, 5745–5749 (1991).
- ¹²¹C. Sourisseau, M. Fouassier, M. Alba, A. Ghorayeb, and O. Gorochov, "Resonance Raman, inelastic neutron scattering and lattice dynamics studies of 2H-WS₂", *Materials Science and Engineering: B* **3**, 119–123 (1989).
- ¹²²T. Sekine, T. Nakashizu, K. Toyoda, K. Uchinokura, and E. Matsuura, "Raman scattering in layered compound 2H-WS₂", *Solid State Communications* **35**, 371–373 (1980).
- ¹²³G. Lucovsky, R. M. White, J. A. Benda, and J. F. Revelli, "Infrared-Reflectance Spectra of Layered Group-IV and Group-VI Transition-Metal Dichalcogenides", *Physical Review B* **7**, 3859 (1973).
- ¹²⁴S. Uchida and S. Tanaka, "Optical phonon modes and localized effective charges of transition-metal dichalcogenides", *Journal of the Physical Society of Japan* **45**, 153–161 (1978).
- ¹²⁵C. Sourisseau, F. Cruege, M. Fouassier, and M. Alba, "Second-order Raman effects, inelastic neutron scattering and lattice dynamics in 2H-WS₂", *Chemical Physics* **150**, 281–293 (1991).
- ¹²⁶H. Tornatzky, A.-M. Kaulitz, and J. Maultzsch, "Resonance Profiles of Valley Polarization in Single-Layer MoS₂ and MoSe₂", *Physical Review Letters* **121**, 167401 (2018).

- ¹²⁷C. R. Zhu, K. Zhang, M. Glazov, B. Urbaszek, T. Amand, Z. W. Ji, B. L. Liu, and X. Marie, "Exciton valley dynamics probed by Kerr rotation in WSe₂ monolayers", *Physical Review B* **90**, 161302(R) (2014).
- ¹²⁸T. Korn, S. Heydrich, M. Hirmer, J. Schmutzler, and C. Schüller, "Low-temperature photocarrier dynamics in monolayer MoS₂", *Applied Physics Letters* **99**, 102109 (2011).
- ¹²⁹P. Tonndorf, R. Schmidt, P. Böttger, X. Zhang, J. Börner, A. Liebig, M. Albrecht, C. Kloc, O. Gordan, D. R. T. Zahn, S. Michaelis de Vasconcellos, and R. Bratschitsch, "Photoluminescence emission and Raman response of monolayer MoS₂, MoSe₂, and WSe₂", *Optics Express* **21**, 4908 (2013).
- ¹³⁰G. Plechinger, F.-X. Schrettenbrunner, J. Eroms, D. Weiss, C. Schüller, and T. Korn, "Low-temperature photoluminescence of oxide-covered single-layer MoS₂", *physica status solidi (RRL) - Rapid Research Letters* **6**, 126–128 (2012).
- ¹³¹S. Tongay, J. Suh, C. Ataca, W. Fan, A. Luce, J. S. Kang, J. Liu, C. Ko, R. Raghunathanan, J. Zhou, F. Ogletree, J. Li, J. C. Grossman, and J. Wu, "Defects activated photoluminescence in two-dimensional semiconductors: interplay between bound, charged, and free excitons.", *Scientific reports* **3**, 2657 (2013).
- ¹³²G. E. Pikus and A. N. Titkov, *Optical orientation*, edited by F. Meier and B. Zakharchenya, Vol. 8, Modern problems in condensed matter sciences (North Holland (Amsterdam), 1984).
- ¹³³H. M. Hill, A. F. Rigosi, C. Roquelet, A. Chernikov, T. C. Berkelbach, D. R. Reichman, M. S. Hybertsen, L. E. Brus, and T. F. Heinz, "Observation of Excitonic Rydberg States in Monolayer MoS₂ and WS₂ by Photoluminescence Excitation Spectroscopy", *Nano Letters* **15**, 2992–2997 (2015).
- ¹³⁴*Private communication with Dr. Alexey Chernikov (Universität Regensburg).*
- ¹³⁵*Private communication with Dr. Paulina Plochocka (Laboratoire National des Champs Magnétique Intenses – Toulouse).*
- ¹³⁶L. C. Andreani, F. Tassone, and F. Bassani, "Radiative lifetime of free excitons in quantum wells", *Solid State Communications* **77**, 641–645 (1991).
- ¹³⁷H. Shi, R. Yan, S. Bertolazzi, J. Brivio, B. Gao, A. Kis, D. Jena, H. G. Xing, and L. Huang, "Exciton Dynamics in Suspended Monolayer and Few-Layer MoS₂ 2D Crystals", *ACS Nano* **7**, 1072–1080 (2013).
- ¹³⁸D. Sun, Y. Rao, G. A. Reider, G. Chen, Y. You, L. Brézin, A. R. Harutyunyan, and T. F. Heinz, "Observation of Rapid Exciton–Exciton Annihilation in Monolayer Molybdenum Disulfide", *Nano Letters* **14**, 5625–5629 (2014).
- ¹³⁹S. Mouri, Y. Miyauchi, M. Toh, W. Zhao, G. Eda, and K. Matsuda, "Nonlinear photoluminescence in atomically thin layered WS₂ arising from diffusion-assisted exciton–exciton annihilation", *Physical Review B* **90**, 155449 (2014).

- ¹⁴⁰T. Yu and M. W. Wu, “Valley depolarization due to intervalley and intravalley electron-hole exchange interactions in monolayer MoS₂”, *Physical Review B* **89**, 205303 (2014).
- ¹⁴¹C. Robert, D. Lagarde, F. Cadiz, G. Wang, B. Lassagne, T. Amand, A. Balocchi, P. Renucci, S. Tongay, B. Urbaszek, and X. Marie, “Exciton radiative lifetime in transition metal dichalcogenide monolayers”, *Physical Review B* **93**, 205423 (2016).
- ¹⁴²G. Kioseoglou, A. T. Hanbicki, M. Currie, A. L. Friedman, D. Gunlycke, and B. T. Jonker, “Valley polarization and intervalley scattering in monolayer MoS₂”, *Applied Physics Letters* **101**, 221907 (2012).
- ¹⁴³G. Kioseoglou, A. T. Hanbicki, M. Currie, A. L. Friedman, and B. T. Jonker, “Optical polarization and intervalley scattering in single layers of MoS₂ and MoSe₂”, *Scientific Reports* **6**, 25041 (2016).
- ¹⁴⁴G. Kioseoglou, M. Korkusinski, T. Scrace, A. T. Hanbicki, M. Currie, B. T. Jonker, A. Petrou, and P. Hawrylak, “Spin effects in MoS₂ and WS₂ single layers”, *Physica Status Solidi – Rapid Research Letters* **10**, 111–119 (2016).
- ¹⁴⁵C. Mai, A. Barrette, Y. Yu, Y. G. Semenov, K. W. Kim, L. Cao, and K. Gundogdu, “Many-body effects in valleytronics: Direct measurement of valley lifetimes in single-layer MoS₂”, *Nano Letters* **14**, 202–206 (2014).
- ¹⁴⁶M. Baranowski, A. Surrente, D. K. Maude, M. Ballottin, A. A. Mitioglu, P. C. M. Christianen, Y. C. Kung, D. Dumcenco, A. Kis, and P. Plochocka, “Dark excitons and the elusive valley polarization in transition metal dichalcogenides”, *2D Materials* **4**, 025016 (2017).
- ¹⁴⁷M. Z. Maialle, E. A. de Andrada e Silva, and L. J. Sham, “Exciton spin dynamics in quantum wells”, *Physical Review B* **47**, 15776–15788 (1993).
- ¹⁴⁸S. Dal Conte, F. Bottegoni, E. A. A. Pogna, D. De Fazio, S. Ambrogio, I. Bargigia, C. D’Andrea, A. Lombardo, M. Bruna, F. Ciccacci, A. C. Ferrari, G. Cerullo, and M. Finazzi, “Ultrafast valley relaxation dynamics in monolayer MoS₂ probed by nonequilibrium optical techniques”, *Physical Review B* **92**, 1–6 (2015).
- ¹⁴⁹M. Selig, G. Berghäuser, M. Richter, R. Bratschitsch, A. Knorr, and E. Malic, “Dark and bright exciton formation, thermalization, and photoluminescence in monolayer transition metal dichalcogenides”, *2D Materials* **5**, 035017 (2018).
- ¹⁵⁰R. Schmidt, G. Berghäuser, R. Schneider, M. Selig, P. Tonndorf, E. Malić, A. Knorr, S. Michaelis de Vasconcellos, and R. Bratschitsch, “Ultrafast Coulomb-Induced Intervalley Coupling in Atomically Thin WS₂”, *Nano Letters* **16**, 2945–2950 (2016).
- ¹⁵¹(Apr. 2019) <https://www.astm.org/Standards/D150.htm>.

-
- ¹⁵²G.-H. Lee, X. Cui, Y. D. Kim, G. Arefe, X. Zhang, C.-H. Lee, F. Ye, K. Watanabe, T. Taniguchi, P. Kim, and J. Hone, "Highly Stable, Dual-Gated MoS₂ Transistors Encapsulated by Hexagonal Boron Nitride with Gate-Controllable Contact, Resistance, and Threshold Voltage", *ACS Nano* **9**, 7019–7026 (2015).
- ¹⁵³A. Castellanos-Gomez, M. Buscema, R. Molenaar, V. Singh, L. Janssen, H. S. J. van der Zant, and G. A. Steele, "Deterministic transfer of two-dimensional materials by all-dry viscoelastic stamping", *2D Materials* **1**, 011002 (2014).
- ¹⁵⁴*Private communications with Dr. Aurélie Pierret (Laboratoire de Physique de l'Ecole Normale Supérieure, ENS, Université PSL, Paris).*
- ¹⁵⁵E. Courtade, B. Han, S. Nakhaie, C. Robert, X. Marie, P. Renucci, T. Taniguchi, K. Watanabe, L. Geelhaar, J. M. J. Lopes, and B. Urbaszek, "Spectrally narrow exciton luminescence from monolayer MoS₂ and MoSe₂ exfoliated onto epitaxially grown hexagonal BN", *Applied Physics Letters* **113**, 032106 (2018).

Acknowledgement

This work would not have been possible without the support from many people. I would like to take this chance to thank especially

Prof. Dr. Janina Maultzsch, who introduced me to the fascinating flat part of the physics world and advised and encouraged my working towards this thesis,

Prof. Dr. Axel Hoffmann for reviewing my thesis and for the continuous reminders of what already has been done (not only in physics), which helped to sharpen the perception of whats in the present,

Prof. Dr. Michael Lehmann for being the chairman of my defense,

The team of the Feinmechanische Werkstatt: Daniela Beiße, Marco Haupt, Andreas Ludewig and Wolfgang Piper. Without your help many projects would have been bound to fail – or at least wouldn't look that good now ;),

Dr. Harald Scheel and Anja Sandersfeld, for their help regarding all the 'little', yet (very) important things.

Dr. Roland Gillen for the computational support of my work,

Sebastian Weigand for the long-suffering process of teaching me (some) python and the part-taking in the journey of trying to increase the knowledge with which students leave us after the semester,

Henrik Wähnert, for the consistent support of my escapades in teaching and preventing me from flying through the lecture hall,

Johannes Enslin, for the help with HRXRD measurements,

and all of the Members of the AG Thomsen / Hoffmann / Maultzsch (both Berlin and Erlangen!) for the better moments during the past years.

Finally, I want to thank my family for the inexhaustible encouragement.

This wouldn't have happened without you.
Thank you!